

Nitrogen-Rich Carbonaceous Materials for Advanced Oxygen Electrocatalysis: Synthesis, Characterization, and Activity of Nitrogen Sites

Bin Wu, Haibing Meng, Dulce M. Morales, Feng Zeng, Junjiang Zhu, Bao Wang, Marcel Risch, Zhichuan J. Xu, and Tristan Petit*

Nitrogen-doped carbons are among the fastest-growing class of materials used for oxygen electrocatalysis, namely, the oxygen reduction reaction (ORR) and oxygen evolution reaction (OER), thanks to their low cost, environmental friendliness, excellent electrical conductivity, and scalable synthesis. The perspective of replacing precious metal-based electrocatalysts with nitrogen-doped carbon is highly desirable for reducing costs in energy conversion and storage systems. In this review, the role of nitrogen and N-induced structural defects on the enhanced performance of N-doped carbon electrocatalysts toward the OER and the ORR as well as their applications for energy conversion and storage technologies is summarized. The synthesis of N-doped carbon electrocatalysts and the characterization of their nitrogen functional groups and active sites for the conversion of oxygen are also reviewed. The electrocatalytic performance of the main types of N-doped carbon materials for OER/ORR electrocatalysis are then discussed. Finally, major challenges and future opportunities of N-doped carbons as advanced oxygen electrocatalysts are highlighted.

and air pollution are consequences of the current economic expansion driven by fossil fuels.^[1–5] Considering that the energy demand is continuously increasing, the development of low cost and efficient energy technologies based on green and clean sustainable energy sources is urgently needed. Electrochemical energy conversion and storage technologies, such as water electrolyzers, fuel cells, and metal–air batteries, are hence expected to be further developed and widely commercialized in the coming decades.^[6,7] However, the advances of this kind of systems are often significantly hindered by the sluggish kinetics of oxygen electrocatalysis, namely the oxygen evolution reaction (OER) and the oxygen reduction reaction (ORR), which are fundamental for energy conversion and storage processes and nearly determine the cost and efficiency for these technologies.^[4,8–12] In the ORR, the O₂ molecule combines with electrons to

1. Introduction

The environment is currently under serious threat and irretrievable damage due to climate change, imbalanced energy shortage,

form a chemical product, whereas OER generates an O₂ molecule by taking electrons from a reactant.

Precious metals supported on carbon materials, such as Pt/C, have been traditionally considered the state-of-the-art

B. Wu, T. Petit
Young Investigator Group Nanoscale Solid-Liquid Interfaces
Helmholtz-Zentrum Berlin für Materialien und Energie GmbH
Albert-Einstein-Straße 15, 12489 Berlin, Germany
E-mail: tristan.petit@helmholtz-berlin.de

B. Wu
Institute of Physics
Humboldt University Berlin
Newton-Straße 15, 12489 Berlin, Germany

H. Meng
College of Chemistry
Taiyuan University of Technology
Taiyuan 030024, China

 The ORCID identification number(s) for the author(s) of this article can be found under <https://doi.org/10.1002/adfm.202204137>.

© 2022 The Authors. Advanced Functional Materials published by Wiley-VCH GmbH. This is an open access article under the terms of the Creative Commons Attribution License, which permits use, distribution and reproduction in any medium, provided the original work is properly cited.

DOI: 10.1002/adfm.202204137

D. M. Morales, M. Risch
Nachwuchsgruppe Gestaltung des Sauerstoffentwicklungsmechanismus
Helmholtz-Zentrum Berlin für Materialien und Energie GmbH
Hahn-Meitner-Platz 1, 14109 Berlin, Germany

F. Zeng
State Key Laboratory of Materials-Oriented Chemical Engineering
College of Chemical Engineering
Nanjing Tech University
Nanjing 211816, China

J. Zhu
Hubei Key Laboratory of Biomass Fibers and Eco-dyeing and Finishing
College of Chemistry and Chemical Engineering
Wuhan Textile University
Wuhan 430200, China

B. Wang
State Key Laboratory of Biochemical Engineering
Institute of Process Engineering
Chinese Academy of Sciences
Beijing 100190, China

Z. J. Xu
School of Materials Science and Engineering
Nanyang Technological University
50 Nanyang Avenue, Singapore 639798, Singapore

electrocatalysts for ORR, while noble metal oxides, for example, RuO₂ and IrO₂, have been widely explored as electrocatalysts for the OER.^[13–15] However, precious metal-based catalysts have several noticeable disadvantages, such as high cost, poor durability, and limited natural abundance, all of which severely limits large-scale applications.^[16,17] To address this, a remarkable effort has been devoted to substitute Pt group-based electrodes in order to achieve cost-efficient, highly active and stable ORR and OER electrocatalysts.^[17,18] Carbon-based materials appear particularly relevant as oxygen electrocatalysts owing to their low cost, high abundance, often excellent electrical conductivity, and strong resistance to alkaline electrolytes, which could prominently increase the ORR and OER efficiency.^[8,17–19] Nevertheless, the adsorption/activation of reaction intermediates is not readily available on the inert surface of pristine carbon. Thereby, effective strategies, including chemical doping and the introduction of structural defects, have been considered to tune the electrocatalytic ORR/OER activity of carbon nanomaterials.^[18,20]

Nitrogen-doping, especially, has emerged as one of the most promising approaches to achieve high-performance bifunctional oxygen electrocatalysts, that is, materials that are able to catalyze both the OER and the ORR.^[21–24] Importantly, in 2009, the discovery of a catalyst consisting of N-doped carbon nanotube arrays showing superb electrocatalytic ORR activity compared to conventional catalysts triggered enormous interest in the field.^[25] Subsequently, N-doped carbon nanomaterials have been further proved as excellent catalysts exhibiting a long lifetime, enhanced tolerance, and versatility in functionality, being able to catalyze various reactions including the OER, oxidative dehydrogenation, CO₂ reduction, among others.^[23,26] The wide diversity of possible nitrogen sites offers a large panel of N-doped carbon electrocatalysts.^[22,27] The improved electrocatalytic performance of N-doped carbons compared to other carbon-based catalysts is generally assigned to the electron-accepting ability of the nitrogen atoms. Moreover, having a similar atomic radius as carbon atom, a perfect lattice match is ensured. Different classes of N-containing structures are formed, including pyridinic, pyrrolic, and graphitic nitrogen, which establishes net positive charge density on adjacent carbon atoms in the nanocarbon structure, thus changing the oxygen adsorption/generation and facilitating the conversion of oxygen.^[8,21,22,27,28]

Heteroatom(s)-doped carbon-based electrocatalysts for the ORR have been recently reviewed.^[21,23,27] However, the knowledge of the critical active sites and underlying reaction pathways of N-doped carbonaceous catalysts in OER requires deeper discussion. Furthermore, a comprehensive overview on the role of nitrogen in N-doped carbon for oxygen electrocatalysis, in particular including recent developments on the relationship between N-induced defects and reaction activity, is still missing. In addition, characterization of catalysts, either *ex situ* or *in situ/operando*, is essential to confirm reaction mechanisms and requires a special attention. Based on a proper understanding of N-related reactivity toward oxygen electrocatalysis, the design of high-performance N-doped carbonaceous OER and ORR catalysts will be facilitated.

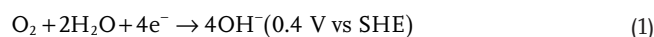
In this review, we comprehensively summarize the recent progress in N-doped carbon-based oxygen electrocatalysts

focusing on the main categories of N-doped carbon introduced over the last decade, including but not limited to N-doped graphene,^[29–32,34–36] carbon nanotubes,^[25] carbon nitride,^[37,38] graphdiyne,^[33] and carbon quantum dots,^[39–41] as illustrated in **Figure 1**. While we mostly focus on metal-free catalysts, some examples of codoping by transition metals will be mentioned. An introduction on the fundamentals of oxygen electrocatalysis applied to N-doped carbon-based electrocatalysts is firstly given. Then, representative studies highlighting the role of OER and ORR in various applications, including metal–air batteries, fuel cells, and seawater batteries are reviewed. Afterward, the main synthesis routes and spectroscopic signatures of N-doped carbon-based oxygen electrocatalysts are summarized before presenting the most recent research progress related to the OER/ORR electrochemical activity on N-doped carbon-based electrocatalysts by type of materials. Finally, the challenges and outlook for N-doped carbon toward oxygen electrocatalytic applications are proposed at the end of this contribution.

2. Fundamentals of Oxygen Electrocatalysis on N-Doped Carbon Materials

2.1. ORR: Reaction Pathway and Mechanisms

The reaction process of the reduction of oxygen in an aqueous electrolyte, taking place at the cathode of fuel cells or at the air electrode in metal–air batteries, generally includes the following steps: 1) diffusion and adsorption of O₂ at the surface of electrocatalysts, 2) electron migration from the anode to adsorbed O₂ molecules, 3) weakening and splitting of O=O bonds, and 4) removal of the generated species to the electrolyte.^[42–46] There are two typical adsorption ways: bidentate O₂ adsorption (two oxygen atoms coordinating with two catalytic centers) and end-on O₂ adsorption (one oxygen atom coordinating vertically to one catalytic center), both of which may result in either the four-electron transfer pathway, also known as a direct pathway, or the two-electron transfer pathway, also called an indirect pathway, or the two of them concomitantly.^[47] The four-electron transfer pathway requires the rupture of an O–O bond with a bond energy of 118 kcal mol^{−1}, which is usually achieved with platinum group-based materials as catalysts.^[48] For a direct four-electron transfer pathway, the reactions in alkaline (Equation (1)) and acidic (Equation (2)) electrolytes are as follows^[49]



where SHE represents the standard hydrogen electrode.

In the case of the indirect pathway, peroxide species are formed upon the transfer of 2 electrons, which can be followed by another 2-electron transfer step to produce H₂O or OH[−] in acidic and alkaline media, respectively, or by chemical disproportionation of the peroxide species.^[50] This pathway primarily dominates carbon-based catalysts.^[45,51,52]

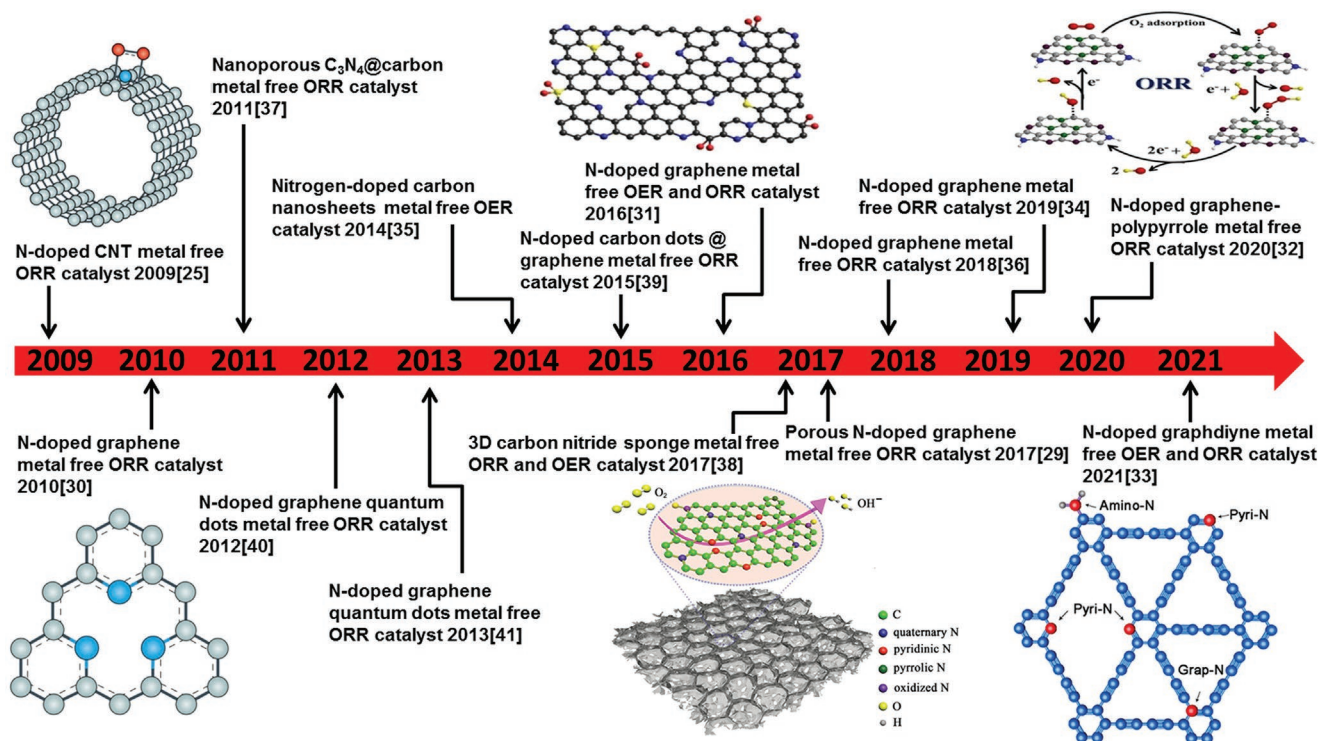
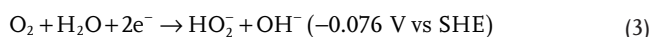


Figure 1. Timeline showing important developments of N-doped carbon-based metal-free catalysts. The schemes include N-doped graphene, carbon nanotubes and graphdiyne. Reproduced with permission.^[29] Copyright 2016, Springer Nature. Reproduced with permission.^[30] Copyright 2010, American Chemical Society; Reproduced with permission.^[31] Copyright 2016, American Association for the Advancement of Science; Reproduced with permission.^[32] Copyright 2020, Wiley-VCH GmbH; Reproduced with permission.^[25] Copyright 2009, American Association for the Advancement of Science; Reproduced with permission.^[33] Copyright 2021, Elsevier.

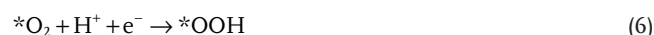
The reactions in alkaline (Equation (3)) and acidic (Equation (4)) media for an indirect two-electron transfer pathway are^[49]



In fact, the ORR is a multistep electron-transfer process involving various oxygen-containing species such as OOH^* , OH^* , O^* , where $*$ represents an active catalytic site.^[53–56] The reaction may take place via the associative mechanism.^[57] In acidic media, after O_2 is adsorbed onto the active sites at the surface of the catalyst, an electron is seized to form an activated $*\text{O}_2$ molecule (Equation (5)) and afterward connected with an H^+ ion to produce $*\text{OOH}$ as shown in Equation (6).^[3,9] Subsequently, reduction of $*\text{OOH}$ upon the combination with another H^+ and an electron leads to the production of either H_2O_2 (indirect pathway), or H_2O and $*\text{O}$ (direct pathway) as shown in Equations (7a) and (7b), respectively. In the latter case, the formed $*\text{O}$ reacts with H^+ in the electrolyte, resulting in the formation of $*\text{OH}$ which finally converts into H_2O according to Equations (8) and (9).^[3] Alternatively, in a so-called dissociative mechanism, the O_2 molecule is adsorbed onto the surface of the catalysts, after which the $\text{O}-\text{O}$ bond of O_2 is split into two O^* species (Equation (10)). Then, H^+ is adsorbed on the surface of the catalysts to form OH^* (Equation (8)), and eventually

produces H_2O by the combination of OH^* and H^+ as shown in Equation (9), similarly to the associative mode.^[43] The related equations are shown in the following.^[58–61]

Associative mode:



Dissociative mode:



In the case of alkaline media, the corresponding reaction steps take place analogously to those shown in Equations (5)–(10) for acidic electrolytes, with H_2O replacing

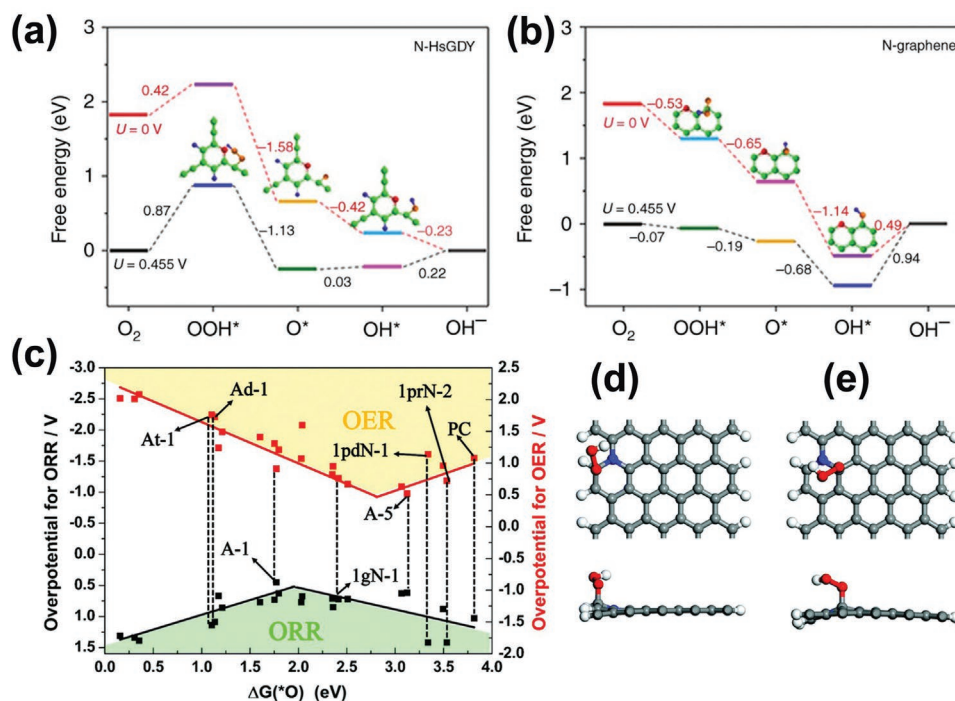


Figure 2. Free energy diagrams of the oxygen reduction reaction (ORR) on a) pyridinic nitrogen-doped hydrogen-substituted graphdiyne (N-HsGDY) and b) pyridinic N-doped graphene edge (N-graphene), at 0.455 and 0V (vs reference hydrogen electrode, RHE) in alkaline media. Reproduced with permission.^[62] Copyright 2018, Springer Nature. c) Volcano plot for the ORR and OER showing the overpotential as a function of $\Delta G(^*\text{O})$ at various possible active sites. Top and side views of the active site d) A-1 for the ORR, e) A-3 for the OER, with OOH adsorbed. Reproduced with permission.^[64] Copyright 2019, The Royal Society of Chemistry.

H^+ and participating in the reaction to generate OH^- ions (instead of H_2O molecules) as products.

Considering the possible ORR mechanisms mentioned above, the identification of reaction intermediates such as $^*\text{OOH}$, $^*\text{OH}$, and $^*\text{O}$ in N-doped carbon-based electrocatalysts has been the topic of intense research efforts. For example, Lv et al. used density functional theory (DFT) to calculate the ORR free energy diagrams for pyridinic N-doped hydrogen-substituted graphdiyne (N-HsGDY) and pyridinic N-doped graphene at 0 and 0.455 V versus RHE in an alkaline electrolyte (Figure 2a,b).^[62] For pyridinic N-HsGDY, $^*\text{OOH}$, $^*\text{OH}$, and $^*\text{O}$ adsorb on the acetylenic C atom adjacent to the benzene ring. The C atoms adjacent to N alkynyl groups in N-HsGDY possess a higher positive charge density (0.694) compared to that in N-graphene (0.392) due to the inserted alkynyl groups between benzene rings in N-HsGDY. Because of steric hindrance, the adjacent carbons of N are not active sites, but they can affect the active carbon atom. The different charge distributions result in different rate-determining steps over N-HsGDY and N-graphene. ORR over N-HsGDY is rate-limited by $^*\text{OOH}$ adsorption, while the rate-determining step over N-graphene is the desorption of $^*\text{OH}$. Furthermore, the authors found that the free energy change of the rate-determining step for N-HsGDY is smaller than that over N-graphene, indicating smaller resistance to the ORR driven by N-HsGDY. Moreover, in order to investigate the effect of the composition of N-sites on the ORR activity and selectivity, Behan et al. computed the Gibbs energies of the relevant ORR intermediates using DFT.^[63] The active sites with the highest theoretical potential

for graphene are graphitic N and pyridinic N sites. Graphene, comprising only graphitic N or pyridinic N, exhibited a reduction of HO^* to OH^- (O_2 to HOO^*) as the potential limiting steps, respectively. In addition, DFT calculations predicted the weakest binding for the HO_2^- intermediate for the homogeneous graphene with all graphitic N clusters, suggesting HO_2^- desorption competed effectively with its subsequent reduction to HO^- on these graphitic N-rich surfaces. On the other hand, the homogeneous graphene with all pyridinic N clusters displayed the weakest adsorption energy for HOO^* . Therefore, on pyridinic N-rich surfaces, desorption of HOO^* competed more effectively with subsequent reductions. The type of nitrogen sites, therefore, plays a major role on the oxygen reduction pathway and will be discussed in more detail in the next section.

All in all, the ORR mechanisms on N-doped carbon materials are still not well understood due to the difficulty to accurately identify the active sites and the complicated transfer processes between active sites and intermediates in the reaction pathways.^[43] The proposed pathways mentioned above might be further complemented in the future.

2.2. OER: Reaction Pathway and Mechanisms

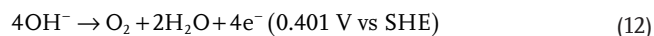
The OER is the reverse reaction of the ORR, namely, H_2O (acidic media) or OH^- (alkaline media) loses electrons to produce O_2 .^[65–68] In fact, water molecules are decomposed via electrolysis into hydrogen and oxygen by applying an external

potential, thus the OER is also regarded as the half-reaction of the water splitting reaction.^[43,65,69–71] Similar to the ORR, the possible reaction pathways of the OER depend on the pH of the solution with slight differences upon different reactive species under acidic media (H₂O) and alkaline media (OH⁻) involved in the reaction process.^[66,72] Briefly, the OER process is summarized in Equations (11) and (12).

In acid aqueous electrolyte:



In alkaline aqueous systems:



where SHE represents the standard hydrogen electrode.

In addition, the OER may also take place in aprotic electrolytes, and the resulting process is shown in Equation (13)



Similar to the ORR, the OER occurs via different mechanisms in both acidic and alkaline media by combining two *O to produce O₂, or forming *OOH first.^[73] These related processes are exhibited as follows from Equations (14)–(22).^[74]

In acidic electrolytes, the oxygen intermediates are formed as follows



Afterward, the two possible pathways proposed by Bockris and Kobussen are^[75,76]



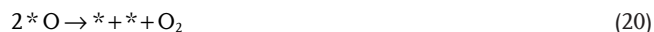
or



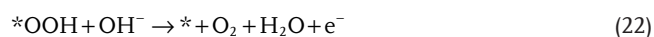
Similarly for alkaline electrolytes, *O is generated first



Subsequently, the pathways are



or



It is important to note that carbon-based catalysts subjected to the anodic conditions of the OER may undergo oxidation along with the generation of oxygen species on the surface, particularly in acidic media. This may lead to a decrease in their electrical conductivity and, in some cases, to the decomposition of the electrode.^[43,77] Thus, achieving long-term stability of carbon-based materials in a highly oxidative OER environment may be challenging.

The favorable OER mechanisms on N-doped carbon-based electrocatalysts were recently addressed by DFT calculations. Typically, the potential-determining steps for OER can either be the formation of *O from *OH (Equation (15)) or the transformation of *O to *OOH (Equations (17)–(21)) in OER as determined through DFT.^[78,79] Partanen et al. studied the kinetic barriers of the OER on singly and doubly N-doped single-walled carbon nanotubes, denoted as NCNTs and N2CNTs, respectively.^[80] A four-step OER process was considered and the formation of *OOH was found to be the rate-determining step on both structures, while the kinetic barrier over NCNTs is 0.4 eV lower than that over N2CNTs. In addition, Jiang et al. identified ORR/OER active sites over N-doped carbon nanosheets.^[64] Figure 2c presents the ORR/OER overpotential as a function of Gibbs free energy of oxygen adsorption, ΔG(*O), for various active sites on the N-doped graphene monolayer, as well as the armchair and zigzag graphene nanoribbons. The increasing ΔG(*O) indicates that the interaction between the oxygen atom and the active site gets weaker. Thus, the pristine (undoped) carbon (PC) with the largest ΔG(*O) interacts most weakly with oxygen. Accordingly, it is inefficient for the ORR and for the OER. Yet, incorporating N as a dopant enhances the interaction, resulting in a decreasing overpotential trend for the conversion of oxygen. Furthermore, A-1 C atom (Figure 2d) and A-3 C atom (Figure 2e) are found the most active sites for the ORR and for the OER, respectively. The authors also compared the activity over graphitic, pyridinic and pyrrolic N-doped monolayer graphene, and found that the graphitic N-doped carbon possesses the lowest overpotential. The N dopant modifies the electronic properties of carbon nanosheets, influencing thereby the adsorption of oxygen atoms and, thus, the activity toward the ORR and the OER.

Several hypotheses on the role of N-dopant in these reaction pathways have been proposed so far. On the one hand, the location of N dopants in the carbon matrix is considered to have an impact on the absorption of reaction intermediates. For example, Li et al. found that carbon atoms near nitrogen atoms acts as active sites with moderate adsorption energy, reducing the OER overpotential.^[81] Fan et al. confirmed that the introduced nitrogen atoms can regulate the electronic structure of adjacent carbon atoms to optimize the adsorption energies for intermediates.^[82] The conversion of *O to *OOH intermediates, which is the potential-determining step, showed the lowest Gibbs energy of 1.69 eV on carbon atoms next to the pyridinic N. Zhao et al. also showed both theoretically and experimentally that carbon atoms next to nitrogen atoms are positively charged at the first step due to the electron-withdrawing nitrogen atoms, which facilitates absorption of OH⁻.^[83] The high positive charge density of neighboring carbon atoms also promotes the electron transfer between the catalyst surface and reaction intermediates (for example, *OH and *O).^[84] This was further confirmed by

Yang et al. who observed that adsorption of *OOH and *O intermediates occurs likely on carbon atoms next to the pyridinic N rather than graphitic and pyrrolic N by comparing X-ray absorption spectra before and after OER.^[31] On the other hand, Zhao et al. propose that the dominant active sites, which have an affinity to OH^- for OER on N-doped carbon, are the carbon atoms adjacent to the graphitic N based on DFT calculation.^[85] Similarly, Jiang et al. also confirmed that the carbon atom that is near the graphitic N dopant is the most efficient active site enabling strong OH^- adsorption for defect-rich and ultrathin N-doped carbon nanosheets as OER catalysts.^[64] These few theoretical examples demonstrate that the nature of the nitrogen sites is predicted to have a dramatic impact on the electrocatalytic pathway even though details are still actively discussed. The current understanding of the different roles that can play nitrogen dopants on these reaction mechanisms from experimental results is summarized in the following.

2.3. Nitrogen Atoms as Electrocatalytic Active Sites

Generally, it is believed that doping-induced electron modulation dominates the high activity of carbon-based catalysts.^[86] N-doping of sp^2 carbons for increasing their performance toward the ORR and the OER is usually motivated

by 1) N and C have similar atomic radius, thus avoiding lattice mismatch, 2) N has one more electron than C, which facilitates electron-demanding reactions such as the ORR, and 3) N has an outer lone pair after binding with C atoms, which translates into a larger amount of defects that increase the density of active sites.^[23] Additionally, N-doped materials are easier to synthesize compared to other heteroatom-doped counterparts.^[45]

Nitrogen commonly exists in the form of pyridine-like, pyrrole-like, and graphitic nitrogen as shown in Figure 3.^[87] There is an ongoing debate regarding the contributions of the different types of nitrogen to the ORR, and its understanding is at the beginning stage. With in-depth studies on different N configurations in doping states, several research groups have explored the contribution of pyridinic N toward the high performance of N-doped carbon-based catalysts in ORR, whereas some groups declared graphitic N is responsible for the enhanced ORR activity.^[88–90]

To comprehensively understand the role of the pyridinic N and graphitic N, scanning tunneling microscopy (STM) was conducted.^[91] The work aimed to identify the effect of doping by these two types of N on the electronic structure around the Fermi level as well as changes of charge density due to N-doping (Figure 3a,b).^[91] Scanning tunneling spectra (STS) shown in Figure 3a,b were measured at the positions indicated by arrows (one was surrounded by a bright region (type A), and the other

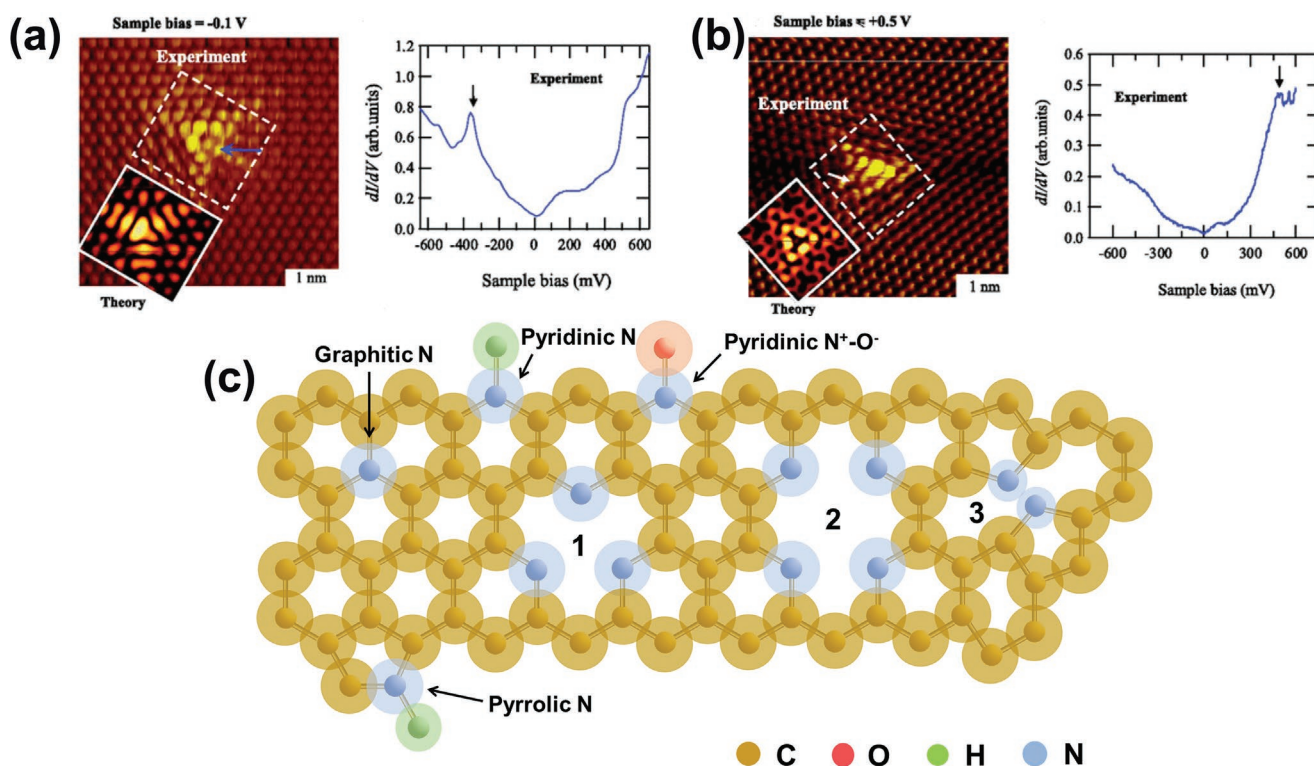


Figure 3. a) STM topographic image of pyridinic N defect. The simulated STM image ($V = -0.1$ V) is also shown for comparison. STS spectrum was measured at the position indicated by the arrow on left side in (a). b) STM topographic image corresponding to graphitic N defects. The simulated STM image ($V = +0.5$ V) is also shown for comparison. STS spectrum was measured at the position indicated by the arrow on left side in (b). Reproduced with permission.^[91] Copyright 2012, American Physical Society. c) Schematic illustration of common N species and defects in carbon materials. 1) Pyridinic N with monovacancy (Pyr-N3), 2) porphyrinic N divacancy (Por-N4), and 3) pyrrolic N (NPY) with Stone-Thrower-Wales defect.

was surrounded by a dark region (type B)). For pyridinic N, it consists of a large peak at around -370 mV and smaller peaks within a parabolic background along with a type-A defect, while a peak at $+500$ mV along with a type-B defect for graphitic N in the STS spectrum. The results indicated that the sites around the pyridinic N might act as a Lewis base, which is beneficial for the ORR, while graphitic N surrounding C atoms may play a role as Lewis acid. Pyridinic N with a lone electron pair is more electrochemically active by improving the electron-donating capability and weakening the O—O bond in ORR.^[92] According to past studies, pyridinic N contributes with four electrons to the sp^2 configuration with a lone pair, while the other valence electron exists in the π -conjugated system.^[22,27,93] Owing to the higher electronegativity of a nitrogen atom compared to that of a carbon atom, the pyridinic N is negatively charged, as proved by the aforementioned experiment related to the Lewis base.^[22,27,94]

On the other hand, by measuring the electrocatalytic performances of a series of electrocatalysts with different types of N species, Yang et al. showed that the electron-donating graphitic N served as ORR active centers, whereas the electron-withdrawing functional groups acted as OER active centers.^[31] Graphitic N was found to provide a favorable ORR catalytic activity under neutral and alkaline conditions through a 2-electron transfer pathway.^[31] These N species donate three electrons for the sp^2 configuration along with two electrons in the p^z orbital, which can move to the stable π -conjugated system of graphite, leading to the positive charge of the graphitic N.^[22,27,95,96] In addition to this, the sp^2 hybrid carbon skeleton possesses a π bond negative charge resulting from the additional lone pair electrons of the N atom, therefore enhancing the electron transport abilities and chemical reactivity of the material.^[22,27,97]

Pyrrolic N is also considered as one of the possible active sites due to its similar structure to pyrrolidine but fewer works are available on its role in ORR and OER.^[21] Actually, pyrrolic N is not commonly found in carbon matrices due to a low stability induced by the unique structure of five-membered heterocyclic rings.^[21,98] For example, Lin et al. showed that the carbonization at 1000 °C of polypyrrole leads to the complete disappearance of pyrrole groups.^[99] Yet, some studies showed that pyrrolic N in N-doped carbons are catalytically active. Li et al. revealed the displacement of pyrrole N position as the adsorption site of the *OOH intermediate by means of XAS.^[100] Additionally, the ORR activity was found in direct proportion to the content of pyrrolic N. These results suggest that pyrrolic N can effectively preserve the *OOH intermediate and suppress its further dissociation into O^* and *OH intermediate states. Furthermore, Li et al. reported that the highest ORR catalytic activity of ordered mesoporous carbon doped with different N species was obtained for the sample which exhibited the highest pyrrolic and pyridinic contents.^[101] Likewise, the synthesis of pyridinic and pyrrolic N-doped carbon using the template method exhibited superior catalytic activity compared to commercial platinum-based catalysts as shown by Feng et al.^[102] Finally, based on DFT calculations, Zhang and Xia confirmed that pyrrole-based N-doped carbon materials trigger a 4-electron transfer pathway through a bridging binding mode in form of the nitrogen functionality and subsequently lead to the cleavage of the O—O bond due to the formation of two C—O—H

intermediates in the late reduction stages, resulting in the final formation of two water molecules during ORR.^[103] While the activity of pyrrolic-like groups is rarely considered due to their unstable chemical configuration, the few observations on the enhancement of catalytic performance resulting from presence of pyrrolic N may require more attention in the future.^[104,105]

Moreover, Liu et al. prepared a series of N-doped carbons by pyrolysis of a ground mixture of carbon black and urea, and reported the order of catalytic activities corresponding to different N species: pyridinic N > pyrrolic N > graphitic N > oxidized N > carbon skeleton.^[106] Yet, it is important to consider that, since the different types of nitrogen are simultaneously present in N-doped carbons, deconvoluting their individual contribution is very challenging. It has been further suggested that a combination of N species can lead to strong synergies and thus boost their catalytic properties.^[107–109]

Overall, doping of carbon-based catalysts with nitrogen has received more attention than doping with other heteroatoms due to three main advantages that promote the mechanisms of the OER and ORR.

- 1) Dipole–dipole interaction: The carbon atoms bonding with nitrogen could show higher positive charge density and stronger electron affinity, leading to higher catalytic activity toward the OER and the ORR.^[21,110]
- 2) Nitrogen hydrogenation: Previous studies implied that more than half of the nitrogen atoms experience a hydrogenation process at a specific potential that leads to destabilization of the surrounding carbon atoms, resulting in the generation of electrons during the process, and, thereby, facilitating the evolution of *OOH.^[21,111]
- 3) Modification of surface physicochemical properties: N doping can change the alkalinity, hydrophilicity, defectiveness, and/or electrical conductivity of carbon-based catalysts. It increases the charge migration on the surface of catalysts, which is in favor of electrochemical O_2 reduction and evolution.^[16,21,112]

Even though the role of different types of nitrogen for the enhancement of the OER and ORR performance remains to be fully clarified, it appears clear that N-doping is generally beneficial for carbon materials used in oxygen conversion applications.

2.4. Nitrogen-Induced Structural Defects

According to the second law of thermodynamics, disorder or intrinsic defects are non-negligible for crystalline materials.^[43] Indeed, various nanocarbon materials, including graphene and graphdiyne, are not devoid of extrinsic or intrinsic defects, regardless of their synthesis.^[27,113] Generally, defects exist in various forms that can be sorted by dimensionality as 0D (vacancies, adatoms, impurities), 1D (line defects), 2D (grain boundaries, twins), and 3D (voids, inclusions), all of which influence strongly adsorption, in both catalytic and chemical applications.^[27,114] Particularly, these defects may contribute to the enhancement of electrocatalytic activity due to the breaking of the structural symmetry and change of the local distribution of the π -electrons.^[113,115]

Among N-doped carbon-based electrocatalysts, N-induced incomplete-bonding defects such as monovacancy (MV), divacancy (DV), and Stone–Thrower–Wales (STW) defects dominate in various crystalline carbonaceous materials.^[116,117] Typically, in the vicinity of MV, three pyridinic N (Pyr-N₃, Figure 3c-1), each having double coordination with a C–N bond length of 1.33 Å, form a pentagon-like structure which is the most stable configuration for the N-dopants.^[118] Since Pyr-N₃ has fewer electrons compared to pristine graphene, in the form of MV defects it exhibits a p-type band structure.^[119] For N configuration around a DV defect, where two C atoms are removed, four pyridinic N collectively construct a porphyrinic-like planar architecture called porphyrinic N (Por-N₄, Figure 3c-2).^[119] Similarly, the electron deficiency of Por-N₄ results in an acceptor level that shows a p-type character. It is worth noting that several N-related impurities are likely spatially localized around the DV and form p-like orbital shapes localized at N atoms, causing diverse catalytic activities.^[120] Finally, STW defects generated by a simple 60° rotation of two carbon atoms, form two pentagons and two heptagons in the hexagonal graphitic lattice. In the case of STW defects, the N atom can be placed into a pentagon ring, which corresponds to a pyrrolic N (N_{py}, Figure 3c-3).^[116] Compared with other defects, the N_{py} configuration does not induce electron/hole-doping in the electronic structure due to the stabilization of defects by hydrogen atoms.^[121] N-dopants have exceptionally low energy barriers for guest molecules, rendering them superior catalyst dopants. A fascinating recent discovery for the application of N dopants-induced defects is their ability to initiate reduction/oxidation with the adsorption of molecules at the interface by charge transfer.^[122] Thus, creating these defects in a controlled manner may largely enhance the oxygen electrocatalytic activity.

Unfortunately, N-related active sites may be partly encapsulated in the inner carbon layer for some N-doped carbon materials, thereby restraining their catalytic activity.^[123] Therefore, nanocarbon structures with a higher edge exposure facilitate the incorporation of electrochemically active nitrogen into the carbon matrix.^[27,124] In addition to this, Stumm et al. incorporated N into the carbon network at diamond-like sites, where N-defects possess four neighbors in a tetrahedral configuration. N-doping resulted in slightly disordered fourfold sites and chains of many more sp² active sites, therefore increasing the Fermi level, which might result in a decrease in electrical conductivity.^[125] Normally, the edge sites themselves are not favorable to ORR activity, while the defects induced by edge-N play a crucial role in the enhanced reactivity.^[27,126] Increasing the exposure of edges with nitrogen-related defects and precisely modulating the location of N-doping is a promising strategy to boost the ORR/OER activity.

3. Applications of N-Doped Carbon-Based Oxygen Electrocatalysts

Sustainable energy conversion and storage technologies, such as unitized regenerative fuel cells (URFCs) and rechargeable metal–air batteries, are currently under intensive development due to their high efficiency, promising large-scale applications, and environmental friendliness.^[127,128] In addition to this, rechargeable

seawater batteries are emerging as a potential low-cost solution for energy storage devices in the marine environment.^[129] The OER and ORR reactions determine the efficiency of the energy conversion and storage systems. The general principles for these applications and the role that can play N-doped carbonaceous electrocatalysts in these are discussed below.

3.1. Oxygen Electrocatalysis in Regenerative Fuel Cells

URFC refers to a single electrochemical device that combines the functions of a fuel cell and an electrolysis cell.^[130–132] URFCs can serve as energy storage devices via water electrolysis, storing electricity in the form of chemical bonds, namely, hydrogen, and function as an energy conversion system producing electricity by utilization of the stored hydrogen.^[130,131,133] The ORR and the OER take place reversibly at the same electrode, playing the role of the cathode while functioning as a fuel cell (ORR), and of the anode when functioning as an electrolyzer (OER).^[130,131] URFCs still have to be further improved to reach a level of maturity of both fuel cells and electrolyzers in terms of energy efficiency and long-term performance. Currently, the major challenge of URFCs technology has been the insufficient performance of the bifunctional electrocatalyst, such as 1) low catalyst activities for both ORR and OER, that can determine the energy power, density, and efficiency of URFCs, 2) insufficient stability/durability of catalysts with a low resistance to physicochemical corrosion, resulting in a performance degradation, 3) poor product selectivity, 4) low cost-effectiveness, which is a key step to the commercialization of URFCs, and 5) nonestablished scale-up capabilities for catalyst production to meet the requirements on practical large scale production of catalysts. N-doped carbons used as ORR and/or OER electrocatalysts have tremendous advantages in the practical application of fuel cells due to their low cost, high efficiency and environmental friendliness.^[134] For instance, Sun et al. synthesized metal-free N-doped partly graphitized carbon as cathode catalyst for fuel cells by using waste cornstalks as the carbon source and melamine as the N source.^[135] The fuel cell test results demonstrated that the maximum power density of this catalyst is 1122 mW m⁻², which is higher than that of Pt/C (988 mW m⁻²) measured under the same conditions, showing a decline of only 10.2% after 80 days. Similarly, Tian et al. prepared metal-free N-doped carbon aerogel by one-pot template-free synthesis and assembled it into the fuel cell. An outstanding performance with the highest maximum power density of 967 ± 34 mW m⁻² (37.4% and 55.2% higher than platinum (Pt/C) and activated carbon, respectively) was obtained due to its superior surface area and increased micropores, as well as the highest pyridinic N and the lowest pyrrolic N content.^[136] In addition, Zhang et al. creatively prepared pomelo peel-derived porous N-doped carbon as cathode catalysts in fuel cells by rapid biomass conversion. The catalyst exhibited a power density as high as 907.2 mW m⁻² in a fuel cell, comparable to that of the costly Pt/C electrode (1022.9 mW m⁻²). Meanwhile, the long-term durability of this electrocatalyst allowed it to run continuously for 90 days, thus outperforming Pt/C.^[137] In addition to this, catalysts containing M–N–C-type moieties have attracted extensive attention for fuel cell applications due to their high performances.

For instance, Dresch et al. reported on anion exchange membrane electrode assembly tests in a reversible electrolyzer using Fe–N–C as catalysts. The initial round-trip efficiency decreased from 50% to 45% in the second cycle, which was superior to the performance of the two noble-metal reference catalysts (Pt and raveled Ir), indicating a higher reversibility of this catalyst.^[138]

3.2. Oxygen Electrocatalysis in Rechargeable Metal–Air Batteries

Rechargeable metal–air batteries are based on O₂–H₂O transformation chemistries in alkaline electrolytes, having a high theoretical energy density comparable to those of state-of-the-art lithium-ion batteries.^[139,140] Metal–air batteries consist of a pure metal or metal alloy electrode, which undergoes oxidation and reduction during discharging and charging processes, respectively, as well as an air–electrode coated by an electrocatalyst where the ORR and the OER take place during discharge and charge, respectively.^[139] Bifunctional oxygen electrocatalysts that are able to drive both the ORR and the OER at low overpotentials on the same electrode are thus required for regenerative energy technologies. Application and commercialization of rechargeable metal–air batteries remain challenged by a dearth of suitable bifunctional oxygen electrodes, exhibiting not only high activity toward the two reactions, but also having long-term stability under the operating conditions of both the ORR and the OER.^[141] The efficiency of oxygen conversion in rechargeable metal–air batteries is also limited by the inherent slow kinetics of the two reactions, resulting in a large energy barrier.^[142] The development of economical and robust non-noble metal and even metal-free electrocatalysts used in rechargeable metal–air batteries has attracted wide attention.^[139] Wang et al. prepared N-doped carbons as bifunctional oxygen electrocatalysts with large specific surface area and optimized porosity by a facile alkali activation method and used them in the assembled Zn–air batteries.^[143] The results displayed excellent performance among carbon-based metal-free oxygen electrocatalysts because of high pyridinic-N and graphitic-N contents and abundant edge defects, such as large peak power density up to 131.4 mW cm⁻², energy density as high as 889.0 W h kg⁻¹ at 4.5 mA cm⁻², and remarkable discharge–charge cycles up to 575 times. In addition, Lyu et al. developed a rechargeable Zn–air battery based on N, S codoped carbon as oxygen electrocatalysts, which delivered a maximum power density output of 149 mW cm⁻², a specific capacity of 769 mAh g⁻¹, and long charge–discharge capability at 5 mA cm⁻² with 600 cycles in 100 h, superior to an analogous battery prepared with the mixed Pt/C and IrO₂ (1:1 wt%) catalysts using the same mass loading.^[144]

3.3. Oxygen Electrocatalysis in Seawater Batteries

Seawater batteries are promising energy storage devices for sustainable energy storage applications due to their eco-friendly nature and access to abundant seawater on the earth, which contains low-cost sources of Na ion, used as charge carrier.^[145,147,148] Seawater batteries usually involve two oxygen reactions during operation: 1) OER upon charging and 2) ORR upon discharging, both occurring on the same electrode

immersed in seawater. During charging, Na⁺ ions move toward the cathode and are reduced to metallic Na, while the OER takes place at the anode. Meanwhile, during discharging, Na⁺ ions from Na⁰ oxidation migrate back to the anode (cathode during charging), as the ORR takes place on the cathode (anode during charging).^[129,149] The OER and ORR occurring at the water-electrode determine the overall cell performance, implying the importance of further developing suitable materials for oxygen conversion.^[147,149] Carbon-based materials are potential alternatives to noble metals for use in air electrodes when doped with nitrogen, which increases the charge delocalization and the density of donor states near the Fermi level without compromising the electronic conductivity of materials, thus increasing the electron-transfer rates and active site for reactants to largely enhance the device performance in seawater batteries.^[150] For example, Kim et al. prepared a pyridinic N rich few-layer graphene encapsulating cobalt catalysts, and used this catalyst as the electrode in seawater batteries.^[151] The results demonstrated an extremely low overpotential (0.56 V) at 0.1 mA and presented superior stability for 100 h with a mere 10% increase of voltage gap in rechargeable seawater batteries. Moreover, Khan et al. synthesized N, S codoped carbon nanospheres via the pyrolysis of melanosomes, exhibiting a distinctively higher performance when used as an air electrode in seawater batteries under ambient conditions, as well as an improved cell discharge potential due to the high surface area and improvement of spin density. Furthermore, the seawater battery cell operating in a flow mode with N, S codoped carbon nanospheres as electrode exhibits an overpotential gap of 0.56 V, a round-trip efficiency of 84%, a maximum power density of 203 mW g⁻¹, and an outstanding cycling stability for up to 100 cycles.^[150]

3.4. N-Doped Carbons as Bifunctional Oxygen Electrocatalysts

For all these applications, the design of high-performance yet low-cost bifunctional oxygen electrodes is essential. Some N-doped carbonaceous materials have shown promising perspectives in this direction. Heteroatom-doping of carbon materials provides electron redistribution on the pristine carbon framework due to differences in electronegativity between carbon and the dopant, and the resulting dipoles serve as active centers that interact with O₂ or oxygen-containing intermediates for further charge transfer, thus enhancing their performance as bifunctional oxygen electrocatalysts.^[152–155] In particular, nitrogen is regarded as an excellent dopant because the C–N dipole induces an electron redistribution beneficial for electron transfer in bifunctional oxygen electrocatalysis.^[4] N-doping may also increase the electrical conductivity, thus further reducing the energy input requirements.^[107,156,157] In general, bifunctional oxygen electrocatalysts require a small energy barrier between the involved intermediate species during the charge transfer steps to minimize overpotentials. Additionally, a high surface area with suitable electrode porosity is desirable in order to maximize the accessibility to active sites.^[14,158]

Lai et al. reported a unique, nitrogen-doped carbon nanocages-based bifunctional oxygen electrocatalyst (N-CNC-900) for rechargeable Zn–air batteries, which demonstrated enhanced bifunctional ORR/OER electrocatalytic performance

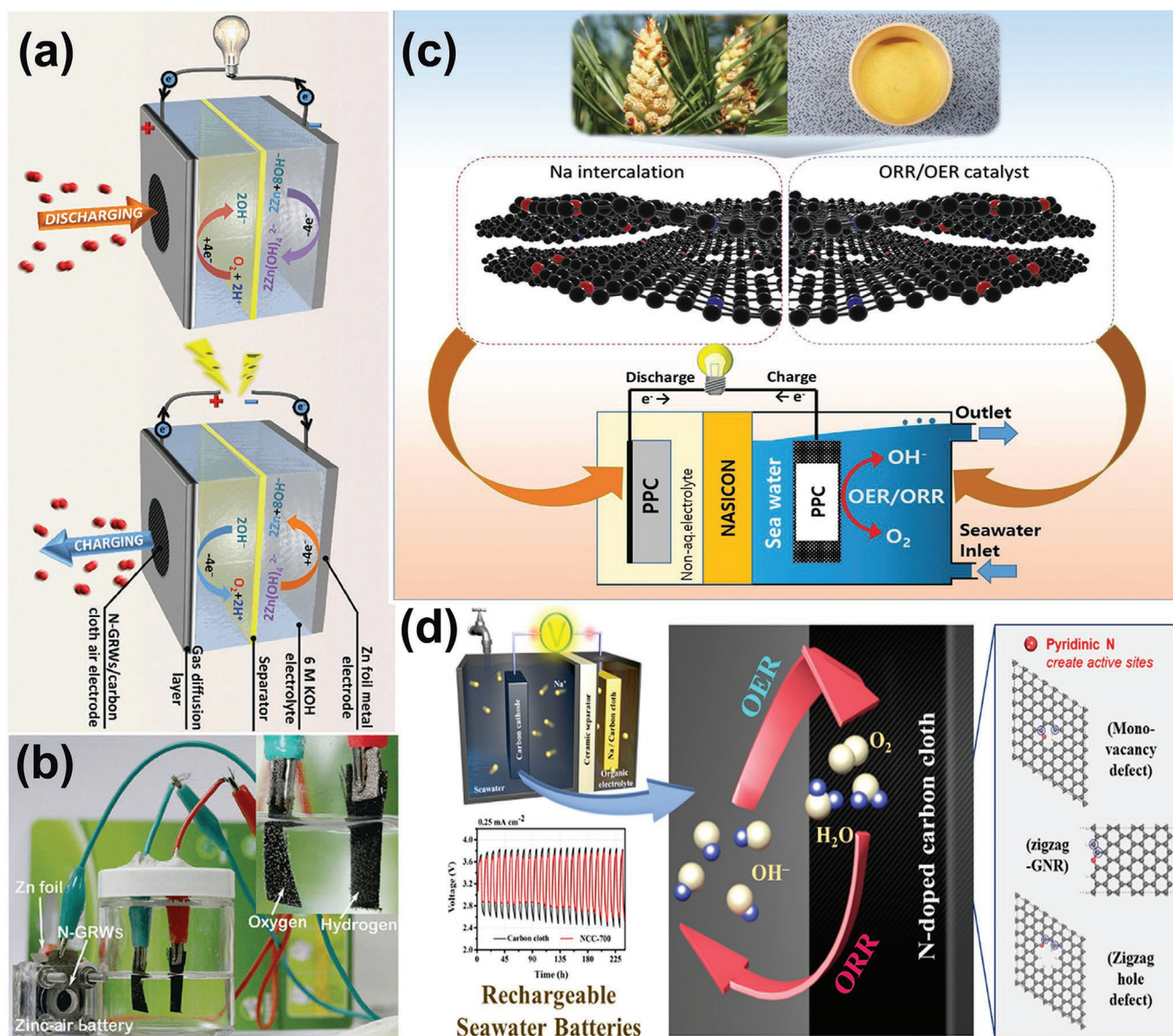


Figure 4. a) Schematic of an N-GRW bifunctional catalyst in rechargeable zinc–air batteries at charging and discharging conditions, and b) photograph of an electrolysis cell powered by a zinc–air battery. Inset shows the bubble formation on both cathode and anode electrodes. Reproduced with permission.^[31] Copyright 2016, American Association for the Advancement of Science. c) Strategies to reduce the cost and enhance the safety of the energy storage system with a seawater battery of bifunctional biomass carbon electrode. Reproduced with permission.^[145] Copyright 2021, Wiley-VCH GmbH & Co. KGaA, Weinheim. d) Schematic illustration of the OER and ORR process in seawater batteries for pyridinic nitrogen-containing carbon cathode. Reproduced with permission.^[146] Copyright 2020, American Chemical Society.

and long-term stability ascribed to the high degree and accessibility of pyridinic N (>50% of nitrogen content) active sites.^[159] Additionally, Zhong et al. developed a bifunctional oxygen electrocatalyst consisting of N-doped carbon nanotubes with encapsulated Ni nanoparticles, which exhibited superior bifunctional catalytic activity and long-term stability under alkaline conditions.^[160] Similarly, NH_3 -activated N-doped hierarchical carbon reported by To et al. presented a high bifunctional ORR/OER electrocatalytic activity in alkaline environments, with an excellent overall O_2 activity compared to commercial Pt/C catalysts.^[161] Therein, the authors estimated that the active sites for the ORR and OER originate from the N-doped defects and carbon intrinsic defects, respectively, where the concentration of

defects is modulated by controlling the degree of NH_3 chemical treatment. Furthermore, Yang et al. conducted the identification of catalytic sites in 3D N-doped graphene materials for bifunctional oxygen electrocatalysis (Figure 4a,b).^[31] ORR polarization curves measured from the 3D N-doped graphene materials (N-GRW) show a half-wave potential ($E_{1/2}$) of 0.84 V versus RHE. Note that more positive potentials represent lower overpotentials. Furthermore, the N-GRW electrode also demonstrated a high methanol tolerance, namely, much higher resistance to CO poisoning. As for the OER performance of the electrode, the overpotential required to drive a 10 mA cm^{-2} current density (η_{10}) for the N-GRW is 360 mV as shown in OER curves. In addition, the N-GRW catalyst showed superior durability

compared to Ir/C catalyst with <10% decay in the OER activity over 24 h of continuous operation, which is consistent with the electrocatalytic results before and after the stability testing. Thus, they confirmed that electron-donating graphitic N sites facilitated the ORR, whereas the electron-withdrawing pyridinic N species in the catalysts were assigned as the active sites for OER.

The importance of matching OER and ORR catalysts on the cathode of seawater batteries has been widely witnessed in the literature.^[162,163] For instance, Kim et al. synthesized a microporous N and P dual-doped carbon by simply heat-treating pine pollen, and this material was evaluated as an ORR/OER catalyst, thereby exhibiting superior activity and outperforming Pt/C (20 wt%) and commercial hard carbon electrodes.^[145] A full cell mounted with this catalyst as air-electrode material possessed an energy efficiency of 74% and a coulombic efficiency of 98% (Figure 4c).^[145] Furthermore, Tu et al. developed a pyridinic nitrogen-containing carbon coated onto carbon cloth as a bifunctional oxygen electrocatalyst via an annealing process (Figure 4d). Its electrochemical performance indicated a remarkable enhancement in the electrocatalytic activity toward the OER and ORR compared to that of a cell using the conventional carbon cloth.^[146]

Although progress has been made regarding N-doped carbons as electrocatalysts, their performance as bifunctional oxygen electrocatalysts is still relatively limited due to the difficulty of precise control on specific types of N configurations. It is urgently demanded to develop these materials toward more efficient, low-cost bifunctional oxygen conversion.

4. Synthesis of N-Doped Carbon-Based Oxygen Electrocatalysts

Up to now, various N-doped materials employed as ORR and OER electrocatalysts have been developed upon rational design of the structure, composition, surface functional groups, and morphology. The preparation methods commonly used to synthesize these materials are briefly introduced in this section.

4.1. Pyrolysis

Pyrolysis consists in controlling the thermal decomposition of materials at elevated temperatures conducted in an inert atmosphere such as N₂ or Ar. Pyrolysis is most generally used in the treatment of organic and organometallic materials, as illustrated by the example shown in Figure 5a.^[43] Typically, pyrolysis of organic substances produces volatile products and carbon-rich solid materials, and is often referred to as carbonization since carbon is obtained as the main residue. Pyrolysis is a handy and widely used method for the synthesis of a variety of functional carbon materials, and N-doping can be accessibly achieved by calcining the mixture of the carbon precursor and nitrogen source.^[43,164] The pyrolysis temperature, ramping rate, and duration have a critical impact on the composition, structure, and morphology of the as-made N-doped carbons.^[165] Li et al. reported a facile strategy to prepare nitrogen and phosphorus codoped graphene nanosheets (N, P-GCNS) by pyrolysis of a dried hydrogel which consisted of a mixture of graphene

oxide, polyaniline, and phytic acid (Figure 5c). Graphene oxide nanosheets were used as the precursor and structure-directing agent for coating polyaniline and phytic acid molecules during the polymerization of aniline monomers. Owing to the synergetic effects between the N and P atoms, as well as to the high active surface area, high electrical conductivity, and unique porous structure of this electrocatalyst, mass transport of both gas and electrolyte were favored.^[166] In addition to this, Li et al. prepared a flexible 3D sponge consisting of porous N-doped carbon microtubes with a high content of pyridinic and quaternary nitrogen via simple pyrolysis of facial cotton under NH₃ atmosphere.^[167] This material was employed as a bifunctional ORR/OER catalyst, exhibiting excellent electrocatalytic activity of the electrode toward the ORR with a potential of 0.89 V (vs RHE) at a current density of -3 mA cm^{-2} , as well as toward the OER, with a potential of 1.52 V (vs RHE) at a current density of 10 mA cm^{-2} . Moreover, it outperformed Pt/C and various reported carbonaceous electrodes for ORR/OER electrocatalysis due to its dictyophora-like structure, with a micrometer-scale, hollow core, and porous, well-graphitized tube walls, as well as fast electron transfer capability and abundant mass transport pathways due to its high-density of active sites. Nevertheless, and despite the huge progress already achieved, the fine control of the active site distribution remains one of the main challenges in the development of pyrolysis-derived N-doped carbons.^[43] Thus, pyrolysis, as a synthesis route for the fabrication of N-doped carbons for ORR/OER electrocatalysis, is considered to be in a development stage, and further research efforts are still required to optimize further this synthesis method.

4.2. Hydrothermal Carbonization

Hydrothermal carbonization (HTC), also named aqueous carbonization at elevated temperature and pressure, is a chemical process for the conversion of organic compounds to carbon materials (Figure 5b), employed frequently for the production of nanostructured carbons.^[43,44,169] HTC reactions happen in an aqueous medium, typically at temperatures above 100 °C and high pressure.^[170] According to the operating temperature, HTC can be divided into two main categories: 1) high-temperature HTC, ranging from 300 to 800 °C, which allows the preparation of carbon materials with a high degree of graphitization, and 2) low-temperature HTC, conducted at temperatures below 300 °C, which has been recently applied as a simple approach to prepare various functional carbonaceous fabrics for electrochemical applications.^[43,171,172] Huang et al. presented a hierarchical nitrogen-doped porous nanocarbon, using the biomolecule guanine and diverse carbohydrates (glucose, fructose, and cellulose) as carbon precursors.^[173] The materials were evaluated as ORR electrocatalysts, and it was found to be highly active toward the ORR with a superpositive half-wave potential of 0.87 V (vs the RHE) and a limiting current density of 5.9 mA cm^{-2} indicating hydroxyl as the main product, which is assigned to its remarkable nanosheet morphology, and independently of different elemental compositions and porosities.^[173] Furthermore, Qiao et al. adopted hydrothermal carbonization of chitosan to incorporate N-doped active sites in carbon nanotubes (NC-CNTs-1000; Figure 5d), thereby strengthening

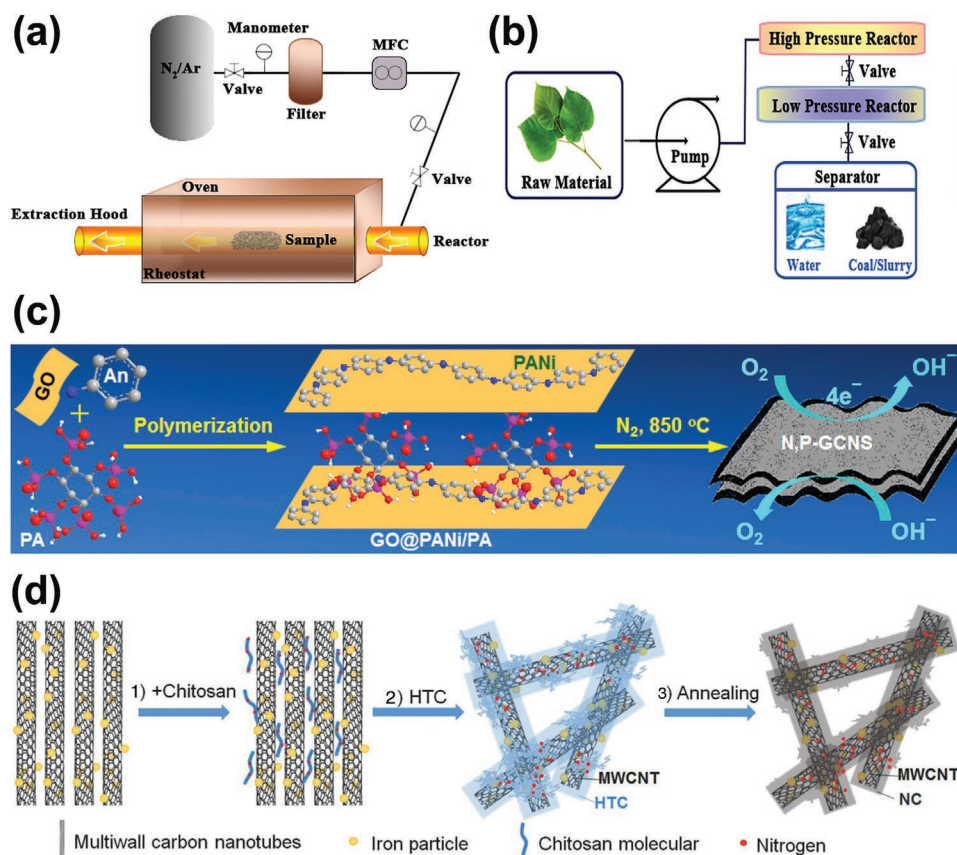


Figure 5. Schematic illustration of a) pyrolysis and b) hydrothermal processes. Reproduced with permission.^[43] Copyright 2020, Elsevier. c) Schematic illustration of the fabrication process and structure of N, P-GCNS bifunctional oxygen electrocatalyst. Reproduced with permission.^[166] Copyright 2015, American Chemical Society. d) Preparation steps of NC-CNT-1000: 1) addition of chitosan to MWCNTs; 2) hydrothermal carbonization (HTC) of the mixture of multiwalled carbon nanotubes (MWCNTs) and chitosan at 200 °C for 12 h; as-obtained material 3) after annealing at 1000 °C for 2 h followed by washing and drying, obtaining thus carbon nanocomposites. Adapted with permission.^[168] Copyright 2018, Wiley-VCH GmbH & Co. KGaA, Weinheim.

their ORR activity and stability in both alkaline and acid electrolytes.^[168] The resulting catalyst demonstrated enhanced ORR activity as the assembly of carbon nanotubes into a 3D network improved the mass transfer, alongside the formation of active nitrogen sites. The biggest advantage of hydrothermal carbonization is that, without an energy-intensive drying method, the precursor can be transformed to carbonaceous solids, thus facilitating rapid fabrication of N-doped carbons for ORR/OER electrocatalysis.

4.3. Chemical Vapor Deposition

Chemical vapor deposition (CVD) is a vacuum deposition method employed to produce high-quality solid materials, which are commonly used in the semiconductor and carbon nanomaterial industries to produce thin films and nanostructured solids.^[43,174] Generally, the substrate is exposed to one or more volatile precursors, which react and/or decompose on the substrate surface to produce favorable deposits in the CVD process (Figure 6a).^[174] Usually, volatile by-products are also generated, which can be removed by gas flow with inert Ar or N₂ through the reaction chamber.^[174] Besides the effect

of carbon precursors, the deposition temperature, carrier gas flow rate, and chamber pressure all play a significant role in the physicochemical properties of the as-prepared carbons.^[175] Tian et al. reported a new N-doped graphene/single-walled carbon nanotube hybrid material, fabricated by in situ doping during CVD, as a bifunctional ORR/OER electrocatalyst. This hybrid catalyst revealed a high ORR activity which is superior to commercial 20 wt% Pt/C catalysts, displaying higher durability and higher resistance to crossover effect, as well as high catalytic activity toward the OER (Figure 6c). The superiority of this high electrode-performance and low-cost oxygen conversion catalyst is attributed to its large specific surface area (812.9 m² g⁻¹) and high electrical conductivity (53.8 S cm⁻¹).^[176] Similarly, an N-rich nanocarbon was fabricated by CVD of nitrogen-containing compounds onto the pristine carbon nanotubes, which showed superior oxygen reduction performance due to full exposure of nitrogen active sites at the surface, as well as a synergic effect from their combination with the intact inner carbon walls.^[177] In addition to this, Kazakova et al. reported catalytic N-doped multiwalled carbon nanotube (N-MWCNT) growth using a mixture of ethylene and NH₃ (2–8 vol%) as the precursor. The obtained materials displayed differences not only in the concentration of nitrogen but also in their morphology and structural

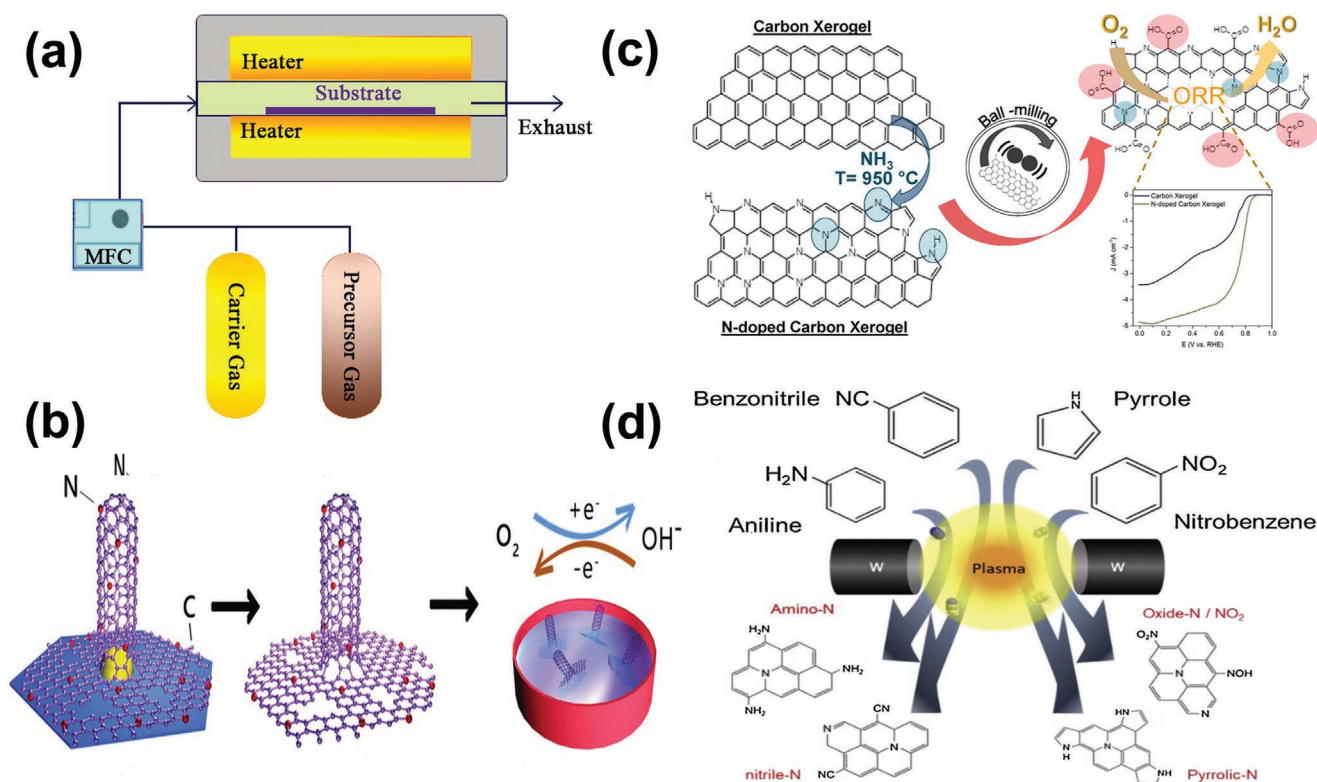


Figure 6. a) Schematic illustration of the CVD process. Reproduced with permission.^[43] Copyright 2020, Elsevier. b) Schematic diagram of ball-milling preparation and ORR process of N-doped carbon xerogels (Reproduced with permission.^[178] Copyright 2021, Elsevier. c) One-step growth of N-doped graphene/carbon nanotube hybrids for oxygen reduction and oxygen evolution reaction. Reproduced with permission.^[176] Copyright 2014, Wiley-VCH GmbH & Co. KGaA, Weinheim. d) Schematic diagram illustrating the preparation procedure of tailored N-doped carbon through a plasma process. Reproduced with permission.^[179] Copyright 2019, Elsevier.

characteristics, as well as in the surface chemical composition and defectiveness. The N-MWCNTs exhibited activity toward the ORR and OER, being the sample grown in the presence of 8 vol% NH_3 the one that displayed the lowest overpotentials for the two reactions.^[107] Generally, the nanocarbon prepared via CVD possesses a uniform graphitic structure and high electrical conductivity.

4.4. Ball Milling

Ball milling is a size reduction approach that involves the use of a rotating cylindrical chamber to mill materials to a fine powder.^[43] It is commonly used not only for grinding powders but also to synthesize oxides and nanocomposites including nanocarbon materials.^[180,181] In particular, this method has already exhibited various advantages for the preparation of N-doped carbon-based materials for ORR and OER.^[182] For instance, ball milling could mechanically reduce the size of carbon materials,^[183] favoring thus the subsequent modification by heat-treatment in the presence of nitrogen precursors.^[184]

Functionalization of material with nitrogen atoms by ball milling has also already been reported to synthesize N-doped carbon nanotubes.^[109] Due to its high N-pyridinic/N-quaternary ratio, this catalyst exhibited higher durability and methanol tolerance than Pt/C for ORR. Moreover, a carbon matrix can be

directly ball-milled in the presence of N_2 or NH_3 gas to produce active carbon species upon cleavage of graphitic C–C bonds and subsequent reaction with N_2 or NH_3 , forming thus N-doped carbons. For example, N-doped carbon xerogels were prepared by Eblagon et al. by ball milling using gaseous NH_3 as a nitrogen source (Figure 6b).^[178] The superior electrocatalytic properties of the N-doped carbon xerogels, suggested by increased diffusion-limited and kinetic current densities, originated from the high surface area of this catalyst, while overpotentials and the selectivity in terms of the number of electrons transferred were optimized by the highest ratio between quaternary N and pyrrolic N. Thus, ball milling could function as a low-cost and high-yield method for the massive production of defect-rich, N-functionalized carbons. It is important to note that the chemical and physical properties of ball-milled carbon nanomaterials strongly rely on the preparation conditions and the selection of suitable precursors for nitrogen doping through ball-milling.^[182]

4.5. Plasma Treatment

Plasma treatment is a state-of-the-art technique for the surface modification and functionalization of carbon materials, particularly in regard to the doping of nitrogen atoms and nitrogen-containing groups within a carbon matrix.^[185,186]

Plasma-related techniques are eco-friendly and energy-saving substitutes to existing energy-intensive and pollution-intensive synthesis methods.^[185] Plasma consists of ions, radicals, electrons, and neutral atoms, which are induced to produce instantaneously free radicals that can be used thereby to synthesize nitrogen-doped materials.^[186] Generally, carbon atoms are partially replaced with nitrogen atoms during plasma treatment. Li et al. creatively prepared N-doped carbon with amino N, pyrrolic N, nitrile N, and oxide N via a room temperature plasma synthesis process.^[179] This material displayed a high ORR activity in terms of overpotential and current density (Figure 6d), attributed to the high basic strength of amino N compared to the other studied C–N bonding structures. The nitrogen content in the carbon materials prepared via plasma treatment can be controlled by optimizing the exposure time and plasma strength, which therefore provides good flexibility for tuning the material properties.^[186]

4.6. Arc Discharge

The arc discharge technique is an effective, widely used method for the synthesis of carbon nanotubes and graphene nanosheets due to its simplicity and cost-effectivity. In a typical arc discharge synthesis, two graphitic rods acting as a negative cathode and a positive anode are placed a few millimeters apart from each other within an inert gas atmosphere, such as He or Ar. Then, a high current between the two electrodes is applied, vaporizing them and forming thus carbon-based products depositing around the chamber walls or over the cathode substrate as shown in **Figure 7a**.^[43,187–190] When flowing N₂ or another N-containing gas, or when nitrogen-rich graphite rod is involved in the preparation process, N-doped carbon materials can be rapidly available as the final products.^[43,189] Large-scale N-doped multilayered graphene sheets were obtained by Li et al. via the direct current arc-discharge method using pure graphite rods as electrodes, and NH₃ and H₂ as the buffer gas and as the reactive gas, respectively.^[191] The as-made graphene sheets were mainly of 2–6 layers and their sizes were about 100–200 nm. Additionally, the authors found that the content of N atoms on the multilayered graphene sheets can be modulated by simply changing the proportion between NH₃ and H₂ in the chamber atmosphere. Moreover, Ben Belgacem et al. adopted the arc discharge method for the deposition of boron and nitrogen codoped MWCNTs.^[187] The results demonstrated the desired presence of a significant amount of B- and N-doped CNTs in the cathodic deposit, which have a narrow diameter distribution of 20–30 nm and a length of up to 1 μm. Although the arc discharge is a high-yield approach for carbon materials, this method is extremely limited due to the requirement of high synthesis temperature and difficulty of purification of the products if metal elements are involved.^[43]

4.7. Biomass Conversion

Biomass is a superior alternative to fossil fuels to prepare a wide range of valuable chemicals and carbon materials, including porous carbons, hierarchical porous carbons, carbon

quantum dots, heteroatom-doped porous carbons, and carbon fibers.^[87] The biomass-derived synthesis methods for the fabrication of N-doped carbons offer several advantages compared to synthesis routes that require harsh and environmentally unfriendly reaction conditions. The biomass-derived method is a green and economically viable way to prepare N-doped carbon compared to other approaches.^[87,195] Moreover, this synthesis method allows incorporating additional treatments, with which the surface area and pore size can be further optimized.^[43,87]

Various biomass-based carbon precursors derived from natural plants or animals have been reported, including human hair,^[196] tea leaves,^[197] banana peels,^[198] coconut shells,^[199] and garlic stems.^[200] Gao et al. prepared a 3D porous sulfur, nitrogen codoped carbon using honeysuckles as the single precursor, as ORR electrocatalyst, demonstrating excellent ORR activity in alkaline medium with tolerance to methanol and stability superior to those of Pt/C. The high performance of this material was attributed to a high density of ORR catalytic sites resulting from nitrogen-doping, favorable reactant transport channels, and a fast electron transfer rate (Figure 7b).^[192] Additionally, Kaare et al. synthesized a highly active, wood-derived, N-doped carbon, which exhibited outstanding electrocatalytic activity toward the ORR with low overpotential and high current density, similar to that of a commercial Pt/C catalyst in an alkaline medium (Figure 7c).^[193] Similarly, Chen et al. designed N-doped nanoporous carbon nanosheets derived from plants (NCS-800). The resulting materials were used as ORR catalysts, exhibiting an unexpected and remarkably high ORR activity. In alkaline media, it demonstrated comparable catalytic activity but tolerance to methanol superior to commercial 20% Pt/C, while showing excellent catalytic activity, stability and tolerance to methanol in acidic media (Figure 7d).^[194] Furthermore, Ilnicka et al. prepared green algae and gelatine-derived nitrogen-rich carbon catalysts as ORR electrocatalysts, showing superior ORR performance in alkaline media compared to commercially available electrocatalysts.^[201] While biomass can be easily transformed into novel carbon nanostructures with superior ORR activity, it usually contains little or no nitrogen, requiring thus a second N-source that may result in poor homogeneity of the final materials due to the absence of molecular mixing.^[43,87] Meanwhile, fine structural control of carbons produced by this method is difficult to achieve. Particularly, graphitization degree, structure, and morphology are aspects of biomass-derived carbons that require further optimization.^[43]

5. Characterization of N-Doped Carbon-Based Oxygen Electrocatalysts

The identification of active sites and the elucidation of ORR and OER mechanisms requires the use of advanced characterization techniques sensitive to the structural, chemical and electronic properties of catalytic materials.^[202] Ex situ characterization of as-synthesized and post-ORR/OER catalysts provides information on the structure of the catalysts before and after the reaction. However, their structure may change drastically under ORR/OER conditions, namely, being exposed to electrolyte under an operating potential.^[203] In situ or operando characterization techniques provide insights into

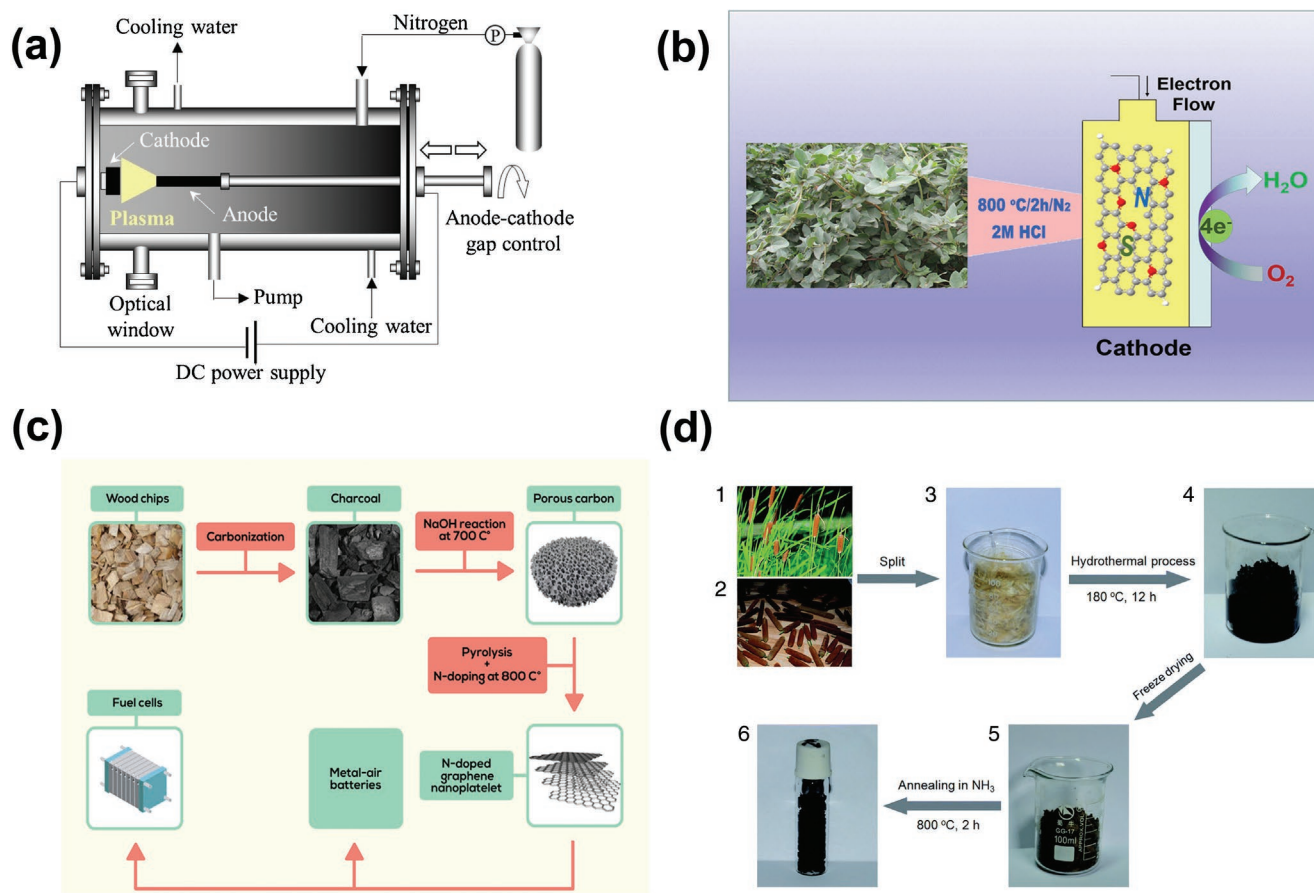


Figure 7. a) Schematic diagram of the arc discharge reactor. Boron and nitrogen-codoped carbon nanotubes are formed from the plasma between the cathode (left) and the composite anode (right). Reproduced with permission.^[187] Copyright 2016, Elsevier. b) The depiction of the transformation of honeysuckles into porous sulfur, nitrogen codoped carbon. Reproduced with permission.^[192] Copyright 2015, Elsevier. c) The depiction of the synthesis process for N-doped carbon from wood chips as carbon source and dicyandiamide as nitrogen source. Reproduced with permission.^[193] Copyright 2020, American Chemical Society. d) Preparation of the nitrogen-doped nanoporous carbon nanosheets: 1) images of the plant *Typha Orientalis*, 2) flower spikes, 3) raw material for hydrothermal process, 4) carbonaceous hydrogel, 5) carbonaceous aerogel, and 6) product NCS-800. Adapted with permission.^[194] Copyright 2014, The Royal Society of Chemistry.

the structure of the catalyst as well as the intermediates under the operating conditions of the ORR and OER.^[204] Vibrational spectroscopies such as infrared (IR) spectroscopy and Raman spectroscopy are particularly sensitive to carbon nanomaterials and were already applied to investigate nitrogen bonding in a wide range of carbonaceous electrocatalysts. X-ray photoelectron spectroscopy (XPS) and X-ray absorption spectroscopy (XAS) are element-sensitive spectroscopic techniques that can provide complementary information on the atomic chemical state, coordination environment and physicochemical nature. In this section, we discuss the application of ex situ and in situ/operando techniques for IR spectroscopy, Raman spectroscopy, XAS, and XPS to study the ORR and the OER driven by N-doped carbon materials.

5.1. Infrared Spectroscopy

IR spectroscopy consists in measuring the absorption (or transmission) of IR radiation in a material as a function of the frequency in the mid-IR range, where most vibrational modes of

organic and carbonaceous compounds absorb light.^[205] IR spectroscopy is used for the study of the structure of the catalysts but also for the identification of reaction intermediates.^[206,207] The ex situ characterization of carbonaceous compounds has been extensively applied to identify nitrogen sites in carbon matrix. The main attributions available in the literature are summarized in **Table 1**.

In addition to the identification of nitrogenous species on carbon nanomaterials, operando IR measurements were also used to observe the formation of active sites during the OER. Zhao et al. conducted an operando IR spectroscopy study on the OER mechanism over an amino-rich hierarchical-network carbon (amino-HNC) framework in an acidic electrolyte (**Figure 8a**).^[208] At open-circuit potential (OCP), absorption bands at 1267 cm^{-1} (stretching mode of C–N), 1130 cm^{-1} (stretching mode of C–C), and $850\text{--}1100\text{ cm}^{-1}$ (bending vibration mode of =C–H) are observed. Interestingly, at a potential of 1.35 V vs RHE, a new band appeared at 1546 cm^{-1} ascribed to the vibration stretching modes of C–O*. Furthermore, keeping amino-HNC at 1.35 V vs RHE for 3000 s did not change C–O* and C–N band, indicating their stability

Table 1. Main IR vibrational modes of N-doped carbonaceous materials and possible active sites for oxygen electrocatalysis.

Attribution	Frequency [cm ⁻¹]	Materials	Refs.
C–N stretching	1267	Amino-rich hierarchical network carbon	[208]
C–H ₂ N vibrational band	1248–1268	Amino-rich hierarchical network carbon	[208]
N–CH ₃ stretching	1372	N-doped carbon nanotubes	[209]
C–N stretching	1506	Plasma-tailored N-doped carbon	[179]
C–O* stretching	1546	Amino-rich hierarchical network carbon	[208]
C=N stretching	1593	Pyridinic N-doped graphene paper	[210]
C=C stretching	1620	3D metal/N-doped nanoplate carbon catalysts	[211]
C≡N stretching	2173	N-modified nanodiamond	[212]

under these conditions. However, the C–O* band disappeared when the potential returned to OCP, suggesting the formation of an H₂N–(*O–C)–C intermediate through the interaction of *O intermediates with H₂N–C=C sites under OER conditions. Moreover, the intensity of C–O* vibration is potential-dependent and increases with the applied potential (Figure 8b), which is due to a larger amount of *O species formed at higher potentials. Notably, a redshift of the C–NH₂ band from around 1267 to 1248 cm⁻¹ was observed as the potential increased due to the conformational variation of C–NH₂ modes resulting from a charge migration from C to NH₂. They proposed that the OER occurs via a four-electron transfer process with a H₂N–(*O–C)–C intermediate onto the H₂N–C=C active site. Figure 8c compares the potential dependence of *O formation with the charge migration. Interestingly, the charge

migration to H₂N–C=C occurred at a lower potential (1.25 V vs RHE) compared to the formation of *O. Furthermore, at potentials higher than 1.30 V vs RHE, the charge migration and *O formation are both enhanced proportionally to the potential increase, indicating a correlation between them. Zhao et al. thus concluded that charge migration from C to NH₂ promotes the formation of the crucial intermediate *O, on H₂N–(C=C) sites, forming H₂N–(*O–C)–C and leading to efficient OER.

Similarly, Su et al. prepared the acid-compatible electrocatalysts HNC–Co (hetero-N-coordinated Co single-site) and also used operando IR spectroscopy to probe a potential active site evolution of H₂N–(*O–Co)–N₄ during the OER process.^[213] The characteristic peaks of the HNC–Co electrode at around 1595, 1535, and 879 cm⁻¹ were observed at OCP (Figure 8d). When applying a potential of 1.38 V, another peak appeared

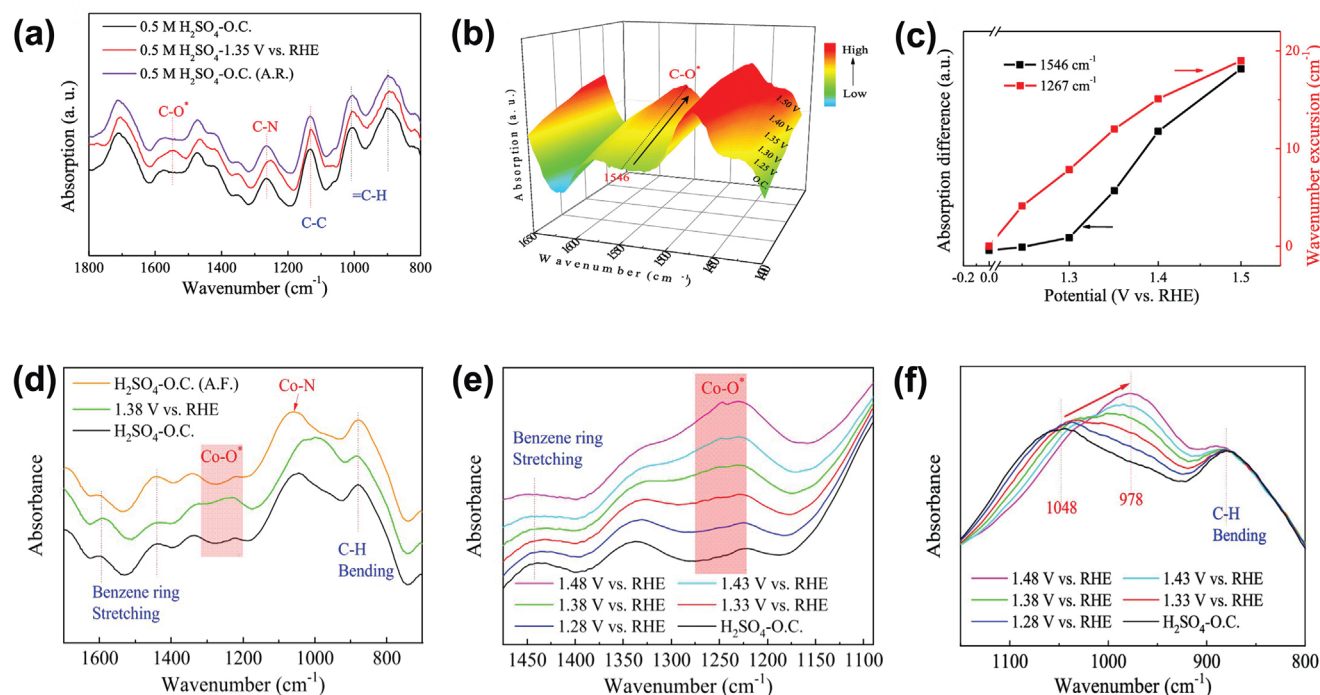


Figure 8. a) Operando IR spectra, b) IR signal in 1400–1650 cm⁻¹, c) evolution of the 1546 and 1267 cm⁻¹ absorption bands for amino-HNC. Reproduced with permission.^[208] Copyright 2019, American Chemical Society). d) Operando IR spectroscopy measurements. IR signals e) in the range of 1100–1500 cm⁻¹ and f) in the range of 800–1200 cm⁻¹ under various potentials for HNC–Co during the OER processes. Reproduced with permission.^[213] Copyright 2019, American Chemical Society.

Table 2. Main Raman vibrational modes of N-doped carbonaceous materials and possible active sites for oxygen electrocatalysis.

Attribution	Frequency [cm ⁻¹]	Materials	Refs.
Disordered carbons I peak	1100	Metal-free graphitized N-doped carbon	[220]
Defect-related D peak	1325	N-doped carbon black	[221]
	1336	Porous N-doped carbon derived from triazine-based polypyrrole network	[222]
	1344	Lignin-derived N-doped carbon	[223]
	1348	N-doped reduced graphene oxide	[224]
	1350	Phosphorus/N-doped carbon nanofiber composite	[225]
	1352	N-doped multiwalled carbon nanotubes	[226]
	Disordered carbons A peak	1510	Metal-free graphitized N-doped carbon
Ordered graphitic carbon G peak	1578	N-doped multiwalled carbon nanotubes	[226]
	1580	Phosphorus/N-doped carbon nanofiber composite	[225]
	1589	Porous N-doped carbon derived from triazine-based polypyrrole network	[222]
	1591	N-doped carbon black	[221]
	1593	N-doped hierarchical few-layered porous carbon	[228]
	1599	Lignin-derived N-doped carbon	[223]
	1600	N-doped reduced graphene oxide	[224]

at 1248 cm⁻¹ and was identified as a Co–O* intermediate. The potential-dependent IR spectra further uncovered that the intensity of the 1248 cm⁻¹ peak gradually increased with the enhanced overpotential, whereas the absorption peak at around 1048 cm⁻¹ gradually shifted to 978 cm⁻¹ at the same time (Figure 8e,f).^[214] This evolution was attributed to the adsorption of H₂O molecule on the H₂N–Co–N₄ moieties which was easily deprotonated and produced the *O intermediates over the H₂N–Co–N₄ moieties to form a structural evolution of H₂N–(*O–Co)–N₄, consequently promoting the formation of *OOH intermediates and the release of O₂ from the H₂N–Co–N₄ moieties.^[214]

5.2. Raman Spectroscopy

Raman spectroscopy is based on the characterization of inelastic scattering of monochromatic laser light after interaction with a sample.^[215] It is particularly well adapted to carbon materials because of its high sensitivity to the different carbon bonding and level of crystallinity.^[216] Generally, four bands are present in the Raman spectra of disordered carbon materials, namely, the graphitic (G) band (1580 cm⁻¹), defect (D) band (1350 cm⁻¹), D' band (sometimes denoted as G' band at around 1620 cm⁻¹), and 2D band (2680 cm⁻¹).^[217] The D band corresponds to carbon disorder and defects on the edge of graphene planar, while the D' band relates to the oxidation of sp² basal carbon. The 2D band reflects the interactions between graphitic planes and provides information on the stacking and the total number of graphene layers; however, it may also be influenced by the coverage of oxygen on the surface.^[218,219] Additionally, the intensity ratio of the D and G bands (I_D/I_G) can be used to calculate the crystallite sizes of carbon materials.

Raman spectroscopy is widely used for the study of N-doped carbon materials. The most relevant bands for N-doped

electrocatalysts are summarized in **Table 2** and we will provide some examples of in situ/operando Raman studies in the following. Zhang et al. studied the structure of N-doped graphene and evidenced a significant increase of the D band upon nitrogen incorporation.^[229] This indicates the formation of defects (i.e., bonding disorders and vacancies in graphene lattice) due to the N dopant. The D, G, and 2D bands in N-doped carbon materials are wider compared to pristine graphene due to the various bonding structures and defects brought by the N dopant. Kim et al. employed in situ Raman spectroelectrochemistry to probe any transient adsorbate–catalyst interactions that occurred during oxygen reduction.^[217] As the applied potential decreased from 0.83 to 0.63 V, noticeable changes in the spectra began to evolve at 0.78 V (**Figure 9a**), indicating the occurrence of a mild reduction of graphene oxide (mrGO)–adsorbate interaction consistent with the onset of ORR. Moreover, in situ Raman spectra of few-layered mildly reduced graphene oxide annealed at 600 °C (F-mrGO 600) during ORR (**Figure 9b**) also confirm that the active site for HO₂⁻ formation is related to edge site defects in F-mrGO(600). In contrast with the unannealed F-mrGO sample, a substantial increase in the intensity of the D band was observed once small cathodic overpotentials were applied with the change of increase of $I_D/(I_G + I_{D'})$ from OCP to 0.78 V (about 40 mV overpotential for HO₂⁻ formation). These results suggest that sp²-hybridized carbon (as has been ascribed to D' band broadening) located at the sheet edges interacts with adsorbed intermediates in this potential region.^[230]

In the past years, Raman spectroscopy has been used widely used for the investigation N-doped carbon-supported metal-based OER electrocatalysts.^[233–235] For instance, Lei et al. embedded NiFe nanoparticles on N-doped carbon nanotubes (NiFe/N-CNTs) as highly efficient OER and ORR catalysts for Zn–air batteries and used in situ Raman spectroscopy to investigate the origin of its high activity.^[231] **Figure 9c** shows the Raman spectra of NiFe/N-CNTs under different potentials.

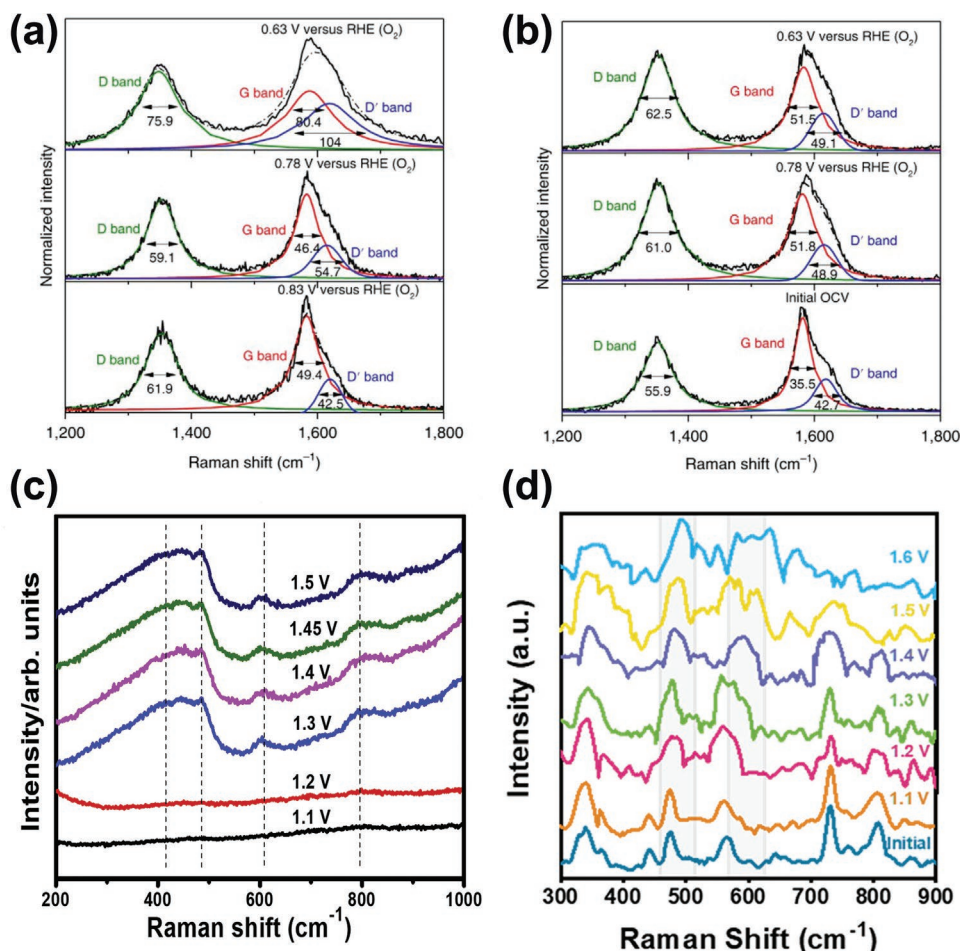


Figure 9. In situ Raman spectra—with calculated Voigt deconvolutions—of a) unannealed F-mrGO and b) F-mrGO(600) at various potentials. ORR occurs below 0.80 V. Oxygen-saturated (≈ 760 Torr) 0.1 M KOH was used as the electrolyte. Reproduced with permission.^[217] Copyright 2018, Springer Nature. c) In situ Raman spectra of NiFe/N-CNT under different applied potentials. Reproduced with permission.^[231] Copyright 2019, Elsevier. d) In situ Raman spectra (300–900 cm⁻¹) for Co/Co₂Mo₃O₈@NC as a function of potential versus RHE (1 M KOH). Reproduced with permission.^[232] Copyright 2021, American Chemical Society.

The bands ascribed to the adsorbed OH⁻ appear at potentials higher than 1.2 V vs RHE, which are absent over bulk NiFe catalysts. Furthermore, the OH⁻ bands gradually dissipate with decreasing potential suggesting the good cycle stability of NiFe/N-CNTs. The authors suggested the enhanced OH⁻ adsorption as the reason for the promoted OER performance.

Additionally, Zhang et al. investigated in detail the catalytic mechanism of Co/Co₂Mo₃O₈ embedded in N-doped carbon (Co/Co₂Mo₃O₈@NC) in an alkaline electrolyte. Figure 9d exhibits the obvious existence of a band at 474 cm⁻¹ when the applied voltage is as high as 1.2 V relative to RHE, which is attributed to the presence of Co(OH)₂. When the potential increases to 1.3 V, the band at 474 cm⁻¹ moves to 493 cm⁻¹, suggesting that Co(OH)₂ was transferred to CoOOH. If the potential rose from 1.0 to 1.3 V, new peaks appeared at 581 and 636 cm⁻¹, which corresponded to the existence of CoOOH. Therefore they speculated from the results that in Co/Co₂Mo₃O₈@NC, Co²⁺ and metal Co are the main active sites involved in the OER. The Co²⁺ and metal Co can greatly optimize the adsorption free energy belonging to the intermediate state, thereby improving the OER kinetics in an alkaline medium.

5.3. X-Ray Absorption Spectroscopy

XAS provides information on the unoccupied electronic states of the probed materials. X-ray absorption occurs when the energy of an incident X-ray photon coincides with the energy required to excite core electrons into an unoccupied electronic state. This technique is therefore element-specific and highly sensitive to the atomic chemical environment.^[236] In a one-electron description, the amplitude of the absorption edge depends on the amount of a specific type of atom and the numbers of holes/unoccupied states of the excited atom. For light elements such as carbon, nitrogen, and oxygen, the analysis of the X-ray absorption near edge structure (XANES) below the main absorption edge provides extensive information on the chemical bonding of the probed atoms.^[237] The most relevant features for N-doped materials available in the literature are summarized in Table 3.

XAS has been widely used to study the composition and structure of N-doped carbon materials. Lv et al. prepared pyridinic N-doped H-substituted graphdiyne (N-HsGDY) for ORR and studied the configuration of the doped N by XANES.^[62] The authors observed two peaks in the XANES, α and β ,

Table 3. Main XAS signature of N-doped carbonaceous materials and attribution to possible active sites for oxygen electrocatalysis.

Elemental category	Attribution	Energy [eV]	Materials	Refs.	
C K-edge	π^* transition of C—C or C=C bonds	285	N-doped carbon spheres	[238]	
		285.5	N-doped carbon nanosheets	[64]	
	π^* transition of C—H/C—NH ₂ bonds	285.6	Polymeric carbon nitride	[239]	
		π^* transition of C=N bond	287.6	N-doped carbon spheres	[238]
	π^* transition of N—C=N bond	287.8	Polymeric carbon nitride	[239]	
	π^* transition of C—O or C=O bonds	288.1	N-doped carbon spheres	[238]	
		289.0	N-doped carbon nanosheets	[64]	
	π^* transition of C—N—C or C—O—C bonds	288.4	N-doped carbon nanosheets	[64]	
		π^* transition of C—N bond	289.6	Polymeric carbon nitride	[239]
	N K-edge	π^* transition of pyridinic N	398–399	N-doped carbon nanosheets	[64]
			398.3	N-doped carbon spheres	[238]
			398.4	N-doped carbon nanotubes via high-temperature N ₂ annealing	[240]
			399.0	N-doped graphdiyne and carbon nanotubes	[241,242]
399.1			N-doped vertically aligned carbon nitride	[243]	
399.3			Pyridinic N-doped hydrogen-substituted graphdiyne	[62]	
π^* transition of amino-like N			399.4	N-doped graphene layers and Pt/NG composite	[244]
			399.5	N-doped single-layer graphene films	[245]
π^* transition of C=N bond			399.4	N-doped carbon spheres	[238]
			399.6	Polymeric carbon nitride	[239]
π^* transition of nitrile —C≡N			399.4–399.7	Carbon nitride thin films	[246]
π^* transition of pyrrolic N			399–399.3	N-doped carbon nanosheets	[64]
			399.5	N-doped graphene	[247]
π^* transition of quaternary N or graphitic N			399.7	N-doped graphene	[248]
			401	N-doped carbon nanotubes	[242]
	401.1	N-doped vertically aligned carbon nitride	[243]		
	401.5	N-doped carbon nanosheets	[64]		
	401.7	Polymeric carbon nitride	[239]		
	π^* transition of N—C bond	402.6	Polymeric carbon nitride	[239]	
	π^* transition of oxidized pyridine-like N	402.6	N-doped carbon nanotubes	[242]	
O K-edge	π^* transition of C—O or C=O bonds	530.9	N-modified graphene oxide	[249]	
		533.9	N-modified graphene oxide	[249]	

corresponding to the N 1s- π^* transition and the N 1s- σ^* transition of pyridinic N, respectively. Peak α splits into α_1 and α_2 because of the existence of different types of N at the edge or inside HsGDY. Additionally, Yang et al. used XAS to identify the active sites of N-doped graphene nanoribbon networks (N-GRWs) as bifunctional OER and ORR catalysts.^[31] Figure 10a,b presents the C and N K-edge XANES spectra of N-GRW pristine and after OER/ORR catalysis. The peaks in C K-edge XANES spectra are ascribed to A: defects, B: $\pi^*_{C=C}$, C: π^*_{C-OH} , D: π^*_{C-O-C} or $C-N$, E: $\pi^*_{C=O}$ or $COOH$, and F: σ^*_{C-C} (Figure 10). After OER/ORR, the intensity of the D peak (π^*_{C-O-C} , $C-N$) increased, indicating the adsorption of *O on C atoms (Figure 10a). Accordingly, a new peak (E) related to *OOH appeared. The N K-edge XANES spectrum (Figure 10b) indicates the presence of pyrrolic, pyridinic, and graphitic N in the fresh N-GRW sample. After ORR, a new peak (≈ 401 eV), ascribed to quaternary N, appears, which

results from the distortion of heterocycles due to the adsorption of *O and *OOH on the C atoms near the graphitic N. However, the peak of pyridinic N remained unchanged, suggesting that quaternary N, instead of pyridinic N, benefits the ORR. However, after OER, the full width at half maximum of the pyridinic N peak increased, and a new peak appeared on its higher energy side, while the other peaks remain unchanged, altogether suggesting that the *OOH and *O adsorbed on C atoms near the pyridinic N are responsible for the OER. Furthermore, in situ XAS was employed to elucidate ORR active site in Fe-N_x-C catalysts by Tylus et al.^[250] They observed that Fe-N_x-C catalysts comprised two Fe species, Fe-N₄ coordinated centers and Fe/Fe_xO_y nanoparticles. The shift of the absorption edge to higher energy with increasing potential, together with the observed electrochemical redox transition between 0.7 and 0.9 V vs RHE, indicated that a change in the oxidation state

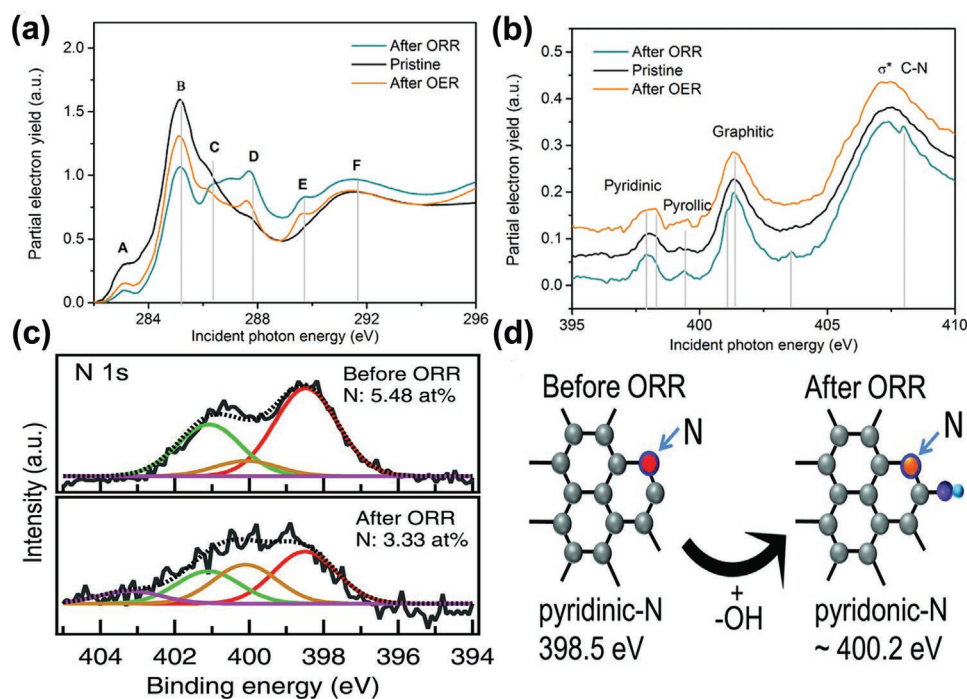


Figure 10. a) Carbon and b) nitrogen K-edge XANES spectra of N-doped graphene nanoribbon networks (N-GRW catalyst), acquired under ultrahigh vacuum, pristine (black line), after ORR (yellow line) and after OER (blue line). In carbon K-edge XANES spectra, A: defects, B: $\pi^*_{C=C}$, C: π^*_{C-OH} , D: $\pi^*_{C-O-C, C-N}$, E: $\pi^*_{C=O, COOH}$, F: σ^*_{C-C} . Reproduced with permission.^[31] Copyright 2016, American Association for the Advancement of Science. c) N 1s XPS spectra of N-doped highly oriented pyrolytic graphite (N-HOPG) model catalyst before and after ORR. d) Schematic representation of the formation of pyridonic N by the attachment of OH^- to the carbon atom next to pyridinic N. Reproduced with permission.^[90] Copyright 2016, American Association for the Advancement of Science.

of iron ($Fe^{2+}-N_4$ to $Fe^{3+}-N_4$) occurs during the ORR, whereas $Fe-N_4$ sites are saturated by the oxygenated species. Since both $Fe-N_4$ saturation and ORR overpotential take place at 0.9 V vs RHE, the authors proposed two possible situations. In the first one, $Fe-N_4$ sites are occupied by hydroxyl species derived from water activation, inhibiting thus the adsorption of O_2 . In the alternative situation, O_2 competes with the oxygenated species formed via water activation for $Fe-N_4$ active sites.

5.4. X-Ray Photoelectron Spectroscopy

XPS is a surface-sensitive technique commonly employed to study the oxidation state of a specific element in a material. It is based on the characterization of the energy of photoelectrons emitted from a material after its excitation by X-ray photons.^[251] As the escape depth of electrons is smaller than that of photons, XPS is more surface sensitive as compared to XAS. Generally, the binding energy of a photoelectron can be obtained by subtracting its kinetic energy from the energy of the incident X-rays. By measuring the kinetic energy, the binding energy can be obtained to elucidate the oxidation state of an element in a material.^[252] XPS is a useful tool for the investigation of ORR/OER driven by N-doped carbon materials. Typically, in the XPS spectra of N-doped carbon materials, pyridinic N, pyrrolic N, and graphitic N appear as well-resolved peaks located at around 398, 399, and 400 eV, respectively.^[253–255] The most relevant features for N-doped materials available in the literature are summarized in Table 4.

For instance, Davodi et al. synthesized N-doped CNTs for full water splitting and used XPS to elucidate the active sites.^[266] The corresponding N 1s spectra indicated that NCNTs contained graphitic and pyridinic N, as well as protonated imine N. Furthermore, the concentration of each N species, can be obtained through deconvolution. Guo et al. synthesized N-doped highly oriented pyrolytic graphite (N-HODP) and used XPS to investigate the intermediates formed on the surface of the material after using it as an ORR catalyst in an acidic electrolyte, revealing that the N 1s peak changed after ORR.^[90] The concentration of pyridinic N (398.5 eV) decreased from 54% to 38%, whereas that of pyrrolic/pyridonic N (400.1 eV) increased from 11% to 29%. Meanwhile, the total concentration of the pyridinic N and pyrrolic/pyridonic N species changed slightly from 65% to 67% (Figure 10c). Furthermore, it was proved that immersion in the electrolyte without applying a potential does not lead to a change in the N 1s spectrum of N-HODP, not only revealing a difference between its chemical and electrochemical stability, but also suggesting that the C atoms next to pyridinic N react with OH species, and pyridinic N transforms to pyridonic N as a consequence (Figure 10d). All these indicated that the C atoms next to the pyridinic N rather than pyridinic N are responsible for ORR. Similarly, Wütscher et al. reported the preparation of metal-free N-doped carbons by hydrothermal carbonization of cellulose followed by annealing in the presence of NH_3 .^[267] XPS studies confirmed the presence of pyridinic and graphitic N, and it was found that the ORR activity of the studied carbon materials benefited from a higher content of these N species.

Table 4. Main XPS signature of N-doped carbonaceous materials and attribution to possible active sites for oxygen electrocatalysis.

Elemental category	Attribution	Energy [eV]	Materials	Refs.	
C 1s	sp ² C bond	284.3	3D N-doped nanocarbons	[256]	
		284.8	N-doped graphene	[257]	
	sp ³ C bond	285.2	3D N-doped nanocarbons	[256]	
	C–OH bond	285.6	N-doped graphene	[257]	
	N-sp ² C bond	285.8	N-doped graphene	[258]	
		285.9	N-doped interconnected carbon nanofibers	[259]	
	N-sp ³ C bond	287.5	N-doped graphene	[258]	
	C=O bond	288.6	N-doped graphene	[257]	
	N 1s	Pyridine N	398.3	Functionalized N-doped interconnected carbon nanofibers	[259]
			398.4	N-doped carbon nanoparticle–carbon nanofiber composite	[260]
398.4			Fe-containing N-doped carbon	[261]	
398.5			Fe, N-doped carbon networks	[262]	
Amino N		399.5	N-doped carbon via a solution plasma process	[263]	
Pyrrolic N		400.2–400.4	400.3	N-doped carbon nanoparticle–carbon nanofiber composite	[260]
			400.4	Functionalized N-doped interconnected carbon nanofibers	[259]
		400.4	Fe-containing N-doped carbon	[261]	
		401.1	Fe, N-doped carbon networks	[262]	
		Quaternary N or graphitic N	401	N-doped carbon nanoparticle–carbon nanofiber composite	[260]
			401.5	Fe-containing N-doped carbon	[261]
			401.9	Functionalized N-doped interconnected carbon nanofibers	[259]
			402.1	Fe, N-doped carbon networks	[262]
		Pyridine N oxide	402.7	Nitrided-Ru nanoparticles implanted on N-doped graphitic sheet	[264]
			403	Fe-containing N-doped carbon	[261]
403.5			N-doped carbon nanoparticle–carbon nanofiber composite	[260]	
403.9			Fe, N-doped carbon networks	[262]	
403.9	Fe, N-doped carbon networks		[262]		
O 1s	C–O or –C=O bonds	532.7	N-doped carbon	[265]	
		533	Functionalized N-doped interconnected carbon nanofibers	[259]	
	N–O bond	533.9	N-doped carbon	[265]	
	N–C=O bond	535.4	N-doped carbon	[265]	

In addition to this, Xu et al. used XPS to investigate ORR driven by sputtered Fe–N–C films.^[268] XPS together with cyclic voltammetry showed that the Fe–N–C film comprised N–C (pyridinic N, graphitic N, and hydrogenated N), iron oxide, and iron nitride species. Additionally, they carried out an XPS analysis on the post-ORR catalyst. Fe species were not detected by XPS after ORR, indicating the dissolution of Fe species during ORR in an H₂SO₄ electrolyte. Furthermore, N 1s signal shifted to higher binding energy after the ORR, which is consistent with a protonated N and graphitic N. C 1s spectrum of the post-ORR catalyst showed the presence of a large amount of graphitic C, suggesting that graphitic species are the most stable C species under ORR conditions. Moreover, C–O and C–N species were also detected, and the O 1s spectrum showed an increase in the oxidation of the carbon matrix resulting from either corrosion due to the presence of peroxide intermediates, or the presence of N defects in the carbon matrix. More than that, Jain et al. gave a model reference on the combination of postreaction XPS and DFT, targeted at the detection of changes in the nitrogen species in N-doped carbons after applying potentials in O₂-saturated

acidic electrolyte.^[269] The results revealed interesting changes to the pyridinic, graphitic and pyridinic N⁺O[−] binding energy as a result of protonation of active sites and formation of ORR intermediates after conducting cyclic voltammetry with the catalyst in the ORR potential region.

6. N-Doped Carbon Catalysts for Oxygen Electrocatalysis

In this section, the different types of N-doped carbon-based electrocatalysts having shown the most promising properties for oxygen conversion over the last decade are reviewed.

6.1. N-Doped Graphene-Based Electrocatalysts

Graphene is a 2D nanosheet with superior properties such as high electrical conductivity and high surface area. After introducing nitrogen into the graphene backbone, the resultant

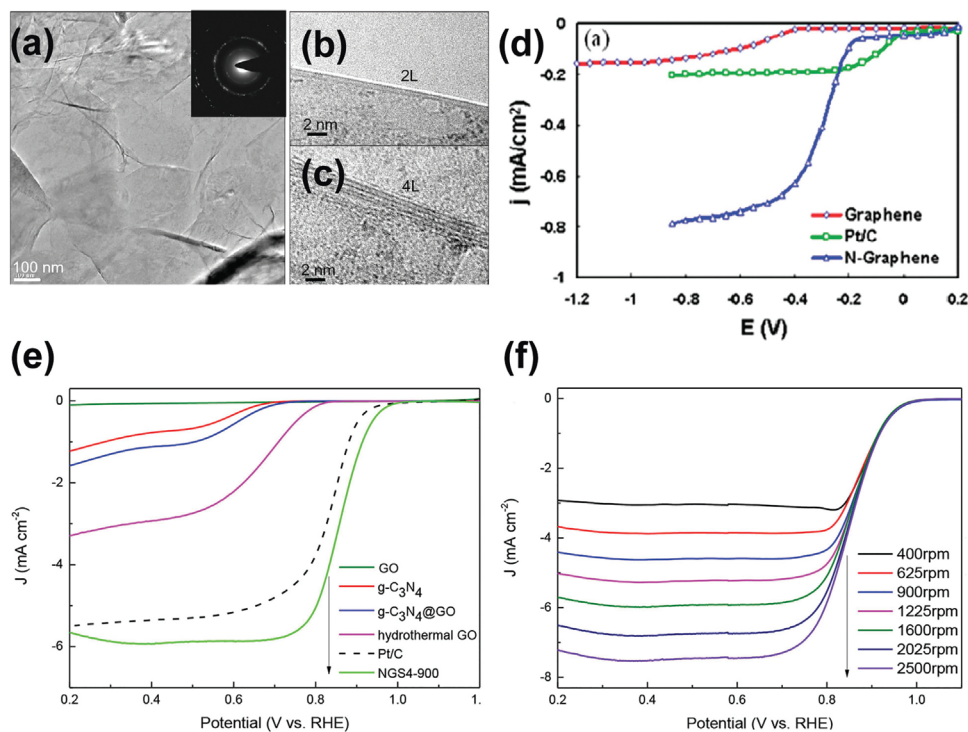


Figure 11. a) Low-magnification TEM image showing a few layers of a CVD-grown N-graphene film on a grid. Inset shows the corresponding electron diffraction pattern. b,c) High-magnification TEM images showing edges of the N-graphene film regions consisting of (b) 2 and (c) 4 graphene layers (L). d) Rotating disk electrode voltammograms for the ORR in air-saturated 0.1 M KOH at the C-graphene electrode (red line), Pt/C electrode (green line), and N-graphene electrode (blue line). Electrode rotation rate: 1000 rpm. Scan rate: 10 mV s⁻¹. Mass (graphene) = Mass (Pt/C) = Mass (N-graphene) = 7.5 μg. Reproduced with permission.^[30] Copyright 2010, American Chemical Society. e) Linear sweep voltammograms of the prepared catalysts and commercial 20 wt% Pt/C obtained on 1600 rpm rotating disk electrode in O₂-saturated 0.1 M KOH with 10 mV s⁻¹, and f) LSV curves of NGS4-900 on different electrode rotation rates. Reproduced with permission.^[36] Copyright 2018, American Chemical Society.

N-doped graphene exhibits excellent electrocatalytic activity, particularly for the ORR.^[270] Recently, much effort has been devoted to investigating the electrocatalytic applications of this kind of material, and a large amount of 2D N-doped graphene-based materials have been reported to date. In 2010, Qu et al. proposed a facile CVD approach to fabricate large-area N-doped graphene films (Figure 11a–d).^[30] The obtained N-graphene film possessed a layered structure that can be easily transferred onto different substrates. Electrochemical data showed that the N-graphene film exhibited superior ORR electrocatalytic activity and stability, outperforming commercial Pt/C. In 2011, Sheng et al. found a facile and low-cost method to large-scale fabricate N-doped graphene.^[271] Upon optimization of the synthesis conditions, the nitrogen content in graphene could reach 10.1%, mostly in the form of pyridine N, leading to high ORR electrocatalytic performance. In 2014, Wei et al. designed and synthesized mesoporous N-doped carbon nanosheets by templated synthesis method.^[35] The obtained ordered, porous structures generated abundant catalytic sites, which facilitated the electron/mass transfer during the ORR. Therefore, the catalyst exhibited a low overpotential of –0.01 V (vs Ag/AgCl) and prominent catalytic activity and durability even under acidic conditions, rendering it a promising metal-free catalyst to replace Pt/C. Moreover, in 2016, Guo et al. conducted an in-depth investigation of the ORR properties of graphite with a highly conjugated structure and N-doped graphene nanosheets.^[90] They confirmed that the ORR

active sites of N-doped graphene nanosheets were mainly based on pyridinic N. Besides, carbon atoms with Lewis basicity also exhibited catalytic activity but were inferior to pyridinic N.

Higher accessibility of active sites also improves the electrocatalytic activity, as demonstrated for 3D N-doped graphene materials with hierarchical structures. In 2017, Qin et al. prepared porous holey N-doped graphenes (PHNGs) by simply pyrolyzing urea and magnesium acetate tetrahydrate.^[29] The PHNGs exhibited abundant out-of-plane pores and interpenetrated holes. Furthermore, the nitrogen doping degree was modulated by means of post-treatments, such as plasma treatment, hydrothermal method, and a CVD method.^[171,174,185] As previously discussed, the ORR activities of PHNGs largely depended on the content of pyridinic nitrogen, and was improved by the combination with quaternary nitrogen. In 2017, Xiang et al. prepared a 3D N-doped graphene-based, gel-like hybrid by pyrolyzing an assembly of g-C₃N₄ on graphene oxide (Figure 11e,f).^[36] The obtained catalyst demonstrated the uniform distribution of N atoms, a high pyridinic N content, and abundant edge-rich defects. As a result, the catalyst showed good ORR activities with a half-wave potential ($E_{1/2}$) of 0.859 V, outperforming $E_{1/2}$ of 0.848 V in Pt/C and other metal-free carbon catalysts at that time. Further data showed that appropriate doping configuration (mainly pyridinic N) and location played a critical role in enhancing the ORR activity. Recently, Mohamad et al. utilized a polymer-assisted electrophoretic

exfoliation technique to fabricate N-doped graphene.^[32] The abundant graphitic nitrogen atoms directly enhanced the electrolytic ORR activities and the prepared material showed excellent stability toward methanol crossover and high durability. As an air cathode in Zn–air batteries, it also exhibited high peak power density, illustrating thus its potential applications as an ORR catalyst in fuel cells and metal–air batteries.

6.2. N-Doped CNTs-Based Electrocatalysts

CNTs have raised worldwide attention because of their large surface area, high electrical conductivity, and unique 1D hollow structure, all of which are highly relevant for applications in electrocatalysis. Various CNTs-based electrocatalysts have been developed as ORR catalysts, particularly N-doped CNTs. In 2009, Gong et al. designed and synthesized vertically aligned nitrogen-containing CNTs (VA-NCNTs) and investigated their electrocatalytic activity toward the ORR.^[25] The obtained catalysts demonstrated electrocatalytic activity and stability superior to those of Pt, exhibiting a steady output potential of -80 mV and a current density of 4.1 mA cm⁻² at -0.22 V (vs Ag/AgCl). These good performances were attributed to positive charge density on the aligned NCNTs induced by electron-withdrawing nitrogen atoms. In 2011, Wang et al. discovered that nitrogen atoms can facilitate the self-assembly of tubular carbon nanostructures.^[272] By virtue of this, they produced N-doped CNTs with high nitrogen content using melamine as a precursor. As electrocatalysts, the NCNTs exhibited excellent ORR activity, stability, selectivity, and resistance to CO poisoning, illustrating their potential in fuel cell applications.

Combined with other carbon materials, the electrocatalytic properties of N-doped CNTs can be enriched. In 2020, Chang et al. prepared carbon nanohybrids by a facile mechanical technique, generating cut and exfoliated N-doped CNTs with abundant edge-N-rich structures as ORR active sites.^[273] By integrating CNTs with N-rich graphene nanoclusters, Gong et al. obtained a graphene nanoclusters-CNTs (GN-CNTs) hybrid with a high abundance of active N species.^[274] The incorporation of defects/edges into the CNTs structure can influence the degree of N-doping as well as the ORR performance. Therefore, the optimized GN-CNTs delivered a high catalytic activity with $E_{1/2}$ of 0.84 V (vs RHE) and durability. Nguyen and Shim designed and synthesized an N-doped carbon quantum dots/multiwalled carbon nanotubes (CDs/CNTs) hybrid by a facile and scalable synthesis method.^[275] The obtained CDs/CNT exhibited excellent ORR activity ($E_{1/2} = 0.834$ V vs RHE) with favorable kinetics, as well as high durability ascribed to the synergistic effect of CDs and CNTs. Shui et al. incorporated vertically aligned N-doped carbon nanotubes (VA-NCNTs) in combination with N-doped graphene (Figure 12a,b).^[8] This hybrid was evaluated in PEM fuel cells, showing a high activity ($E_{1/2} = 0.87$ V vs RHE) and durability in acidic conditions. Besides ORR activity, N-doped CNTs have also exhibited OER activity and can be used in rechargeable Zn-air batteries. Pendashteh et al. fabricated CNTs fiber fabrics via a hydrothermal method (Figure 12c–f).^[276] By optimizing the nitrogen doping degree and the density of defects, CNT fabric containing abundant pyridinic nitrogen and sp³ carbons showed outstanding ORR/OER activities ($E_{10} = 1.59$ V and $E_{1/2} = 0.78$ V

vs RHE). When the catalyst was employed as air cathodes, the Zn–air battery presented a high capacity of 698 mAh g⁻¹, an energy density of 838 W h kg⁻¹ as well as excellent stability.

6.3. N-Doped CDs-Based Electrocatalysts

Carbon quantum dots (CDs) are 0D carbon materials that possess alterable electronic structures and abundant catalytic sites due to their small size.^[277] Many theoretical works have been devoted to the electrocatalytic properties of N-doped CDs which were reviewed elsewhere.^[277] In particular, Saidi et al. found that the most active sites for ORR in N-doped CDs for the four-electron transfer pathway originated from pyridinic and graphitic nitrogen with overpotentials of 0.55 and 0.79 – 0.90 V, respectively, in accord with experimental investigations.^[41] In 2016, Noffke et al. identified that solvation around the active sites and the pH largely determined the selectivity of N-doped graphitic carbon as an ORR catalyst.^[278] In 2021, Guo et al. investigated the four-electron and two-electron reduction pathways of ORR for N- and N/S-codoped CDs by DFT methods.^[279] Once again, the electrocatalytic activity was mainly ascribed to pyridinic N doping sites. They found that the codoping of S and N atoms induced asymmetric spin and charge density distribution, leading to an enhancement of their ORR catalytic performances.

N-doped CDs can be synthesized by several preparation methods. Solution chemistry enabled a great control on the numbers of nitrogen atoms and their bonding configurations in N-doped CDs.^[40] The N-containing CDs 1, 2, and 11 shown in Figure 13a,c showed ORR onset potentials at -0.04 , -0.10 , and -0.14 V, respectively, relative to that of the commercial Pt/C catalyst. In 2014, Hu et al. synthesized a hybrid catalyst of graphene and N-doped CDs through a hydrothermal approach (Figure 13d,e).^[39] The N-doped CDs on graphene acted as the catalytic active sites for ORR driving the reaction mainly through a 4-electron transfer pathway, as well as exhibiting high selectivity and stability, outperforming Pt-based catalyst in an alkaline medium. A microwave-assisted hydrothermal approach was also employed by He et al.^[280] The resulting N-CDs exhibited a high degree of crystallinity and a large number of N atoms. Moreover, the abundant pyridinic N endowed the N-CDs with a promising onset potential of -0.121 V (vs RHE) for ORR.

6.4. Carbon Nitride-Based Electrocatalysts

Graphitic carbon nitride, also denoted as g-C₃N₄, is a highly ordered polymer typically built upon polymerization of nitrogenous precursors, e.g., melamine or cyanamide. Its high nitrogen content, tunable conjugated structure and environmental friendliness render it a promising catalyst in photo and electrochemical applications.^[281] They however suffer from a low electrical conductivity and are therefore often combined with conductive carbon materials. Carbon nitride-based materials have already shown superior electrocatalytic activities,^[37,282–284] and their electrocatalytic properties toward the conversion of oxygen were recently reviewed.^[281,283] Among the most prominent studies, Yang et al. designed and synthesized graphene-based carbon nitride nanosheets by virtue of silica template

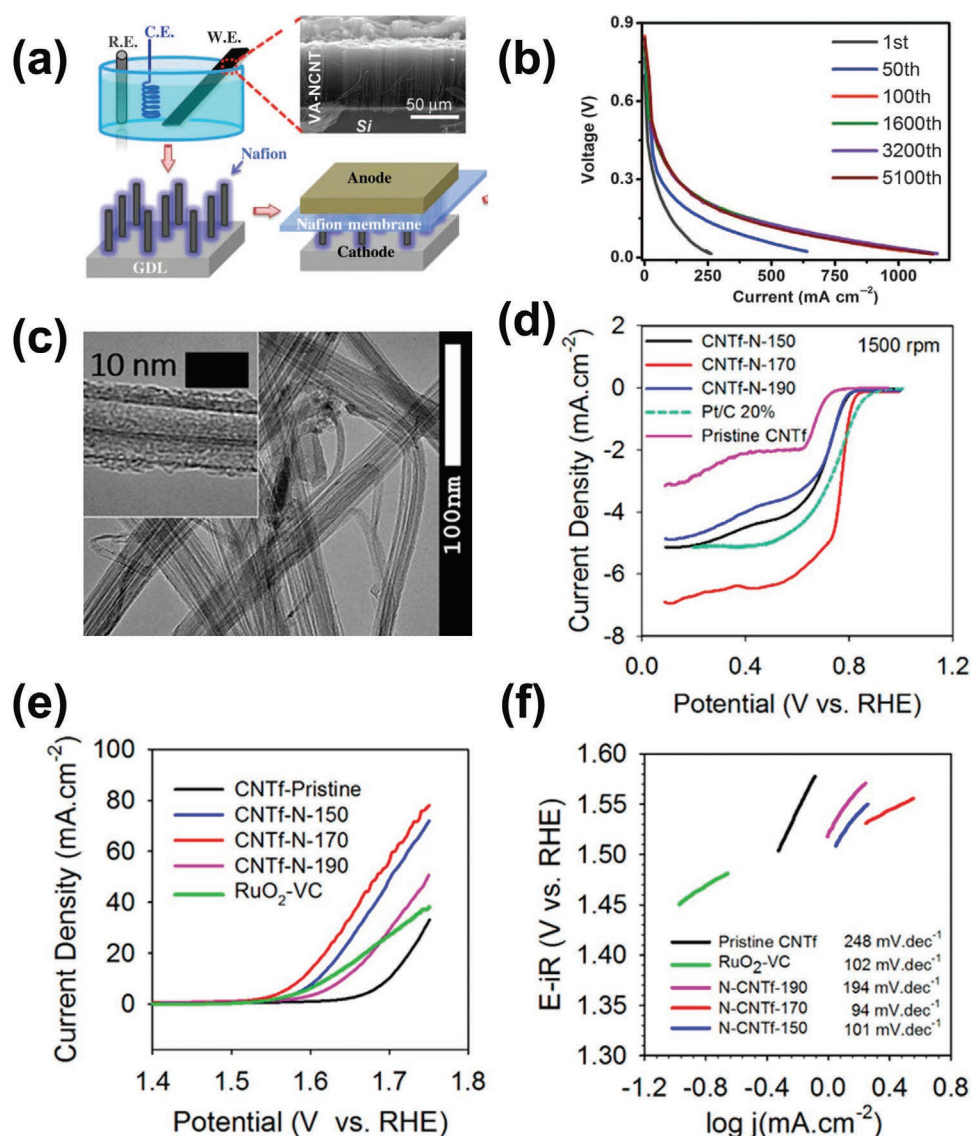


Figure 12. a) Schematic drawings for the fabrication of membrane electrode assembly from vertically aligned nitrogen-doped carbon nanotubes (VA-NCNT) arrays and the electrochemical oxidation to remove residue Fe. C.E., counter electrode; R.E., reference electrode; W.E., working electrode. The top right in (a) is a typical SEM image of the VA-NCNT array. b) Polarization curves as a function of the current density after accelerated degradation by repeatedly scanning the cell from open-circuit voltage to 0.1 V at the rate of 10 mV s⁻¹. Reproduced with permission.^[8] Copyright 2015, American Association for the Advancement of Science. c) TEM images of treated CNT fiber at 170 °C (N-CNT f-170). d) Linear sweep voltammograms of pristine and treated CNT fibers and commercial Pt/C 20% at a rotation rate of 1500 rpm with a scan rate of 20 mV s⁻¹. e) LSV curves of various samples in Ar-saturated 0.1 M KOH solution, showing OER catalytic activity of electrode. f) Tafel plots of OER LSV curves in panel (d). Reproduced with permission.^[276] Copyright 2018, American Chemical Society.

that showed high durability and selectivity (Figure 14a,b).^[285] In the same year, Zheng et al. fabricated metal-free mesoporous g-C₃N₄@carbon nanorods with higher catalytic efficiency than a Pt/C catalyst (Figure 14c,d).^[37] Later, Tahir et al. synthesized 1D g-C₃N₄ as nanofibers and tubular structures with good wettability and abundant active sites, improving the ORR performance.^[286] The tubular structures exhibited higher ORR activity than nanofibers due to the higher availability of active sites and higher surface area. The g-C₃N₄ demonstrated higher durability and methanol tolerance compared to Pt/C.

Carbon nitride-based materials also exhibit promising electrocatalytic properties toward the OER, as well as for bifunctional

ORR/OER catalysts. In 2014, Ma et al. reported the hybridization of g-C₃N₄ nanosheets and CNTs using a self-assembly method to form a metal-free OER catalyst (Figure 15a,b).^[84] The ultrathin g-C₃N₄ nanosheets facilitate the formation of a 3D interconnected porous framework, endowing the hybrid with abundant catalytic centers and enhanced charge/mass transfer. As a result, the catalyst demonstrated outstanding activity with 1.60 V vs RHE at 10 mA cm⁻² and stability, which surpassed those of IrO₂ supported on CNTs. In addition to this, Wahab et al. synthesized a well-ordered mesoporous carbon nitride material with a uniform pore size of 4.56 nm and high nitrogen content following a nano hard-templating approach

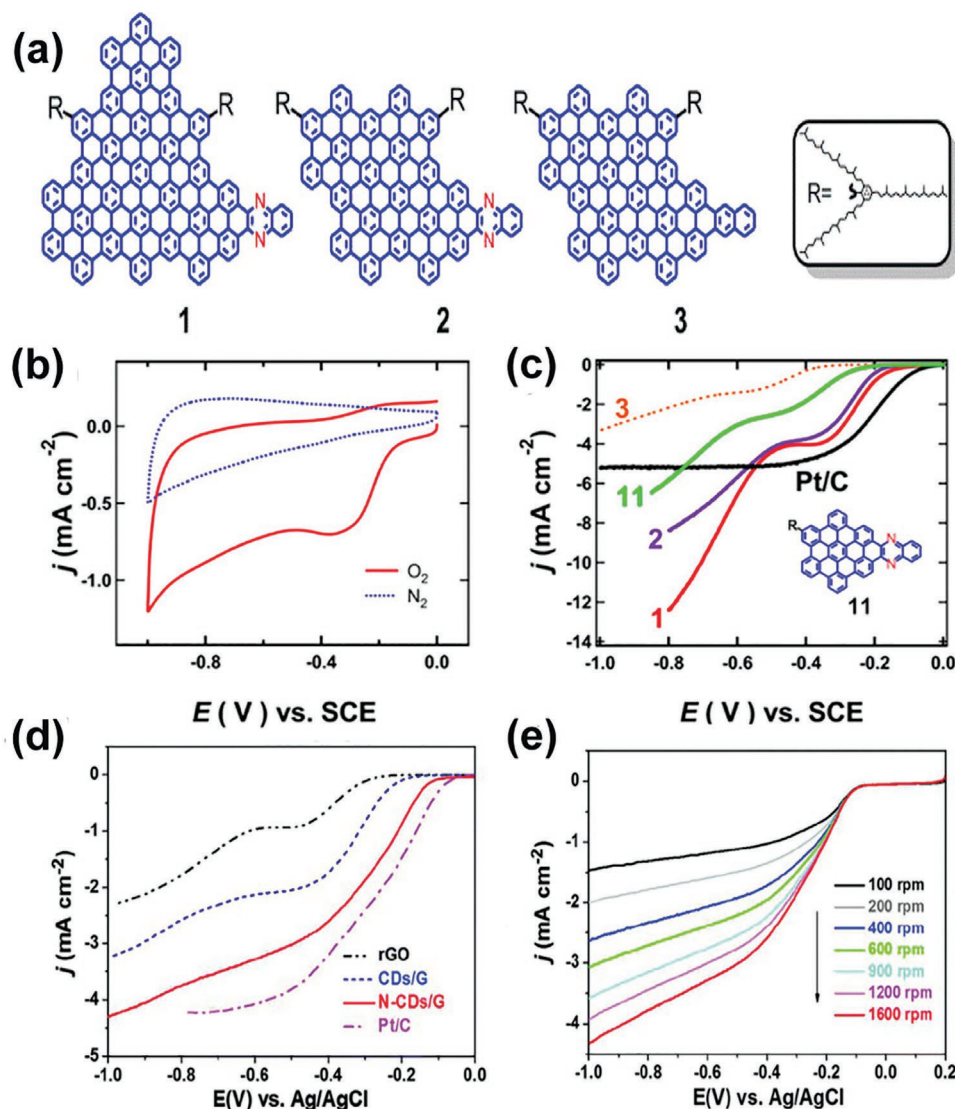


Figure 13. a) Structures of (1,2) N-doped and (3) undoped graphene quantum dots (CDs) for comparison studies. b) Cyclic voltammograms of 1 deposited onto a glassy-carbon rotating disk electrode recorded at a scan rate of 50 mV s^{-1} in N_2 - and O_2 -saturated 0.1 M KOH solutions. c) Linear sweep voltammograms of 1–3 and Pt/C (black) recorded at a scan rate of 10 mV s^{-1} with a rotating rate of 1600 rpm in an O_2 -saturated 0.1 M KOH solution. Also shown is the voltammogram of a much smaller N-substituted heterocycle 11 with the structure shown in the inset. Reproduced with permission.^[40] Copyright 2012, American Chemical Society. d) Rotating disk electrode voltammograms of rGO, CDs/G, N-CDs/G, and Pt/C recorded in an O_2 -saturated 0.1 M KOH solution at a rotation rate of 1600 rpm and 10 mV s^{-1} scan rate. e) Rotating disk electrode voltammograms of N-CDs/G at different rotation rates. Reproduced with permission.^[39] Copyright 2015, The Royal Society of Chemistry.

(Figure 15c).^[284] This mesoporous carbon nitride catalyst demonstrated high OER activity (1.606 V vs RHE at 10 mA cm^{-2}) with a Tafel slope of about 52 mV dec^{-1} . Moreover, the material showed high durability after 24 h chronoamperometric test, illustrating its potential applicability in the field of water electrolysis. In another approach, Shinde et al. developed carbon nitride sponges, sandwich-type catalysts doped with P and S by a facile polymerization method (Figure 15d–f).^[38] The codoping with P and S alongside an efficient mass/charge transfer of the 3D structures imparted the electrodes with ORR (half-wave potential = 0.87 V) and OER (overpotential = 0.33 V at 10 mA cm^{-2}) catalytic activities that proved to be superior to Pt/C and RuO_2 electrode for bifunctional oxygen

electrocatalysis. Besides, when employed as air–electrode material in zinc–air batteries, the catalyst exhibited a high specific capacity of 830 mAh g^{-1} , a power density of 198 mW cm^{-2} , and an open-circuit voltage of around 1.51 V . In addition to this, the zinc–air batteries assembled with this catalyst showed superior stability and reversibility after 500 charge/discharge cycles.

6.5. N-Doped Graphdiyne-Based Electrocatalysts

As a new 2D carbon material, graphdiyne (GDY) has aroused extensive attention. It consists of sp^2 - and sp -hybridized carbon atoms, which endow it with prominent chemical and physical

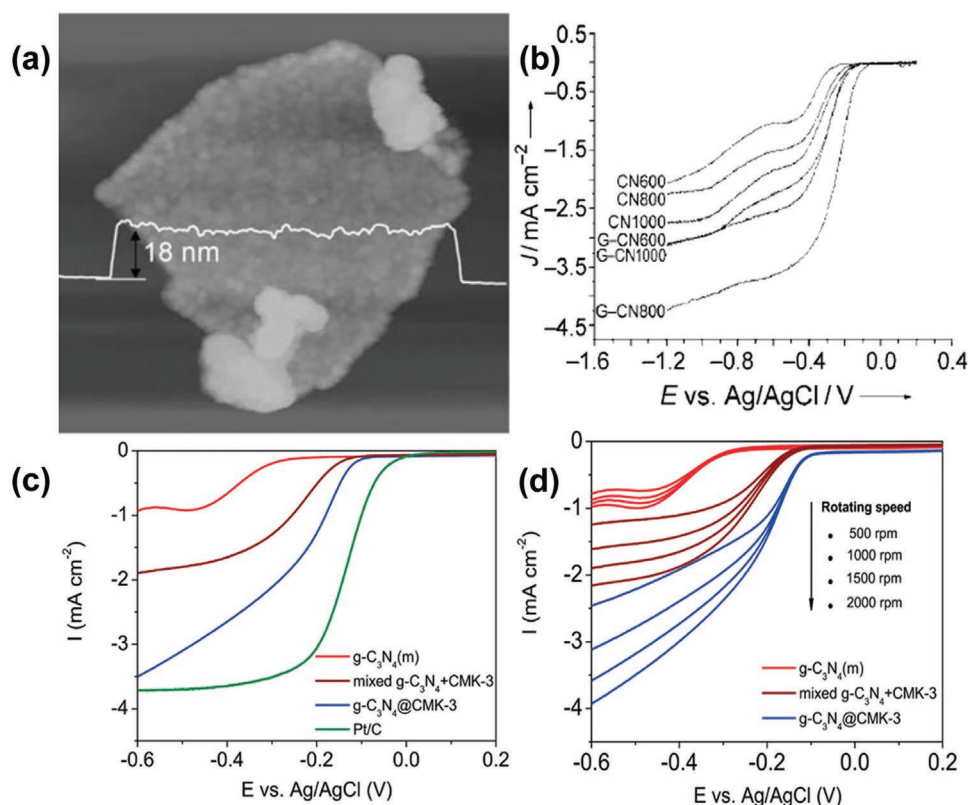


Figure 14. a) AFM image of graphene-based carbon nitride (G-CN) nanosheets. b) Polarization curves of G-CN and CN nanosheets at a rotation rate of 1600 rpm in O_2 -saturated 0.1 M KOH at a scan rate of 5 mV s^{-1} . Reproduced with permission.^[285] Copyright 2011, Wiley-VCH GmbH & Co. KGaA, Weinheim. c) Voltammograms of various electrocatalysts on rotating disk electrode at 1500 rpm at a scan rate of 5 mV s^{-1} and d) at different rotating rates (500 to 2000 rpm), recorded in O_2 -saturated 0.1 M KOH solution at a scan rate of 5 mV s^{-1} . Reproduced with permission.^[37] Copyright 2011, American Chemical Society.

properties, conjugation, unique triangular pores, and superior semiconducting properties.^[287,288] Particularly, N-doped GDY has been widely investigated for electrochemical applications, including ORR electrocatalysis.^[289] In 2018, Zhao et al. introduced sp-hybridized nitrogen (sp-N) atoms into the skeleton of 2D GDY by a pericyclic reaction route to facilitate O_2 adsorption as well as electron transfer.^[290] Corresponding TEM and polarization curves in the ORR potential region are displayed in **Figure 16a–c**. Upon optimization of the doping site and proportion of sp-N atoms, the sp-N-doped GDY delivered outstanding ORR catalytic activity comparable to Pt/C with an $E_{1/2}$ of 0.87 V in alkaline solution, as well as high stability and sufficient methanol resistance. In 2019, Lv et al. introduced accurately pyridinic N into the carbon skeleton of graphdiyne (PyN-GDY) using a cross-coupling reaction.^[291] The resulting PyN-GDY possessed a well-defined molecular structure, acting as a model for investigating the intrinsic activity of pyridinic active sites. It demonstrated excellent ORR activity with half-wave potential of 0.84 and 0.55 V (vs RHE) in alkaline and acidic media, respectively, and its activity and stability was demonstrated in Zn–air batteries.

The N-doped GDY materials can also be designed as metal-free OER electrocatalysts. Gu et al. investigated the electrocatalytic activity of GDY doped with B, N, P, and S toward the conversion of oxygen through theoretical calculation.^[292] They found that sp-N-doped graphdiyne, graphitic S-doped, and

graphitic P-doped graphdiyne demonstrated catalytic activities similar or better than those of Pt/C or RuO_2 . Additionally, the sp-N dopant can effectively generate ORR and OER active sites within the N-doped GDY structure, while graphitic S- and P-dopants can endow GDY with high ORR and OER activity, respectively. The authors also showed that positive charges were related to ORR activity while the OER catalytic properties were ascribed to spin densities. Another example of N-doped GDY bifunctional catalyst was recently reported by Lu et al. (Figure 16d–f).^[33] The N doping efficiently modulated electron distribution of GDY, facilitating electron/mass transfer and enhancing the catalytic activity. DFT calculations confirmed the lowering of the energy barrier by pyridinic N atoms, thus improving the reaction kinetics. Thereby, N-doped GDY-based zinc–air batteries showed a high open-circuit voltage of 1.54 V as well as high charge–discharge stability.

6.6. Metal–Nitrogen-Doped Carbon (M–N–C)-Based Electrocatalysts

Metal–nitrogen-doped carbon (M–N–C) materials are promising ORR/OER catalysts because the hybridization of metal and nitrogen-doped carbon precursors provide abundant catalytic centers and electron/mass transfer pathways.^[293] Various

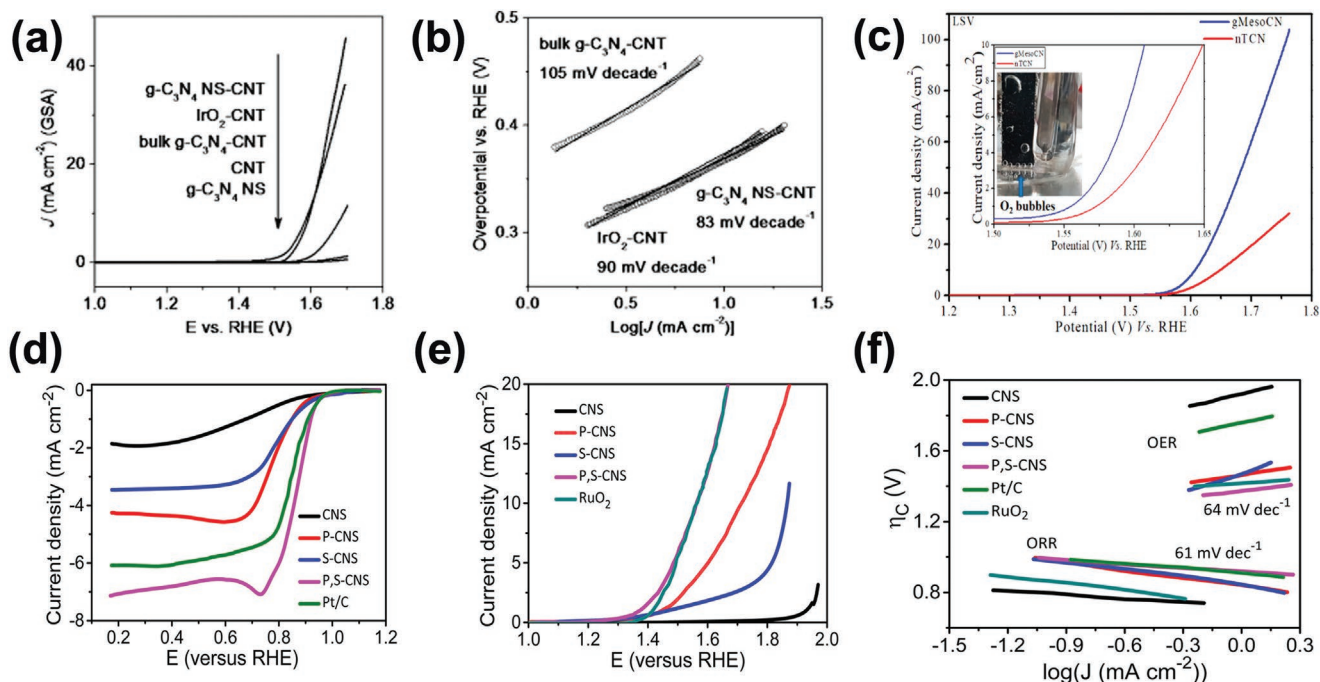


Figure 15. a) Linear sweep voltammograms and b) Tafel plots for different C_3N_4 on a rotating disk electrode (1500 rpm) recorded in O_2 -saturated 0.1 M KOH solution at a scan rate of 5 mV s^{-1} . Reproduced with permission.^[84] Copyright 2014, Wiley-VCH GmbH & Co. KGaA, Weinheim). c) Linear sweep voltammograms of mesoporous carbon nitride nanostructured electrocatalyst. The photograph in the inset shows the formation of O_2 bubbles. Reproduced with permission.^[284] Copyright 2020, American Chemical Society. d) Linear sweep voltammograms obtained with different catalysts in the ORR potential region recorded in O_2 -saturated 0.1 M KOH electrolyte at 1600 rpm electrode rotation at a scan rate of 5 mV s^{-1} , e) in the OER potential region recorded in 0.1 M KOH at 1600 rpm electrode rotation at a scan rate of 5 mV s^{-1} , and f) the corresponding Tafel plots displaying both the ORR and the OER potential regions. Reproduced with permission.^[88] Copyright 2016, American Physical Society.

M–N–C catalysts have been discovered by combining transition metal and N–C precursors, exhibiting promising catalytic properties to replace noble metal-based catalysts. The metal ions can influence the structure, morphology and catalytic properties of M–N–C catalysts as shown by Li et al. on M–N–C catalysts prepared by pyrolyzing metal-polydopamine (M-PDA) precursors.^[294] In particular, the Co–N–C moieties demonstrated a higher half-wave potential of 767 mV (vs RHE) and current densities during the ORR than commercial Pt/C and other M–N–C catalysts investigated. Besides, the OER activity and durability of the catalyst also stood out, rendering it a promising catalyst for bifunctional oxygen conversion. Recently, Zhang et al. integrated Ni(Fe)OOH with Ni/Fe–N–C to form 3D core–shell nanochains ($Ni_2Fe_1@PANI-KOH900$).^[295] The catalyst displayed outstanding catalytic performance by inheriting the properties of Ni(Fe)OOH for OER and Ni/Fe–N–C for ORR. Zn–air batteries composed of $Ni_2Fe_1@PANI-KOH900$ demonstrated high charging–discharging performance over 200 cycles.

The catalytic properties of the M–N–C can be improved by controlling the structure and morphology of the N–C component. The increase of the electrochemical surface area by hierarchical mesoporous structures lead to the development of Co, N-doped carbon material with outstanding bifunctional catalytic activities, displaying an $E_{1/2}$ of 855 mV (vs RHE) in 0.1 M KOH for the ORR, and an overpotential of 344 mV at $j = 10 \text{ mA cm}^{-2}$ for the OER in the same electrolyte.^[296] Additionally, the catalyst demonstrated excellent practical applications in Zn–air batteries, with a small discharge–charge

voltage gap (0.8 V at 2 mA cm^{-2}) and superior cycling stability. Zhang et al. synthesized a 3D hierarchical catalyst comprising Co nanoparticles and N-doped carbon nanocapsules on N-doped graphene.^[297] The catalyst exhibited a porous structure and high surface area, facilitating the mass transfer and exposure of catalytic centers. Moreover, the cobalt nanoparticles were wrapped by carbon layers, preventing erosion during the electrochemical process. The unique structure synergistically imparted the catalyst with outstanding performances toward the OER (overpotential = 298 mV at 10 mA cm^{-2}) and the ORR ($E_{1/2} = 0.86 \text{ V}$ vs RHE). Furthermore, the bifunctional catalyst showed a small potential gap of 0.67 V between $E_{1/2}$ and E_{10} , surpassing commercial noble RuO_2 (0.87 V). Derivating new catalysts from metal–organic frameworks also lead to active bifunctional catalysts. Cai et al. reported a 3D porous Co@N–C catalyst composed of abundant CoN_x and Co nanoparticles embedded in carbon networks, which facilitated the ORR and OER kinetics.^[298] Besides, the zinc–air batteries assembled with the catalyst exhibited a high power density (150 mW cm^{-2}), a high specific energy density ($964.2 \text{ W h kg}^{-1}$), and sufficient cycling stability (730 cycles with 10 mA cm^{-2} charge/discharge current density). N-doped hollow porous carbon nanofibers with incorporated Co nanoparticles were also reported by Lu et al. using electrospinning and ultrafast high-temperature shock technique (Figure 17a,b).^[299] The existence of Co–N–C species and the coupling of Co and N–C resulted in improved reaction energy barrier and kinetics, leading to excellent electrocatalytic activities for the OER (overpotential = 289 mV at 10 mA cm^{-2})

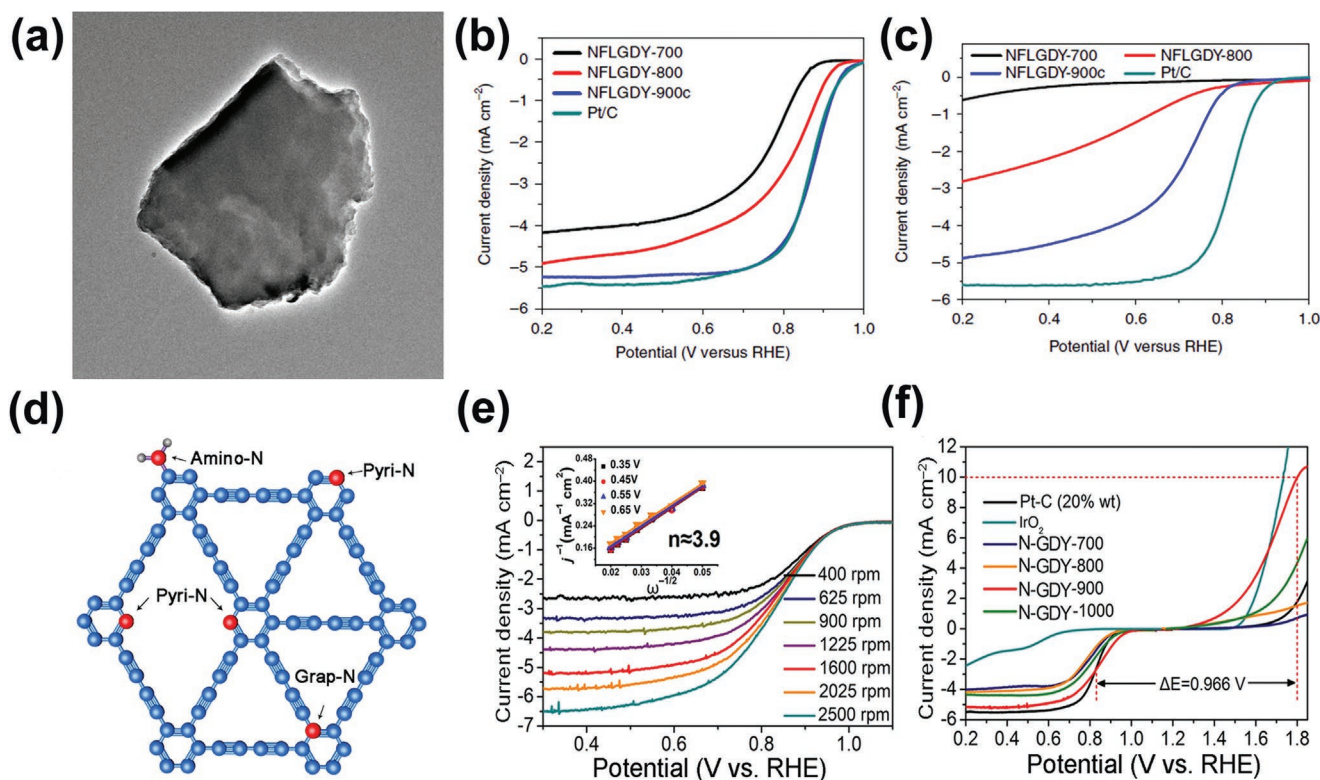


Figure 16. a) TEM image of pristine bulk graphdiyne with 2D morphology. ORR polarization curves of N-doped few-layer graphdiyne in b) alkaline and c) acidic solutions. Few-layer graphdiyne: FLGDY, bulk graphdiyne: BGDY. Reproduced with permission.^[290] Copyright 2018, Springer Nature. d) Schematic diagram of different N-doping forms in graphdiyne. e) Linear sweep voltammograms of N-GDY-900 with different electrode rotation speeds from 400 to 2500 rpm at 5 mV s^{-1} under O_2 -saturated 0.1 M KOH . Inset shows the corresponding Koutecky–Levich plot for the determination of the electron transfer number (n). f) ORR and OER voltammograms of four catalysts compared with commercial Pt/C and IrO_2 . (0.1 M KOH for ORR and 1 M KOH for OER). Reproduced with permission.^[33] Copyright 2021, Elsevier.

as well as for the ORR ($E_{1/2} = 0.85 \text{ V vs RHE}$). When employed as an air-electrode catalyst, the assembled zinc-air batteries demonstrated high specific capacity and cycling stability.

Constructing atomically dispersed dual metal sites in M–N–C is another strategy to improve the efficiency of carbon-based electrocatalysts. Zhu et al. reported hierarchically porous M–N–C ($M = \text{Fe}$ or Co) single-atom electrocatalysts using bimodal template-based synthesis strategies (Figure 17c–e).^[300] The catalysts with active and robust MN_2 active moieties demonstrated enhanced intrinsic activity of ORR and superior anti-poisoning power, as well as a high affinity for O_2 . Particularly, the optimized, high surface area Fe–N–C catalyst presents a half-wave potential of 0.927 V (vs RHE) in an alkaline medium for ORR, which is 49 and 55 mV higher than those of the Co–N–C counterpart and commercial Pt/C, respectively. The higher activity of the Fe-containing catalyst is ascribed to the presence of FeN_2 sites that lead to lower energy barriers for the formation of intermediates and products compared to CoN_2 sites.

Another interesting approach for the synthesis of metal-nitrogen-codoped carbons for bifunctional ORR/OER applications consists of the use of metal macrocyclic complexes, such as porphyrins or phthalocyanines, as precursors. Their impregnation with N-doped carbon and pyrolysis under an inert atmosphere, yielded MN_x moieties ($M = \text{Mn}$ or Co) embedded in an N-doped carbon matrix which served as active sites for

the ORR as reported by Masa et al.^[301] Upon subsequent mild calcination, OER-active N-coordinated metal oxide species were formed, thus creating active bifunctional ORR/OER catalysts. The synthesis route was later extended to incorporate N-doped few-layer graphene by firstly conducting liquid-phase exfoliation of graphite in the presence of a macrocyclic complex, yielding π -stacked graphene/complex composites that were later subjected to the aforementioned heat treatment.^[302] The metal content in the resulting materials was less than 0.2 wt% but nevertheless demonstrated high activity for both the ORR and the OER (E_1 of 0.88 V and E_{10} of 1.88 V vs RHE), with performance depending largely on the metal complex used as precursor. In particular, Ni-tetrasulfonated phthalocyanine appeared as the most promising precursor for the fabrication of low metal loading N-doped graphene hybrids, resulting in a NiO_x/N -graphene composite with an ORR/OER overpotential gap of 0.87 V .

6.7. Comparison of N-Doped Carbon-Based Electrocatalysts

An overview of the ORR/OER performance of N-doped carbon-based electrocatalysts reviewed in this section are summarized in Table 5. GDY and graphene-based materials appear best for ORR. In general, there is a consensus toward the improvement of ORR activity for pyridinic nitrogen, although the local

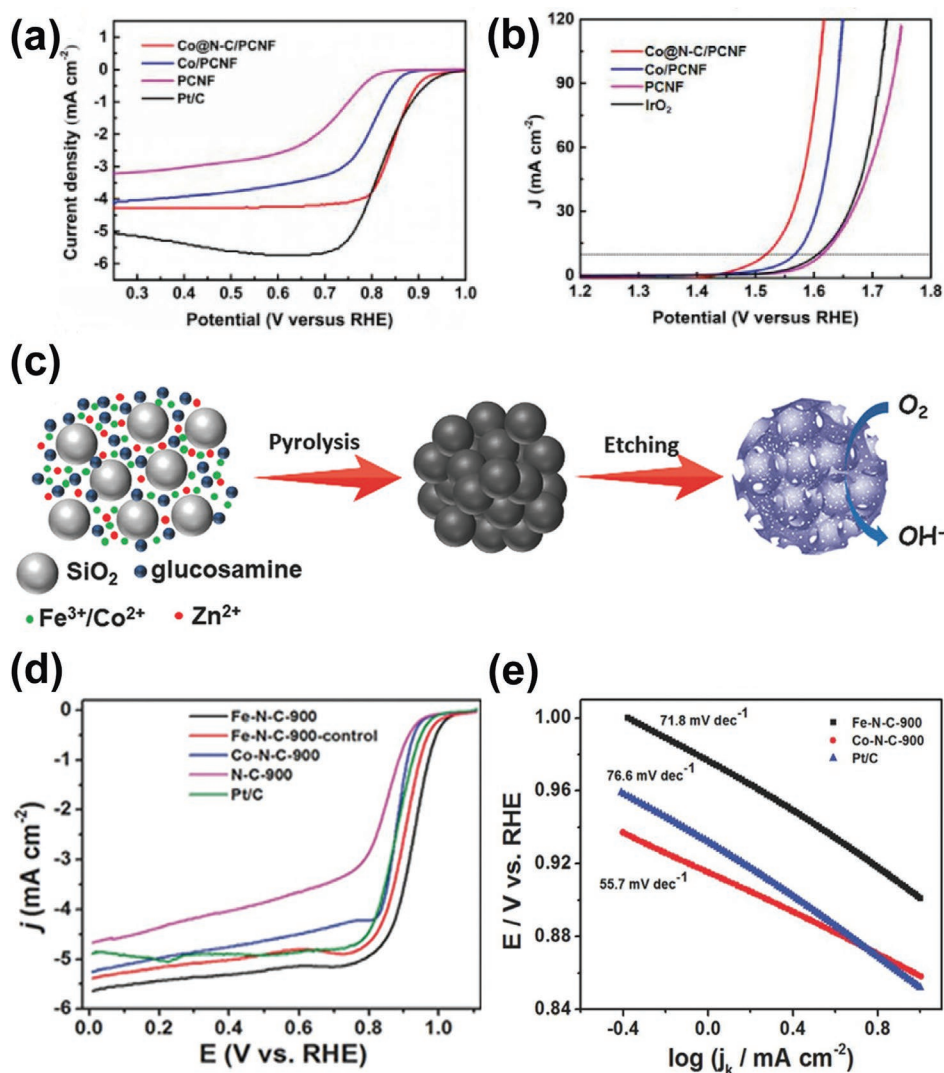


Figure 17. a) ORR and b) OER linear sweep voltammograms of Co@N-C/PCNF, Co/PCNF, PCNF, and Pt/C recorded at 5 mV s^{-1} with a rotation speed of 1600 rpm. Reproduced with permission.^[299] Copyright 2021, Wiley-VCH GmbH & Co. KGaA, Weinheim. c) A schematic illustration of the synthesis of hierarchically porous M–N–C ($M = \text{Co}$ and Fe) single-atom electrocatalysts. d) ORR voltammograms of Fe(Co)–N–C, N–C, and commercial Pt/C recorded at 10 mV s^{-1} and a rotating speed of 1600 rpm. e) Tafel plots of Fe–N–C-900, Co–N–C-900, and Pt/C. Reproduced with permission.^[300] Copyright 2018, Wiley-VCH GmbH & Co. KGaA, Weinheim.

chemical environment of these groups can also affect its activity. The increase of the surface area improves the accessibility to active sites while improvement of electrical conductivity by coupling with pure carbon-based materials such as graphene and CNTs is often beneficial. While high area metal-free electrocatalysts have shown reasonable OER activity, the addition of a small amount of metal-N-doped carbons obviously improves significantly the electrochemical activity. These results constitute promising perspectives for the development of N-doped carbon-based oxygen electrocatalysts.

7. Conclusion and Perspectives

N-doping has been demonstrated as an efficient approach for tuning the electron structures of carbon materials toward higher electrocatalytic performances. In this review, N-doped

carbon electrocatalysts for the OER and ORR reactions were presented and we underlined the proposed mechanisms for these two reactions on this type of material. Different synthesis methods and applications as ORR and OER catalysts, as well as characterization techniques, were concisely presented. Although great progress has been made over the past few years in developing N-doped carbon-based catalysts to replace precious metal catalysts for the ORR and OER in energy conversion and storage applications, several key challenges remain. They are summarized below:

1. The activity of nitrogen dopants toward oxygen electrocatalysis depends strongly on the nitrogen chemical structure, doping site, and concentration. Despite clear progress in recent years, the undisputed nature of the catalytic mechanism of N-types active sites has not yet been determined. This point

Table 5. Summary of ORR and OER performance of N-doped carbon-based catalysts. $E_{1/2}$ vs RHE (V) and E_{10} vs RHE (V) represent half-wave potential and potential at a current density of 10 mA cm^{-2} , respectively. Meanwhile, the Tafel slope (mV dec^{-1}) is from Tafel equation $\eta = b \cdot \log(j/j_0)$ ($b = \ln(10) RT/\alpha nF$), where b is the so-called Tafel slope, given typically in mV dec^{-1} units, R is the ideal gas constant, T is the absolute temperature, n is the number of electrons transferred during the redox reaction, F is the Faraday constant, and α is the charge transfer coefficient. Tafel slope (of the OER) relates the overpotential (η) to the logarithmic current density ($\log j$).

Catalyst	Type of carbon	Synthesis route	Electrolyte	$E_{1/2}$ vs RHE [V]	E_{10} vs RHE [V]	Tafel slope [mV dec^{-1}]	Refs.
ORR	N-doped carbon dots/CNT hybrid	Wet chemical method	0.1 M KOH	0.780	–	60.9	[275]
	Nanoporous N-doped carbon microfiber	Biomass conversion	0.1 M KOH	0.780	–	–	[303]
	N-doped graphene gel-like hybrid	Hydrothermal method	0.1 M KOH	0.859	–	–	[36]
	N-doped graphene	Hydrothermal method	0.1 M KOH	0.862	–	–	[304]
	Few-layer N-doped graphdiyne	Pericyclic organic reaction	0.1 M KOH	0.870	–	60.0	[290]
OER	3D N-doped carbon film	Assembly	0.1 M KOH	–	1.38	128.0	[305]
	3D porous N-doped carbon microtube sponge	Pyrolysis	0.1 M KOH	–	1.52	246	[167]
	3D self-supporting N-doped monolithic porous carbon cloth	Thermal reduction	1 M KOH	–	1.59	98.0	[306]
	g-C ₃ N ₄ and CNTs	Self-assembly	0.1 M KOH	–	1.6	83.0	[84]
	N-doped graphene/CNTs hybrid	CVD	0.1 M KOH	–	1.63	83.0	[176]
	N-doped carbon sheets	Pyrolysis of chitin	0.1 M KOH	–	1.64	116.0	[307]
	g-C ₃ N ₄ /graphene	Ultrasonication	0.1 M KOH	–	1.84	68.5	[308]
OER and ORR	Co, N-doped hollow carbon nanofibers	Electrospinning	0.1 M KOH	0.850	1.25	91.8 (OER)	[299]
	Co, N-doped carbon materials	Pyrolysis	0.1 M KOH	0.855	1.31	52.5 (ORR) and 57.8 (OER)	[296]
	Co, N-doped carbon nanocapsules on 3D carbon frameworks	Hydrothermal method	0.1 M KOH	0.860	1.53	66.6 (ORR) and 114.4 (OER)	[297]
	N-doped oxidized MWCNTs	CVD	0.1 M KOH	0.820	1.67	–	[107]

should be clarified in future research, based on real-time operando characterization and ideally supported by theoretical methods. Particularly, change of valence state, coordination number, chemical configuration, and evolution of elemental composition, with respect to time and/or applied potentials should be monitored. Based on operando characterization, a series of critical issues, such as surface remodeling and substrate–surface interaction during electrocatalysis are expected to be resolved and thus the accurate identification of OER and ORR reactive sites may be achieved.

- Most N-doped carbon materials exhibit enhanced stability against poisoning by CO or methanol than Pt/C.^[309] However, these materials generally exhibit lower catalytic activity toward the ORR in acidic media compared to Pt/C based on the half-wave potential. Up to now, two hypotheses have been suggested: (electro)chemical instability and susceptibility to protonation.^[16] The proposed strategies to counteract this drawback are 1) trying to obtain a higher degree of graphitization, and 2) incorporating a higher number of graphitic N atoms, which are not prone to protonation.
- The role of nonprecious metal impurities, particularly of iron, remains to be clearly distinguished from the intrinsic activity of a wide variety of N-doped materials.^[310] The presence of small amounts of nonprecious metals in N-doped carbon electrocatalyst could be favorable for its activity under acidic conditions for ORR.^[311] Similarly for alkaline media, the presence of iron impurities in precursors, such as

graphite, may lead to an overall enhancement of the ORR and OER activity.^[312] While this aspect can be further studied and rationalized for the strategic incorporation of non-precious metal dopants into N-doped carbon materials, in the field of metal-free catalysts, rigorous tests of absence of metals after synthesis and after electrochemical measurements are required to fully demonstrate the origin of their catalytic properties. Particularly, conducting purification of electrolytes prior to electrochemical measurements is crucial for fundamental research to prevent incorporation of metal impurities in the catalyst films.

- The synthesis routes and experimental conditions for the preparation of the N-doped carbon materials have an important impact on the final nitrogen content, nitrogen configuration, surface area, degree of graphitization, morphology, and textural characteristics of the resulting materials.^[16] For instance, the distribution of N-active sites is rather difficult to control for pyrolysis-derived N-doped carbons. Meanwhile, biomass-derived carbons generally have low or even lack a nitrogen source, hence a second N-source may be required, resulting in a poor homogeneity of the final materials.^[43] As for plasma treatment for N-doped carbons, the nitrogen content in the carbon materials can only be achieved upon thorough optimization of the exposure time and plasma strength.^[43,186] Thereby, the choice of suitable synthesis methods should be carefully considered for the fabrication of N-doped carbons to obtain optimal electrocatalytic performance.

5. The degradation mechanism of carbon-based catalysts and the evolution process of the N-type active sites in nanocarbon materials need to be properly investigated.^[27] Particularly, carbon corrosion can be considered among the most important degradation mechanisms, especially in highly oxidative conditions,^[313] with a strong impact on the performance of the catalysts, leading to a possible decrease in electrical conductivity, collapse of the electrode pore structure, loss of hydrophobic character, and increase of the catalyst particle size.^[314]
6. Typical electrochemical methods used for the evaluation of the catalytic activity do not provide information on reactions competing with the conversion of oxygen. Particularly for N-doped carbon-based materials, competition between O₂ and CO₂ evolution during electrocatalytic measurements cannot be distinguished by voltammetric methods, rendering the use of coupled oxygen-detection techniques, such as differential electrochemical mass spectrometry and rotating ring disk electrode voltammetry, crucial for an accurate determination of the Faradaic efficiency.^[19] Moreover, reporting intrinsic activities, e.g., normalized by catalyst mass, electroactive surface area or the number of active sites, rather than geometric area-normalized current will be crucial to identifying an optimal catalyst composition (including defects) for oxygen electrocatalysis.

Despite the aforementioned challenges, the large-scale application of N-doped carbon catalysts unquestionably has a promising future thanks to the continuous research directed toward the development of these materials, preferably metal-free materials, for oxygen electrocatalytic energy conversion and storage applications.

Acknowledgements

B.W., H.M., and D.M.M. contributed equally to this work. This work was supported by the Volkswagen Foundation (Freigeist Fellowship No. 89592). B.W. also acknowledges the funding by the CSC Fellowship. Open access funding enabled and organized by Projekt DEAL.

Conflict of Interest

The authors declare no conflict of interest.

Keywords

carbon nanomaterials, electrocatalysis, nitrogen doping, oxygen evolution reaction, oxygen reduction reaction

Received: April 13, 2022

Revised: May 10, 2022

Published online: May 31, 2022

- [1] M. Tahir, L. Pan, F. Idrees, X. Zhang, L. Wang, J.-J. Zou, Z. L. Wang, *Nano Energy* **2017**, *37*, 136.
 [2] J. Wang, Y. Li, X. Sun, *Nano Energy* **2013**, *2*, 443.
 [3] X. Tian, X. F. Lu, B. Y. Xia, X. W. (David) Lou, *Joule* **2020**, *4*, 45.
 [4] Z.-L. Wang, D. Xu, J.-J. Xu, X.-B. Zhang, *Chem. Soc. Rev.* **2014**, *43*, 7746.

- [5] J.-S. Lee, S. Tai Kim, R. Cao, N.-S. Choi, M. Liu, K. T. Lee, J. Cho, *Adv. Energy Mater.* **2011**, *1*, 34.
 [6] H. Zhao, Y. Lei, *Adv. Energy Mater.* **2020**, *10*, 2001460.
 [7] T. M. Gür, *Energy Environ. Sci.* **2018**, *11*, 2696.
 [8] J. Shui, M. Wang, F. Du, L. Dai, *Sci. Adv.* **2015**, *1*, 1400129.
 [9] H. Yang, X. Han, A. I. Douka, L. Huang, L. Gong, C. Xia, H. S. Park, B. Y. Xia, *Adv. Funct. Mater.* **2021**, *31*, 2007602.
 [10] X. Ren, T. Wu, Y. Sun, Y. Li, G. Xian, X. Liu, C. Shen, J. Gracia, H.-J. Gao, H. Yang, Z. J. Xu, *Nat. Commun.* **2021**, *12*, 2608.
 [11] G. Chen, Y. Sun, R. R. Chen, C. Biz, A. C. Fisher, M. P. Sherburne, J. W. Ager III, J. Gracia, Z. J. Xu, *J. Phys.: Energy* **2021**, *3*, 031004.
 [12] Z.-F. Huang, J. Song, Y. Du, S. Xi, S. Dou, J. M. V. Nsanzimana, C. Wang, Z. J. Xu, X. Wang, *Nat. Energy* **2019**, *4*, 329.
 [13] P. P. Patel, M. K. Datta, O. I. Velikokhatnyi, R. Kuruba, K. Damodaran, P. Jampani, B. Gattu, P. M. Shanthi, S. S. Dample, P. N. Kumta, *Sci. Rep.* **2016**, *6*, 28367.
 [14] K. B. Ibrahim, M.-C. Tsai, S. A. Chala, M. K. Berihun, A. W. Kahsay, T. A. Berhe, W.-N. Su, B.-J. Hwang, *J. Chin. Chem. Soc.* **2019**, *66*, 829.
 [15] Q. Shi, C. Zhu, D. Du, Y. Lin, *Chem. Soc. Rev.* **2019**, *48*, 3181.
 [16] N. Daems, X. Sheng, I. F. J. Vankelecom, P. P. Pescarmona, *J. Mater. Chem. A* **2014**, *2*, 4085.
 [17] X. Liu, L. Dai, *Nat. Rev. Mater.* **2016**, *1*, 16064.
 [18] L. Dai, *Curr. Opin. Electrochem.* **2017**, *4*, 18.
 [19] S. Möller, S. Barwe, J. Masa, D. Wintrich, S. Seisel, H. Baltruschat, W. Schuhmann, *Angew. Chem., Int. Ed.* **2020**, *59*, 1585.
 [20] Y. Jia, K. Jiang, H. Wang, X. Yao, *Chem* **2019**, *5*, 1371.
 [21] Y. Ding, W. Zhou, J. Gao, F. Sun, G. Zhao, *Adv. Mater. Interfaces* **2021**, *8*, 2002091.
 [22] S. K. Singh, K. Takeyasu, J. Nakamura, *Adv. Mater.* **2019**, *31*, 1804297.
 [23] C. Hu, L. Dai, *Angew. Chem., Int. Ed.* **2016**, *55*, 11736.
 [24] G. Murdachaew, K. Laasonen, *J. Phys. Chem. C* **2018**, *122*, 25882.
 [25] Gong Kuanping, Du Feng, Xia Zhenhai, Durstock Michael, Dai Liming, *Science* **2009**, *323*, 760.
 [26] I. Masood ul Hasan, L. Peng, J. Mao, R. He, Y. Wang, J. Fu, N. Xu, J. Qiao, *Carbon Energy* **2021**, *3*, 24.
 [27] C. Tang, Q. Zhang, *Adv. Mater.* **2017**, *29*, 1604103.
 [28] J. Zhang, Z. Xia, L. Dai, *Sci. Adv.* **2015**, *1*, 1500564.
 [29] L. Qin, R. Ding, H. Wang, J. Wu, C. Wang, C. Zhang, Y. Xu, L. Wang, B. Lv, *Nano Res.* **2017**, *10*, 305.
 [30] L. Qu, Y. Liu, J.-B. Baek, L. Dai, *ACS Nano* **2010**, *4*, 1321.
 [31] H. B. Yang, J. Miao, S.-F. Hung, J. Chen, H. B. Tao, X. Wang, L. Zhang, R. Chen, J. Gao, H. M. Chen, L. Dai, B. Liu, *Sci. Adv.* **2016**, *2*, 1501122.
 [32] G. Mohamad, S. Sarkar, A. Biswas, K. Roy, R. S. Dey, *Chem. - Eur. J.* **2020**, *26*, 12664.
 [33] T. Lu, X. Hu, J. He, R. Li, J. Gao, Q. Lv, Z. Yang, S. Cui, C. Huang, *Nano Energy* **2021**, *85*, 106024.
 [34] G. Lemes, D. Sebastián, E. Pastor, M. J. Lázaro, *J. Power Sources* **2019**, *438*, 227036.
 [35] W. Wei, H. Liang, K. Parvez, X. Zhuang, X. Feng, K. Müllen, *Angew. Chem., Int. Ed.* **2014**, *53*, 1570.
 [36] Q. Xiang, Y. Liu, X. Zou, B. Hu, Y. Qiang, D. Yu, W. Yin, C. Chen, *ACS Appl. Mater. Interfaces* **2018**, *10*, 10842.
 [37] Y. Zheng, Y. Jiao, J. Chen, J. Liu, J. Liang, A. Du, W. Zhang, Z. Zhu, S. C. Smith, M. Jaroniec, G. Q. (Max) Lu, S. Z. Qiao, *J. Am. Chem. Soc.* **2011**, *133*, 20116.
 [38] S. S. Shinde, C.-H. Lee, A. Sami, D.-H. Kim, S.-U. Lee, J.-H. Lee, *ACS Nano* **2017**, *11*, 347.
 [39] C. Hu, C. Yu, M. Li, X. Wang, Q. Dong, G. Wang, J. Qiu, *Chem. Commun.* **2015**, *51*, 3419.
 [40] Q. Li, S. Zhang, L. Dai, L. Li, *J. Am. Chem. Soc.* **2012**, *134*, 18932.
 [41] W. A. Saidi, *J. Phys. Chem. Lett.* **2013**, *4*, 4160.

- [42] X. Ge, A. Sumboja, D. Wu, T. An, B. Li, F. W. T. Goh, T. S. A. Hor, Y. Zong, Z. Liu, *ACS Catal.* **2015**, *5*, 4643.
- [43] J. Wang, H. Kong, J. Zhang, Y. Hao, Z. Shao, F. Ciucci, *Prog. Mater. Sci.* **2021**, *116*, 100717.
- [44] Q. Zhao, Z. Yan, C. Chen, J. Chen, *Chem. Rev.* **2017**, *117*, 10121.
- [45] K.-H. Wu, D.-W. Wang, D.-S. Su, I. R. Gentle, *ChemSusChem* **2015**, *8*, 2772.
- [46] X. Wang, Z. Li, Y. Qu, T. Yuan, W. Wang, Y. Wu, Y. Li, *Chem* **2019**, *5*, 1486.
- [47] M. Risch, *Catalysts* **2017**, *7*, 154.
- [48] M. Shao, *Electrocatalysis in Fuel Cells: A Non- and Low- Platinum Approach*, Springer, London **2013**.
- [49] Y. Li, Q. Li, H. Wang, L. Zhang, D. P. Wilkinson, J. Zhang, *Electrochem. Energy Rev.* **2019**, *2*, 518.
- [50] F. Cheng, J. Chen, *Chem. Soc. Rev.* **2012**, *41*, 2172.
- [51] H. Singh, S. Zhuang, B. Ingis, B. B. Nunna, E. S. Lee, *Carbon* **2019**, *151*, 160.
- [52] K. Zeng, X. Zheng, C. Li, J. Yan, J.-H. Tian, C. Jin, P. Strasser, R. Yang, *Adv. Funct. Mater.* **2020**, *30*, 2000503.
- [53] T. Zhao, Y. Wang, S. Karuturi, K. Catchpole, Q. Zhang, C. Zhao, *Carbon Energy* **2020**, *2*, 582.
- [54] S. Li, X. Hao, A. Abudula, G. Guan, *J. Mater. Chem. A* **2019**, *7*, 18674.
- [55] Y. Wang, D. Wang, Y. Li, *Smart Mat.* **2021**, *2*, 56.
- [56] Z.-F. Huang, J. Song, S. Dou, X. Li, J. Wang, X. Wang, *Matter* **2019**, *1*, 1494.
- [57] Z.-C. Yao, T. Tang, J.-S. Hu, L.-J. Wan, *Energy Fuels* **2021**, *35*, 6380.
- [58] M. Liu, L. Wang, K. Zhao, S. Shi, Q. Shao, L. Zhang, X. Sun, Y. Zhao, J. Zhang, *Energy Environ. Sci.* **2019**, *12*, 2890.
- [59] X.-M. Liu, X. Cui, K. Dastafkan, H.-F. Wang, C. Tang, C. Zhao, A. Chen, C. He, M. Han, Q. Zhang, *J. Energy Chem.* **2021**, *53*, 290.
- [60] M. Yin, H. Miao, R. Hu, Z. Sun, H. Li, *J. Power Sources* **2021**, *494*, 229779.
- [61] R. Ma, G. Lin, Y. Zhou, Q. Liu, T. Zhang, G. Shan, M. Yang, *J. Wang, npj Comput. Mater.* **2019**, *5*, 78.
- [62] Q. Lv, W. Si, J. He, L. Sun, C. Zhang, N. Wang, Z. Yang, X. Li, X. Wang, W. Deng, Y. Long, C. Huang, Y. Li, *Nat. Commun.* **2018**, *9*, 3376.
- [63] J. A. Behan, E. Mates-Torres, S. N. Stamatina, C. Domínguez, A. Iannaci, K. Fleischer, Md. K. Hoque, T. S. Perova, M. García-Melchor, P. E. Colavita, *Small* **2019**, *15*, 1902081.
- [64] H. Jiang, J. Gu, X. Zheng, M. Liu, X. Qiu, L. Wang, W. Li, Z. Chen, X. Ji, J. Li, *Energy Environ. Sci.* **2019**, *12*, 322.
- [65] T. Reier, H. N. Nong, D. Teschner, R. Schlögl, P. Strasser, *Adv. Energy Mater.* **2017**, *7*, 1601275.
- [66] J. Song, C. Wei, Z.-F. Huang, C. Liu, L. Zeng, X. Wang, Z. J. Xu, *Chem. Soc. Rev.* **2020**, *49*, 2196.
- [67] X. Ren, C. Wei, Y. Sun, X. Liu, F. Meng, X. Meng, S. Sun, S. Xi, Y. Du, Z. Bi, G. Shang, A. C. Fisher, L. Gu, Z. J. Xu, *Adv. Mater.* **2020**, *32*, 2001292.
- [68] L. An, C. Wei, M. Lu, H. Liu, Y. Chen, G. G. Scherer, A. C. Fisher, P. Xi, Z. J. Xu, C.-H. Yan, *Adv. Mater.* **2021**, *33*, 2006328.
- [69] Z.-Y. Yu, Y. Duan, X.-Y. Feng, X. Yu, M.-R. Gao, S.-H. Yu, *Adv. Mater.* **2021**, *33*, 2007100.
- [70] H. Dau, C. Limberg, T. Reier, M. Risch, S. Roggan, P. Strasser, *ChemCatChem* **2010**, *2*, 724.
- [71] Y. Zhou, S. Sun, C. Wei, Y. Sun, P. Xi, Z. Feng, Z. J. Xu, *Adv. Mater.* **2019**, *31*, 1902509.
- [72] N.-T. Suen, S.-F. Hung, Q. Quan, N. Zhang, Y.-J. Xu, H. M. Chen, *Chem. Soc. Rev.* **2017**, *46*, 337.
- [73] H. J. Song, H. Yoon, B. Ju, D.-W. Kim, *Adv. Energy Mater.* **2021**, *11*, 2002428.
- [74] D. Antipin, M. Risch, *J. Phys.: Energy* **2020**, *2*, 032003.
- [75] B. E. Conway, J. O. Bockris, A. K. Vijh, *J. Electrochem. Soc.* **1973**, *120*, 148C.
- [76] A. G. C. Kobussen, G. H. J. Broers, *J. Electroanal. Chem. Interfacial Electrochem.* **1981**, *126*, 221.
- [77] F.-Y. Chen, Z.-Y. Wu, Z. Adler, H. Wang, *Joule* **2021**, *5*, 1704.
- [78] F. Calle-Vallejo, M. T. M. Koper, *Electrochim. Acta* **2012**, *84*, 3.
- [79] J. Huang, X. Zhu, M. Eikerling, *Electrochim. Acta* **2021**, *393*, 139019.
- [80] L. Partanen, G. Murdachaew, K. Laasonen, *J. Phys. Chem. C* **2018**, *122*, 12892.
- [81] M. Li, L. Zhang, Q. Xu, J. Niu, Z. Xia, *J. Catal.* **2014**, *314*, 66.
- [82] X.-Z. Fan, Q.-Q. Pang, S.-S. Yi, X. Du, S. Zhang, Z.-Y. Liu, X.-Z. Yue, *Appl. Catal., B* **2021**, *292*, 120152.
- [83] Y. Zhao, R. Nakamura, K. Kamiya, S. Nakanishi, K. Hashimoto, *Nat. Commun.* **2013**, *4*, 2390.
- [84] T. Y. Ma, S. Dai, M. Jaroniec, S. Z. Qiao, *Angew. Chem., Int. Ed.* **2014**, *53*, 7281.
- [85] M. Zhao, T. Li, L. Jia, H. Li, W. Yuan, C. M. Li, *ChemSusChem* **2019**, *12*, 5041.
- [86] J. Duan, S. Chen, M. Jaroniec, S. Z. Qiao, *ACS Catal.* **2015**, *5*, 5207.
- [87] B. M. Matsagar, R.-X. Yang, S. Dutta, Y. S. Ok, K. C.-W. Wu, *J. Mater. Chem. A* **2021**, *9*, 3703.
- [88] J. Zhang, G. Zhang, S. Jin, Y. Zhou, Q. Ji, H. Lan, H. Liu, J. Qu, *Carbon* **2020**, *163*, 154.
- [89] N. Wang, B. Lu, L. Li, W. Niu, Z. Tang, X. Kang, S. Chen, *ACS Catal.* **2018**, *8*, 6827.
- [90] D. Guo, R. Shibuya, C. Akiba, S. Saji, T. Kondo, J. Nakamura, *Science* **2016**, *351*, 361.
- [91] T. Kondo, S. Casolo, T. Suzuki, T. Shikano, M. Sakurai, Y. Harada, M. Saito, M. Oshima, M. I. Trioni, G. F. Tantardini, J. Nakamura, *Phys. Rev. B* **2012**, *86*, 035436.
- [92] A. Ferre-Vilaplana, E. Herrero, *Sustainable Energy Fuels* **2019**, *3*, 2391.
- [93] Y. Bai, Y. Zheng, Z. Wang, Q. Hong, S. Liu, Y. Shen, Y. Zhang, *New J. Chem.* **2021**, *45*, 11876.
- [94] R. M. Lawrence, S. M. Unni, *Sustainable Energy Fuels* **2021**, *5*, 3765.
- [95] Y. Shao, Z. Jiang, Q. Zhang, J. Guan, *ChemSusChem* **2019**, *12*, 2133.
- [96] E. B. Yutomo, F. A. Noor, T. Winata, *RSC Adv.* **2021**, *11*, 18371.
- [97] G. P. Mane, S. N. Talapaneni, C. Anand, S. Varghese, H. Iwai, Q. Ji, K. Ariga, T. Mori, A. Vinu, *Adv. Funct. Mater.* **2012**, *22*, 3596.
- [98] J. Quílez-Bermejo, E. Morallón, D. Cazorla-Amorós, *Carbon* **2020**, *165*, 434.
- [99] Z. Lin, G. H. Waller, Y. Liu, M. Liu, C. Wong, *Nano Energy* **2013**, *2*, 241.
- [100] L. Li, C. Tang, Y. Zheng, B. Xia, X. Zhou, H. Xu, S.-Z. Qiao, *Adv. Energy Mater.* **2020**, *10*, 2000789.
- [101] M. Li, Z. Liu, F. Wang, J. Xuan, *J. Energy Chem.* **2017**, *26*, 422.
- [102] L. Feng, X. Chen, Y. Cao, Y. Chen, F. Wang, Y. Chen, Y. Liu, *RSC Adv.* **2017**, *7*, 14669.
- [103] L. Zhang, Z. Xia, *J. Phys. Chem. C* **2011**, *115*, 11170.
- [104] T. Ikeda, M. Boero, S.-F. Huang, K. Terakura, M. Oshima, J. Ozaki, *J. Phys. Chem. C* **2008**, *112*, 14706.
- [105] J. Quílez-Bermejo, M. Melle-Franco, E. San-Fabián, E. Morallón, D. Cazorla-Amorós, *J. Mater. Chem. A* **2019**, *7*, 24239.
- [106] J. Liu, P. Song, W. Xu, *Carbon* **2017**, *115*, 763.
- [107] M. A. Kazakova, A. Koul, G. V. Golubtsov, A. G. Selyutin, A. V. Ishchenko, R. I. Kvon, B. A. Kolesov, W. Schuhmann, D. M. Morales, *ChemElectroChem* **2021**, *8*, 2803.
- [108] X. Ning, Y. Li, J. Ming, Q. Wang, H. Wang, Y. Cao, F. Peng, Y. Yang, H. Yu, *Chem. Sci.* **2019**, *10*, 1589.
- [109] I. M. Rocha, O. S. G. P. Soares, D. M. Fernandes, C. Freire, J. L. Figueiredo, M. F. R. Pereira, *ChemistrySelect* **2016**, *1*, 2522.
- [110] N. Zhou, N. Wang, Z. Wu, L. Li, *Catalysts* **2018**, *8*, 509.
- [111] Y. Xu, L. Zhu, X. Cui, M. Zhao, Y. Li, L. Chen, W. Jiang, T. Jiang, S. Yang, Y. Wang, *Nano Res.* **2020**, *13*, 752.
- [112] U. I. Kramm, M. Lefèvre, N. Larouche, D. Schmeisser, J.-P. Dodelet, *J. Am. Chem. Soc.* **2014**, *136*, 978.
- [113] J. Zhu, S. Mu, *Adv. Funct. Mater.* **2020**, *30*, 2001097.

- [114] W. Tian, W. Li, W. Yu, X. Liu, *Micromachines* **2017**, *8*, 163.
- [115] J. Zhang, J. Zhang, F. He, Y. Chen, J. Zhu, D. Wang, S. Mu, H. Y. Yang, *Nano-Micro Lett.* **2021**, *13*, 65.
- [116] F. Banhart, J. Kotakoski, A. V. Krasheninnikov, *ACS Nano* **2011**, *5*, 26.
- [117] W. J. Lee, J. Lim, S. O. Kim, *Small Methods* **2017**, *1*, 1600014.
- [118] Y.-C. Lin, P.-Y. Teng, C.-H. Yeh, M. Koshino, P.-W. Chiu, K. Suenaga, *Nano Lett.* **2015**, *15*, 7408.
- [119] H. S. Kim, H. S. Kim, S. S. Kim, Y.-H. Kim, *Nanoscale* **2014**, *6*, 14911.
- [120] D. H. Lee, W. J. Lee, W. J. Lee, S. O. Kim, Y.-H. Kim, *Phys. Rev. Lett.* **2011**, *106*, 175502.
- [121] J. Wei, H. Hu, H. Zeng, Z. Wang, L. Wang, P. Peng, *Appl. Phys. Lett.* **2007**, *91*, 092121.
- [122] G. Wu, K. L. More, C. M. Johnston, P. Zelenay, *Science* **2011**, *332*, 443.
- [123] H. Tang, Y. Zeng, Y. Zeng, R. Wang, S. Cai, C. Liao, H. Cai, X. Lu, P. Tsiakaras, *Appl. Catal., B* **2017**, *202*, 550.
- [124] E. J. Biddinger, U. S. Ozkan, *J. Phys. Chem. C* **2010**, *114*, 15306.
- [125] P. Stumm, D. A. Drabold, P. A. Fedders, *J. Appl. Phys.* **1997**, *81*, 1289.
- [126] D. Li, Y. Jia, G. Chang, J. Chen, H. Liu, J. Wang, Y. Hu, Y. Xia, D. Yang, X. Yao, *Chem* **2018**, *4*, 2345.
- [127] J. W. D. Ng, M. Tang, T. F. Jaramillo, *Energy Environ. Sci.* **2014**, *7*, 2017.
- [128] J. J. Martin, V. Neburchilov, H. Wang, W. Qu, *2009 IEEE Electrical Power & Energy Conference (EPEC)*, IEEE, Piscataway, NJ **2009**, p. 759.
- [129] S. T. Senthilkumar, W. Go, J. Han, L. Pham Thi Thuy, K. Kishor, Y. Kim, Y. Kim, *J. Mater. Chem. A* **2019**, *7*, 22803.
- [130] J. W. Desmond Ng, Y. Gorlin, T. Hatsukade, T. F. Jaramillo, *Adv. Energy Mater.* **2013**, *3*, 1545.
- [131] S. Zhao, L. Yan, H. Luo, W. Mustain, H. Xu, *Nano Energy* **2018**, *47*, 172.
- [132] M. Klingenhof, P. Hauke, S. Brückner, S. Dresp, E. Wolf, H. N. Nong, C. Spöri, T. Merzdorf, D. Bernsmeier, D. Teschner, R. Schlögl, P. Strasser, *ACS Energy Lett.* **2021**, *6*, 177.
- [133] Z. Zhao, M. Li, L. Zhang, L. Dai, Z. Xia, *Adv. Mater.* **2015**, *27*, 6834.
- [134] M. Hunsom, D. Kaewsai, A. M. Kannan, *Int. J. Hydrogen Energy* **2018**, *43*, 21478.
- [135] Y. Sun, Y. Duan, L. Hao, Z. Xing, Y. Dai, R. Li, J. Zou, *ACS Appl. Mater. Interfaces* **2016**, *8*, 25923.
- [136] X. Tian, M. Zhou, C. Tan, M. Li, L. Liang, K. Li, P. Su, *Chem. Eng. J.* **2018**, *348*, 775.
- [137] Y. Zhang, L. Deng, H. Hu, Y. Qiao, H. Yuan, D. Chen, M. Chang, H. Wei, *Sustainable Energy Fuels* **2020**, *4*, 1642.
- [138] S. Dresp, F. Luo, R. Schmack, S. Kühn, M. Gliech, P. Strasser, *Energy Environ. Sci.* **2016**, *9*, 2020.
- [139] R. Cao, J.-S. Lee, M. Liu, J. Cho, *Adv. Energy Mater.* **2012**, *2*, 816.
- [140] L. Sharma, R. Gond, B. Senthilkumar, A. Roy, P. Barpanda, *ACS Catal.* **2020**, *10*, 43.
- [141] D. M. Morales, M. A. Kazakova, M. Purcel, J. Masa, W. Schuhmann, *J. Solid State Electrochem.* **2020**, *24*, 2901.
- [142] Y.-J. Wang, B. Fang, D. Zhang, A. Li, D. P. Wilkinson, A. Ignaszak, L. Zhang, J. Zhang, *Electrochem. Energy Rev.* **2018**, *1*, 1.
- [143] Q. Wang, Y. Lei, Y. Zhu, H. Wang, J. Feng, G. Ma, Y. Wang, Y. Li, B. Nan, Q. Feng, Z. Lu, H. Yu, *ACS Appl. Mater. Interfaces* **2018**, *10*, 29448.
- [144] D. Lyu, S. Yao, Y. Bahari, S. W. Hasan, C. Pan, X. Zhang, F. Yu, Z. Q. Tian, P. K. Shen, *Appl. Mater. Today* **2020**, *20*, 100737.
- [145] J. Kim, J. Park, J. Lee, W.-G. Lim, C. Jo, J. Lee, *Adv. Funct. Mater.* **2021**, *31*, 2010882.
- [146] N. D. K. Tu, S. O. Park, J. Park, Y. Kim, S. K. Kwak, S. J. Kang, *ACS Appl. Energy Mater.* **2020**, *3*, 1602.
- [147] S. T. Senthilkumar, S. O. Park, J. Kim, S. M. Hwang, S. K. Kwak, Y. Kim, *J. Mater. Chem. A* **2017**, *5*, 14174.
- [148] J. Park, J.-S. Park, S. T. Senthilkumar, Y. Kim, *J. Power Sources* **2020**, *450*, 227600.
- [149] W. Lee, J. Park, J. Park, S. J. Kang, Y. Choi, Y. Kim, *J. Mater. Chem. A* **2020**, *8*, 9185.
- [150] Z. Khan, S. O. Park, J. Yang, S. Park, R. Shanker, H.-K. Song, Y. Kim, S. K. Kwak, H. Ko, *J. Mater. Chem. A* **2018**, *6*, 24459.
- [151] S. Kim, S. Ji, H. Yang, H. Son, H. Choi, J. Kang, O. L. Li, *Appl. Catal., B* **2022**, *310*, 121361.
- [152] D. Liu, Y. Tong, X. Yan, J. Liang, S. X. Dou, *Batteries Supercaps* **2019**, *2*, 743.
- [153] J. Fang, X. Zhang, X. Wang, D. Liu, Y. Xue, Z. Xu, Y. Zhang, C. Song, W. Zhu, Z. Zhuang, *J. Mater. Chem. A* **2020**, *8*, 15752.
- [154] G. Fu, Y. Tang, J.-M. Lee, *ChemElectroChem* **2018**, *5*, 1424.
- [155] K. Gao, B. Wang, L. Tao, B. V. Cunnings, Z. Zhang, S. Wang, R. S. Ruoff, L. Qu, *Adv. Mater.* **2019**, *31*, 1805121.
- [156] Z. R. Ismagilov, A. E. Shalagina, O. Yu. Podyacheva, A. V. Ischenko, L. S. Kibis, A. I. Boronin, Y. A. Chesalov, D. I. Kochubey, A. I. Romanenko, O. B. Anikeeva, T. I. Buryakov, E. N. Tkachev, *Carbon* **2009**, *47*, 1922.
- [157] S. C. Ray, W. Mbiombi, P. Papakonstantinou, *Curr. Appl. Phys.* **2014**, *14*, 1845.
- [158] B. Wang, X. Cui, J. Huang, R. Cao, Q. Zhang, *Chin. Chem. Lett.* **2018**, *29*, 1757.
- [159] C. Lai, X. Liu, C. Cao, Y. Wang, Y. Yin, T. Liang, D. D. Dionysiou, *Carbon* **2021**, *173*, 715.
- [160] G. Zhong, S. Li, S. Xu, W. Liao, X. Fu, F. Peng, *ACS Sustainable Chem. Eng.* **2018**, *6*, 15108.
- [161] J. W. F. To, J. W. D. Ng, S. Siahrostami, A. L. Koh, Y. Lee, Z. Chen, K. D. Fong, S. Chen, J. He, W.-G. Bae, J. Wilcox, H. Y. Jeong, K. Kim, F. Studt, J. K. Nørskov, T. F. Jaramillo, Z. Bao, *Nano Res.* **2017**, *10*, 1163.
- [162] D. H. Suh, S. K. Park, P. Nakhanev, Y. Kim, S. M. Hwang, H. S. Park, *J. Power Sources* **2017**, *372*, 31.
- [163] C. Lee, D. Jeon, J. Park, W. Lee, J. Park, S. J. Kang, Y. Kim, J. Ryu, *ACS Appl. Mater. Interfaces* **2020**, *12*, 32689.
- [164] M. U. Zahid, E. Pervaiz, A. Hussain, M. I. Shahzad, M. B. K. Niazi, *Mater. Res. Express* **2018**, *5*, 052002.
- [165] G. Long, K. Wan, M. Liu, X. Li, Z. Liang, J. Piao, *Chin. J. Catal.* **2015**, *36*, 1197.
- [166] R. Li, Z. Wei, X. Gou, *ACS Catal.* **2015**, *5*, 4133.
- [167] J.-C. Li, P.-X. Hou, S.-Y. Zhao, C. Liu, D.-M. Tang, M. Cheng, F. Zhang, H.-M. Cheng, *Energy Environ. Sci.* **2016**, *9*, 3079.
- [168] M. Qiao, S. S. Meysami, G. A. Ferrero, F. Xie, H. Meng, N. Grobert, M.-M. Titirici, *Adv. Funct. Mater.* **2018**, *28*, 1707284.
- [169] L. L. Zhang, X. S. Zhao, *Chem. Soc. Rev.* **2009**, *38*, 2520.
- [170] L.-L. Ma, W.-J. Liu, X. Hu, P. K. S. Lam, J. R. Zeng, H.-Q. Yu, *Chem. Eng. J.* **2020**, *400*, 125969.
- [171] S. A. Nicolae, H. Au, P. Modugno, H. Luo, A. E. Szego, M. Qiao, L. Li, W. Yin, H. J. Heeres, N. Berge, M.-M. Titirici, *Green Chem.* **2020**, *22*, 4747.
- [172] Y. Shen, *Biomass Bioenergy* **2020**, *134*, 105479.
- [173] B. Huang, Y. Liu, Z. Xie, *J. Mater. Chem. A* **2017**, *5*, 23481.
- [174] L. Sun, G. Yuan, L. Gao, J. Yang, M. Chhowalla, M. H. Gharahcheshmeh, K. K. Gleason, Y. S. Choi, B. H. Hong, Z. Liu, *Nat. Rev. Methods Primers* **2021**, *1*, 5.
- [175] A. Behera, P. Mallick, S. S. Mohapatra, in *Corrosion Protection at the Nanoscale* (Eds: S. Rajendran, T. A. Nguyen, S. Kakooei, M. Yeganeh, Y. Li), Elsevier, New York **2020**, p. 227.
- [176] G.-L. Tian, M.-Q. Zhao, D. Yu, X.-Y. Kong, J.-Q. Huang, Q. Zhang, F. Wei, *Small* **2014**, *10*, 2251.
- [177] G.-L. Tian, Q. Zhang, B. Zhang, Y.-G. Jin, J.-Q. Huang, D. S. Su, F. Wei, *Adv. Funct. Mater.* **2014**, *24*, 5956.
- [178] K. Morawa Eblagon, N. Rey-Raap, J. L. Figueiredo, M. F. R. Pereira, *Appl. Surf. Sci.* **2021**, *548*, 149242.

- [179] O. L. Li, K. Prabakar, A. Kaneko, H. Park, T. Ishizaki, *Catal. Today* **2019**, *337*, 102.
- [180] K. Ravichandran, P. K. Praseetha, T. Arun, S. Gobalakrishnan, in *Synthesis of Inorganic Nanomaterials* (Eds: S. Mohan Bhagyaraj, O. S. Oluwafemi, N. Kalarikkal, S. Thomas), Woodhead Publishing, Oxford, UK **2018**, p. 141.
- [181] D. Sumanth Kumar, B. Jai Kumar, H. M. Mahesh, in *Synthesis of Inorganic Nanomaterials* (Eds: S. Mohan Bhagyaraj, O. S. Oluwafemi, N. Kalarikkal, S. Thomas), Woodhead Publishing, Oxford, UK **2018**, p. 59.
- [182] H. Lyu, B. Gao, F. He, C. Ding, J. Tang, J. C. Crittenden, *ACS Sustainable Chem. Eng.* **2017**, *5*, 9568.
- [183] J. C. Park, C. H. Choi, *J. Power Sources* **2017**, *358*, 76.
- [184] C. H. Choi, H.-K. Lim, M. W. Chung, J. C. Park, H. Shin, H. Kim, S. I. Woo, *J. Am. Chem. Soc.* **2014**, *136*, 9070.
- [185] Y. Wang, F. Yu, M. Zhu, C. Ma, D. Zhao, C. Wang, A. Zhou, B. Dai, J. Ji, X. Guo, *J. Mater. Chem. A* **2018**, *6*, 2011.
- [186] A. Khan, M. Goepel, J. C. Colmenares, R. Gläser, *ACS Sustainable Chem. Eng.* **2020**, *8*, 4708.
- [187] A. Ben Belgacem, I. Hinkov, S. B. Yahia, O. Brinza, S. Farhat, *Mater. Today Commun.* **2016**, *8*, 183.
- [188] A. Agrawal, G.-C. Yi, in *Comprehensive Analytical Chemistry* (Ed: C. M. Hussain), Elsevier, New York **2020**, p. 21.
- [189] L. Yang, in *Nanotechnology-Enhanced Orthopedic Materials* (Ed: L. Yang), Woodhead Publishing, Oxford, UK **2015**, p. 97.
- [190] F. V. Ferreira, W. Franceschi, B. R. C. Menezes, A. F. Biagioni, A. R. Coutinho, L. S. Cividanes, in *Carbon-Based Nanofillers and Their Rubber Nanocomposites* (Eds: S. Yaragalla, R. Mishra, S. Thomas, N. Kalarikkal, H. J. Maria), Elsevier, Amsterdam **2019**, p. 31.
- [191] N. Li, Z. Wang, K. Zhao, Z. Shi, Z. Gu, S. Xu, *Carbon* **2010**, *48*, 255.
- [192] S. Gao, H. Liu, K. Geng, X. Wei, *Nano Energy* **2015**, *12*, 785.
- [193] K. Kaare, E. Yu, A. Volperts, G. Dobeles, A. Zhurinsk, A. Dyck, G. Niaura, L. Tamasauskaite-Tamasunaite, E. Norkus, M. Andrulevičius, M. Danilson, I. Kruusenberg, *ACS Omega* **2020**, *5*, 23578.
- [194] P. Chen, L.-K. Wang, G. Wang, M.-R. Gao, J. Ge, W.-J. Yuan, Y.-H. Shen, A.-J. Xie, S.-H. Yu, *Energy Environ. Sci.* **2014**, *7*, 4095.
- [195] S. S. Sekhon, J.-S. Park, *Chem. Eng. J.* **2021**, *425*, 129017.
- [196] Y. Li, G. Wang, T. Wei, Z. Fan, P. Yan, *Nano Energy* **2016**, *19*, 165.
- [197] Z. Guo, Z. Xiao, G. Ren, G. Xiao, Y. Zhu, L. Dai, L. Jiang, *Nano Res.* **2016**, *9*, 1244.
- [198] J. Wang, H. Zhao, Y. Gao, D. Chen, C. Chen, M. Saccoccio, F. Ciucci, *Int. J. Hydrogen Energy* **2016**, *41*, 10744.
- [199] M. Borghei, N. Laocharoen, E. Kibena-Pöldsepp, L.-S. Johansson, J. Campbell, E. Kauppinen, K. Tammeveski, O. J. Rojas, *Appl. Catal., B* **2017**, *204*, 394.
- [200] Z. Ma, K. Wang, Y. Qiu, X. Liu, C. Cao, Y. Feng, P. Hu, *Energy* **2018**, *143*, 43.
- [201] A. Ilnicka, M. Skorupska, M. Tyc, K. Kowalska, P. Kamedulski, W. Zielinski, J. P. Lukaszewicz, *Sci. Rep.* **2021**, *11*, 7084.
- [202] Y. Da, X. Li, C. Zhong, Y. Deng, X. Han, W. Hu, *Adv. Funct. Mater.* **2020**, *30*, 2001704.
- [203] D. Hötger, M. Etkorn, C. Morchutt, B. Wurster, J. Dreiser, S. Stepanow, D. Grumelli, R. Gutzler, K. Kern, *Phys. Chem. Chem. Phys.* **2019**, *21*, 2587.
- [204] M. P. Browne, C. Dominguez, P. E. Colavita, *Curr. Opin. Electrochem.* **2018**, *7*, 208.
- [205] E. Wiercigroch, E. Szafranec, K. Czamara, M. Z. Pacia, K. Majzner, K. Kochan, A. Kaczor, M. Baranska, K. Malek, *Spectrochim. Acta, Part A* **2017**, *185*, 317.
- [206] L. M. Ng, R. Simmons, *Anal. Chem.* **1999**, *71*, 343.
- [207] A. Dutta, in *Spectroscopic Methods for Nanomaterials Characterization*, Elsevier, New York **2017**, p. 73.
- [208] X. Zhao, H. Su, W. Cheng, H. Zhang, W. Che, F. Tang, Q. Liu, *ACS Appl. Mater. Interfaces* **2019**, *11*, 34854.
- [209] A. Misra, P. K. Tyagi, M. K. Singh, D. S. Misra, *Diamond Relat. Mater.* **2006**, *15*, 385.
- [210] G. S. Bang, G. W. Shim, G. H. Shin, D. Y. Jung, H. Park, W. G. Hong, J. Choi, J. Lee, S.-Y. Choi, *ACS Omega* **2018**, *3*, 5522.
- [211] M. Yeganeh Ghotbi, A. Javanmard, H. Soleimani, *Sci. Rep.* **2018**, *8*, 3404.
- [212] Y. Lin, D. Su, *ACS Nano* **2014**, *8*, 7823.
- [213] H. Su, X. Zhao, W. Cheng, H. Zhang, Y. Li, W. Zhou, M. Liu, Q. Liu, *ACS Energy Lett.* **2019**, *4*, 1816.
- [214] Y. Li, W. Cheng, H. Su, X. Zhao, J. He, Q. Liu, *Nano Energy* **2020**, *77*, 105121.
- [215] P. J. Hendra, P. M. Stratton, *Chem. Rev.* **1969**, *69*, 325.
- [216] L. Bokobza, J.-L. Bruneel, M. Couzi, *Vib. Spectrosc.* **2014**, *74*, 57.
- [217] H. W. Kim, M. B. Ross, N. Kornienko, L. Zhang, J. Guo, P. Yang, B. D. McCloskey, *Nat. Catal.* **2018**, *1*, 282.
- [218] M. Acik, G. Lee, C. Mattevi, M. Chhowalla, K. Cho, Y. J. Chabal, *Nat. Mater.* **2010**, *9*, 840.
- [219] K. Vijayarangamuthu, S. Ahn, H. Seo, S.-H. Yoon, C.-M. Park, K.-J. Jeon, *Adv. Mater.* **2016**, *28*, 661.
- [220] N. McEvoy, N. Peltekis, S. Kumar, E. Rezvani, H. Nolan, G. P. Keeley, W. J. Blau, G. S. Duesberg, *Carbon* **2012**, *50*, 1216.
- [221] A. Zahoor, M. Christy, Y. J. Hwang, Y. R. Lim, P. Kim, K. S. Nahm, *Appl. Catal., B* **2014**, *147*, 633.
- [222] M. Yang, Y. Liu, H. Chen, D. Yang, H. Li, *ACS Appl. Mater. Interfaces* **2016**, *8*, 28615.
- [223] Y. Liu, H. Xu, H. Yu, H. Yang, T. Chen, *Sci. Rep.* **2020**, *10*, 20075.
- [224] G. Witjaksono, M. Junaid, M. H. Khir, Z. Ullah, N. Tansu, M. S. Saheed, M. A. Siddiqui, S. S. Ba-Hashwan, A. S. Algamili, S. A. Magsi, M. Z. Aslam, R. Nawaz, *Molecules* **2021**, *26*.
- [225] B. Ruan, J. Wang, D. Shi, Y. Xu, S. Chou, H. Liu, J. Wang, *J. Mater. Chem. A* **2015**, *3*, 19011.
- [226] S. Webster, J. Maultzsch, C. Thomsen, J. Liu, R. Czerw, M. Terrones, F. Adar, C. John, A. Whitley, D. L. Carroll, *MRS Online Proc. Libr.* **2003**, *772*, 78.
- [227] J. A. Behan, Md. K. Hoque, S. N. Stamatina, T. S. Perova, L. Vilella-Arribas, M. García-Melchor, P. E. Colavita, *J. Phys. Chem. C* **2018**, *122*, 20763.
- [228] P. Wang, X. Qi, W. Zhao, M. Qian, H. Bi, F. Huang, *Carbon Energy* **2021**, *3*, 349.
- [229] C. Zhang, L. Fu, N. Liu, M. Liu, Y. Wang, Z. Liu, *Adv. Mater.* **2011**, *23*, 1020.
- [230] X. Cheng, H. Li, Z. Zhao, Y. Wang, X. Wang, *New Carbon Mater.* **2021**, *36*, 93.
- [231] H. Lei, Z. Wang, F. Yang, X. Huang, J. Liu, Y. Liang, J. Xie, M. S. Javed, X. Lu, S. Tan, W. Mai, *Nano Energy* **2020**, *68*, 104293.
- [232] Y. Zhang, W. Ye, J. Fan, V. Cecen, P. Shi, Y. Min, Q. Xu, *ACS Sustainable Chem. Eng.* **2021**, *9*, 11052.
- [233] J. Cao, K. Wang, J. Chen, C. Lei, B. Yang, Z. Li, L. Lei, Y. Hou, K. Ostrikov, *Nano-Micro Lett.* **2019**, *11*, 67.
- [234] Y. Wang, M. Li, Q. Zhou, Q. Wang, X. Zhang, D. Sun, Y. Tang, *Front. Nanotechnol.* **2021**, *3*, 659865.
- [235] X.-W. Song, S. Zhang, H. Zhong, Y. Gao, L. A. Estudillo-Wong, N. Alonso-Vante, X. Shu, Y. Feng, *Inorg. Chem. Front.* **2021**, *8*, 109.
- [236] F. de Groot, *Chem. Rev.* **2001**, *101*, 1779.
- [237] B. Wu, B. Wang, T. Petit, *Energy Storage Mater.* **2021**, *40*, 72.
- [238] S. C. Ray, Z. N. Tetana, R. Erasmus, W.-F. Pong, N. J. Coville, *Appl. Phys. A* **2014**, *115*, 153.
- [239] J. Ren, L. Lin, K. Lieutenant, C. Schulz, D. Wong, T. Gimm, A. Bande, X. Wang, T. Petit, *Small Methods* **2021**, *5*, 2000707.
- [240] H. C. Choi, S. Y. Bae, W.-S. Jang, J. Park, H. J. Song, H.-J. Shin, H. Jung, J.-P. Ahn, *J. Phys. Chem. B* **2005**, *109*, 1683.
- [241] J. Zhong, J. Wang, J.-G. Zhou, B.-H. Mao, C.-H. Liu, H.-B. Liu, Y.-L. Li, T.-K. Sham, X.-H. Sun, S.-D. Wang, *J. Phys. Chem. C* **2013**, *117*, 5931.
- [242] J. Zhou, J. Wang, H. Liu, M. N. Banis, X. Sun, T.-K. Sham, *J. Phys. Chem. Lett.* **2010**, *1*, 1709.

- [243] J. H. Yang, D. H. Lee, M. H. Yum, Y. S. Shin, E. J. Kim, C.-Y. Park, M. H. Kwon, C. W. Yang, J.-B. Yoo, H.-J. Song, H.-J. Shin, Y.-W. Jin, J.-M. Kim, *Carbon* **2006**, *44*, 2219.
- [244] L.-S. Zhang, X.-Q. Liang, W.-G. Song, Z.-Y. Wu, *Phys. Chem. Chem. Phys.* **2010**, *12*, 12055.
- [245] M. Inagaki, M. Toyoda, Y. Soneda, T. Morishita, *Carbon* **2018**, *132*, 104.
- [246] N. Hellgren, J. Guo, C. S  the, A. Agui, J. Nordgren, Y. Luo, H.   gren, J.-E. Sundgren, *Appl. Phys. Lett.* **2001**, *79*, 4348.
- [247] X. Wang, Z. Hou, T. Ikeda, M. Oshima, M. Kakimoto, K. Terakura, *J. Phys. Chem. A* **2013**, *117*, 579.
- [248] P. Lazar, R. Mach, M. Otyepka, *J. Phys. Chem. C* **2019**, *123*, 10695.
- [249] C.-H. Chuang, S. C. Ray, D. Mazumder, S. Sharma, A. Ganguly, P. Papakonstantinou, J.-W. Chiou, H.-M. Tsai, H.-W. Shiu, C.-H. Chen, H.-J. Lin, J. Guo, W.-F. Pong, *Sci. Rep.* **2017**, *7*, 42235.
- [250] U. Tylus, Q. Jia, K. Strickland, N. Ramaswamy, A. Serov, P. Atanassov, S. Mukerjee, *J. Phys. Chem. C* **2014**, *118*, 8999.
- [251] N. H. Turner, J. A. Schreifels, *Anal. Chem.* **2000**, *72*, 99.
- [252] D. Shah, D. I. Patel, T. Roychowdhury, G. B. Rayner, N. O'Toole, D. R. Baer, M. R. Linford, *J. Vac. Sci. Technol. B* **2018**, *36*, 062902.
- [253] A. Yanilmaz, A. Tomak, B. Akbali, C. Bacaksiz, E. Ozceri, O. Ari, R. T. Senger, Y. Selamet, H. M. Zareie, *RSC Adv.* **2017**, *7*, 28383.
- [254] J. S. Roh, H. W. Yoon, L. Zhang, J.-Y. Kim, J. Guo, H. W. Kim, *ACS Appl. Nano Mater.* **2021**, *4*, 7897.
- [255] K. Tian, J. Wang, L. Cao, W. Yang, W. Guo, S. Liu, W. Li, F. Wang, X. Li, Z. Xu, Z. Wang, H. Wang, Y. Hou, *Nat. Commun.* **2020**, *11*, 3884.
- [256] J. Gao, Y. Wang, H. Wu, X. Liu, L. Wang, Q. Yu, A. Li, H. Wang, C. Song, Z. Gao, M. Peng, M. Zhang, N. Ma, J. Wang, W. Zhou, G. Wang, Z. Yin, D. Ma, *Angew. Chem., Int. Ed.* **2019**, *58*, 15089.
- [257] T. Van Khai, H. G. Na, D. S. Kwak, Y. J. Kwon, H. Ham, K. B. Shim, H. W. Kim, *J. Mater. Chem.* **2012**, *22*, 17992.
- [258] D. Wei, Y. Liu, Y. Wang, H. Zhang, L. Huang, G. Yu, *Nano Lett.* **2009**, *9*, 1752.
- [259] Z. Wang, L. Qie, L. Yuan, W. Zhang, X. Hu, Y. Huang, *Carbon* **2013**, *55*, 328.
- [260] G. Panomsuwan, N. Saito, T. Ishizaki, *ACS Appl. Mater. Interfaces* **2016**, *8*, 6962.
- [261] A. Muthukrishnan, Y. Nabae, T. Okajima, T. Ohsaka, *ACS Catal.* **2015**, *5*, 5194.
- [262] X. Zhang, L. Truong-Phuoc, X. Liao, G. Tuci, E. Fonda, V. Papaefthymiou, S. Zafeirotos, G. Giambastiani, S. Pronkin, C. Pham-Huu, *ACS Catal.* **2021**, *11*, 8915.
- [263] O. L. Li, S. Chiba, Y. Wada, G. Panomsuwan, T. Ishizaki, *J. Mater. Chem. A* **2017**, *5*, 2073.
- [264] J. N. Tiwari, A. M. Harzandi, M. Ha, S. Sultan, C. W. Myung, H. J. Park, D. Y. Kim, P. Thangavel, A. N. Singh, P. Sharma, S. S. Chandrasekaran, F. Salehnia, J.-W. Jang, H. S. Shin, Z. Lee, K. S. Kim, *Adv. Energy Mater.* **2019**, *9*, 1900931.
- [265] N. Karikalan, M. Velmurugan, S.-M. Chen, C. Karuppiah, K. M. Al-Anazi, M. A. Ali, B.-S. Lou, *RSC Adv.* **2016**, *6*, 71507.
- [266] F. Davodi, M. Tavakkoli, J. Lahtinen, T. Kallio, *J. Catal.* **2017**, *353*, 19.
- [267] A. W  tscher, T. Eckhard, D. Hiltrop, K. Lotz, W. Schuhmann, C. Andronescu, M. Muhler, *ChemElectroChem* **2019**, *6*, 514.
- [268] Y. Xu, M. J. Dzara, S. Kabir, S. Pylypenko, K. Neyerlin, A. Zakutayev, *Appl. Surf. Sci.* **2020**, *515*, 146012.
- [269] D. Jain, Q. Zhang, J. Hightower, V. Gustin, A. Asthagiri, U. S. Ozkan, *ChemCatChem* **2019**, *11*, 5945.
- [270] J. Zhang, L. Dai, *ACS Catal.* **2015**, *5*, 7244.
- [271] Z.-H. Sheng, L. Shao, J.-J. Chen, W.-J. Bao, F.-B. Wang, X.-H. Xia, *ACS Nano* **2011**, *5*, 4350.
- [272] Z. Wang, R. Jia, J. Zheng, J. Zhao, L. Li, J. Song, Z. Zhu, *ACS Nano* **2011**, *5*, 1677.
- [273] J. Chang, L. Song, C. Liang, Y. Xu, W. Wang, W. Jiang, Y. Ma, Y. Zhang, *Langmuir* **2020**, *36*, 13752.
- [274] L. Gong, J. Sun, X. Li, B. Huang, G. Yang, Y. Liu, *J. Mater. Sci.* **2021**, *56*, 6349.
- [275] A. T. N. Nguyen, J. H. Shim, *RSC Adv.* **2021**, *11*, 12520.
- [276] A. Pendashteh, J. Palma, M. Anderson, J. J. Vilatela, R. Marcilla, *ACS Appl. Energy Mater.* **2018**, *1*, 2434.
- [277] S. Y. Lim, W. Shen, Z. Gao, *Chem. Soc. Rev.* **2015**, *44*, 362.
- [278] B. W. Noffke, Q. Li, K. Raghavachari, L. Li, *J. Am. Chem. Soc.* **2016**, *138*, 13923.
- [279] Q. Guo, J. Feng, D. Chen, N. Song, H. Dong, L. Yu, L. Dong, *J. Phys. Chem. C* **2021**, *125*, 9747.
- [280] H. Huang, C. Liang, H. Sha, Y. Yu, Y. Lou, C. Chen, C. Li, X. Chen, Z. Shi, S. Feng, *Chem. Res. Chin. Univ.* **2019**, *35*, 171.
- [281] Q. Han, N. Chen, J. Zhang, L. Qu, *Mater. Horiz.* **2017**, *4*, 832.
- [282] J. Wang, J. Hao, D. Liu, S. Qin, D. Portehault, Y. Li, Y. Chen, W. Lei, *ACS Energy Lett.* **2017**, *2*, 306.
- [283] W. Niu, Y. Yang, *ACS Energy Lett.* **2018**, *3*, 2796.
- [284] Md. A. Wahab, J. Joseph, L. Atanda, U. K. Sultana, J. N. Beltramini, K. Ostrikov, G. Will, A. P. O'Mullane, A. Abdala, *ACS Appl. Energy Mater.* **2020**, *3*, 1439.
- [285] S. Yang, X. Feng, X. Wang, K. M  llen, *Angew. Chem., Int. Ed.* **2011**, *50*, 5339.
- [286] M. Tahir, N. Mahmood, J. Zhu, A. Mahmood, F. K. Butt, S. Rizwan, I. Aslam, M. Tanveer, F. Idrees, I. Shakir, C. Cao, Y. Hou, *Sci. Rep.* **2015**, *5*, 12389.
- [287] A. L. Ivanovskii, *Prog. Solid State Chem.* **2013**, *41*, 1.
- [288] C. Huang, Y. Li, N. Wang, Y. Xue, Z. Zuo, H. Liu, Y. Li, *Chem. Rev.* **2018**, *118*, 7744.
- [289] X. Qian, Y. Zheng, S. Chen, J. Xu, *Catalysts* **2020**, *10*, 929.
- [290] Y. Zhao, J. Wan, H. Yao, L. Zhang, K. Lin, L. Wang, N. Yang, D. Liu, L. Song, J. Zhu, L. Gu, L. Liu, H. Zhao, Y. Li, D. Wang, *Nat. Chem.* **2018**, *10*, 924.
- [291] Q. Lv, N. Wang, W. Si, Z. Hou, X. Li, X. Wang, F. Zhao, Z. Yang, Y. Zhang, C. Huang, *Appl. Catal., B* **2020**, *261*, 118234.
- [292] J. Gu, S. Magagula, J. Zhao, Z. Chen, *Small Methods* **2019**, *3*, 1800550.
- [293] Z. Shi, W. Yang, Y. Gu, T. Liao, Z. Sun, *Adv. Sci.* **2020**, *7*, 2001069.
- [294] B. Li, Y. Chen, X. Ge, J. Chai, X. Zhang, T. S. A. Hor, G. Du, Z. Liu, H. Zhang, Y. Zong, *Nanoscale* **2016**, *8*, 5067.
- [295] J. Zhang, M. Zhang, L. Qiu, Y. Zeng, J. Chen, C. Zhu, Y. Yu, Z. Zhu, *J. Mater. Chem. A* **2019**, *7*, 19045.
- [296] Z. Liang, N. Kong, C. Yang, W. Zhang, H. Zheng, H. Lin, R. Cao, *Angew. Chem., Int. Ed.* **2021**, *60*, 12759.
- [297] Y. Zhang, P. Wang, J. Yang, S. Lu, K. Li, G. Liu, Y. Duan, J. Qiu, *Carbon* **2021**, *177*, 344.
- [298] Z. Cai, S. Lin, J. Xiao, T. Muhmood, X. Hu, *Adv. Mater. Interfaces* **2021**, *8*, 2001922.
- [299] Q. Lu, H. Wu, X. Zheng, Y. Chen, A. L. Rogach, X. Han, Y. Deng, W. Hu, *Adv. Sci.* **2021**, *8*, 2101438.
- [300] C. Zhu, Q. Shi, B. Z. Xu, S. Fu, G. Wan, C. Yang, S. Yao, J. Song, H. Zhou, D. Du, S. P. Beckman, D. Su, Y. Lin, *Adv. Energy Mater.* **2018**, *8*, 1801956.
- [301] J. Masa, W. Xia, I. Sinev, A. Zhao, Z. Sun, S. Gr  tzke, P. Weide, M. Muhler, W. Schuhmann, *Angew. Chem., Int. Ed.* **2014**, *53*, 8508.
- [302] D. M. Morales, J. Masa, C. Andronescu, Y. U. Kayran, Z. Sun, W. Schuhmann, *Electrochim. Acta* **2016**, *222*, 1191.
- [303] C. Guo, Y. Li, Y. Xu, Q. Xiang, L. Sun, W. Zhang, W. Li, Y. Si, Z. Luo, *Nanoscale Res. Lett.* **2019**, *14*, 22.
- [304] X. Lu, D. Wang, L. Ge, L. Xiao, H. Zhang, L. Liu, J. Zhang, M. An, P. Yang, *New J. Chem.* **2018**, *42*, 19665.
- [305] S. Chen, J. Duan, J. Ran, S.-Z. Qiao, *Adv. Sci.* **2015**, *2*, 1400015.
- [306] M.-S. Balogun, W. Qiu, H. Yang, W. Fan, Y. Huang, P. Fang, G. Li, H. Ji, Y. Tong, *Energy Environ. Sci.* **2016**, *9*, 3411.

- [307] H. Yuan, L. Deng, X. Cai, S. Zhou, Y. Chen, Y. Yuan, *RSC Adv.* **2015**, 5, 56121.
- [308] J. Tian, Q. Liu, A. M. Asiri, K. A. Alamry, X. Sun, *ChemSusChem* **2014**, 7, 2125.
- [309] Y. Zhang, X. Zhang, X. Ma, W. Guo, C. Wang, T. Asefa, X. He, *Sci. Rep.* **2017**, 7, 43366.
- [310] J. Masa, W. Xia, M. Muhler, W. Schuhmann, *Angew. Chem., Int. Ed.* **2015**, 54, 10102.
- [311] Y. Shao, J. Sui, G. Yin, Y. Gao, *Appl. Catal., B* **2008**, 79, 89.
- [312] D. M. Morales, J. Masa, C. Andronesco, W. Schuhmann, *ChemElectroChem* **2017**, 4, 2835.
- [313] Y. Yi, J. Tornow, E. Willinger, M. G. Willinger, C. Ranjan, R. Schlögl, *ChemElectroChem* **2015**, 2, 1929.
- [314] N. Macauley, D. D. Papadias, J. Fairweather, D. Spornjak, D. Langlois, R. Ahluwalia, K. L. More, R. Mukundan, R. L. Borup, *J. Electrochem. Soc.* **2018**, 165, F3148.



Bin Wu is a Ph.D. candidate at the Helmholtz-Zentrum Berlin für Materialien und Energie. He received his B.E. degree in Materials Chemistry from Chongqing University in China in 2016 as well as master degree in Materials Engineering from Institute of Chemistry, Chinese Academy of Sciences in 2019. His current research interests focus on in situ characterization of carbon nano-materials for energy storage and conversion.



Haibing Meng received his Ph.D. in physical chemistry from Institute of Chemistry, Chinese Academy of Sciences, China (2019). From Sep. 2019 to Sep. 2021, he worked as a postdoctoral researcher in the Department of Chemical Engineering at Tsinghua University, China. Currently, he is an associate researcher in the College of Chemistry at Taiyuan University of Technology, China. His research interests focus on the design and fabrication of nanomaterials for gas adsorption and separation, electrocatalysis, and photocatalysis.



Dulce M. Morales is currently deputy head of the Young Investigator Group NOME led by Dr. Marcel Risch at Helmholtz-Zentrum Berlin für Materialien und Energie. She has a background in Industrial Chemical Engineering from Instituto Politécnico Nacional in Mexico City, and earned her Ph.D. degree in Chemistry in 2019 mentored by Prof. Wolfgang Schuhmann at Ruhr-Universität Bochum. Her research focuses on the development of non-noble multimetallic composites as electrocatalysts for sustainable energy conversion and storage applications, and presently aims for their study under industrial-relevant conditions.



Tristan Petit leads the Young Investigator Group Nanoscale Solid-Liquid Interfaces at Helmholtz-Zentrum Berlin für Materialien und Energie. He obtained master degrees from ISAE-Supaéro, France and ETH Zürich, Switzerland in 2010 and a Ph.D. in Physics from ENS Cachan, France in 2013. He received a Freigeist Fellowship from the Volkswagen Foundation in 2015 and an ERC Starting Grant in 2020. His research focuses on in situ/operando spectroscopy of carbon nano-materials and MXenes for energy conversion and storage applications.